University of Southampton

Microstructuring and domain-engineering in Lithium Niobate using combinations of light, etching and poling

Alexander John Boyland

Degree of Doctor of Philosophy

Optoelectronics Research Centre
Faculty of Science

July 2003

UNIVERSITY OF SOUTHAMPTON

ABSTRACT

FACULTY OF ENGINEERING AND APPLIED SCIENCE
DEPARTMENT OF ELECTRONICS AND COMPUTER SCIENCE
OPTOELECTRONICS RESEARCH CENTRE

Microstructuring and domain engineering in Lithium Niobate using combinations of light, etching and poling

By Alexander John Boyland

The work presented in this thesis reports methods for microstructuring of lithium niobate. The process of light induced frustrating etching, where light from a laser is used to inhibit the etching of iron doped lithium niobate, is the subject of a detailed investigation so a better understanding of the process can be developed. The process was found to be dependent upon illumination and etch times, iron dopant levels, and irradiance levels. Analysis of the structures formed revealed that they were resistant to the etchant used and were positively charged. Two dimensional Fourier transform analysis of images obtained were used to confirm that the structures preferentially propagated along 3 directions each 120° apart.

A novel electro-optically controlled domain-engineered total internal reflection switch and beam deflector is also reported. Device construction uses electric field poling of lithium niobate to create two parallel but oppositely oriented domains. When an electric field is applied across the interface between these domains a change in the refractive index of equal magnitude but of opposite sign is induced. If light incident on this interface sees a sufficient difference in refractive index it can be total internally reflected. The total internal reflection switch shows high contrast ratio switching of greater than 20dB and is less wavelength dependent than other electro-optic switches, such as the Pockels cell. The beam deflector can produce large angular deflections, which are increased by faceting of the output face. Deflections of greater than 18° have been demonstrated using this technique. Cascading of devices and possible device implementations are also suggested.

Contents

"Esse Quam Videri"

Colyton Grammar School Motto

Acknowledgements

I would like to thank Professor Rob Eason for his enthusiasm, support and guidance throughout my time at the ORC. I would also like to thank the EPSRC and the ORC for funding and making this research project possible.

Thanks also to colleagues Sakellaris Mailis, Jason Hendricks, Jeffery Scott, and Stephen Barrington for their assistance and discussions.

Thanks also to my family for their encouragement throughout the duration of my studies.

Lastly, but by no means least thanks to Doreen-Asiya Sekibo for her unwavering support, encouragement and understanding throughout the years I have known her.

All the work in this thesis has been conducted by myself while a postgraduate student in the research group of Professor R.W. Eason at the Optoelectronics Research Centre, University of Southampton.

The modelling on page 55 was developed in collaboration with Jeffery Scott (another member of the research group), and that on page 76 was developed in collaboration with Dr J.M. Hendricks (also a member of the research group).

Chapter 1

Introduction

1.1 Introduction

Since the first reports of successful single domain growth of lithium niobate (LN) in 1965 [Ballman65] it has found increasing use in many areas including optoelectronics, Q-switching, holographic data storage and modulator use. However with domain engineering or structuring at the micron / submicron scale for either bulk or surface modification even greater functionality can be introduced thereby further extending the possible applications. The combination of piezoelectric, nonlinear and electro-optic as well as linear optical properties makes LN a material of great interest and potential.

A great deal of the technology used for micromachining of LN has been borrowed from the well established microelectronics industry. However some techniques have been specifically developed for domain engineering and microstructuring of LN, and a schematic illustrating some of those routes is shown in fig. 1.1.

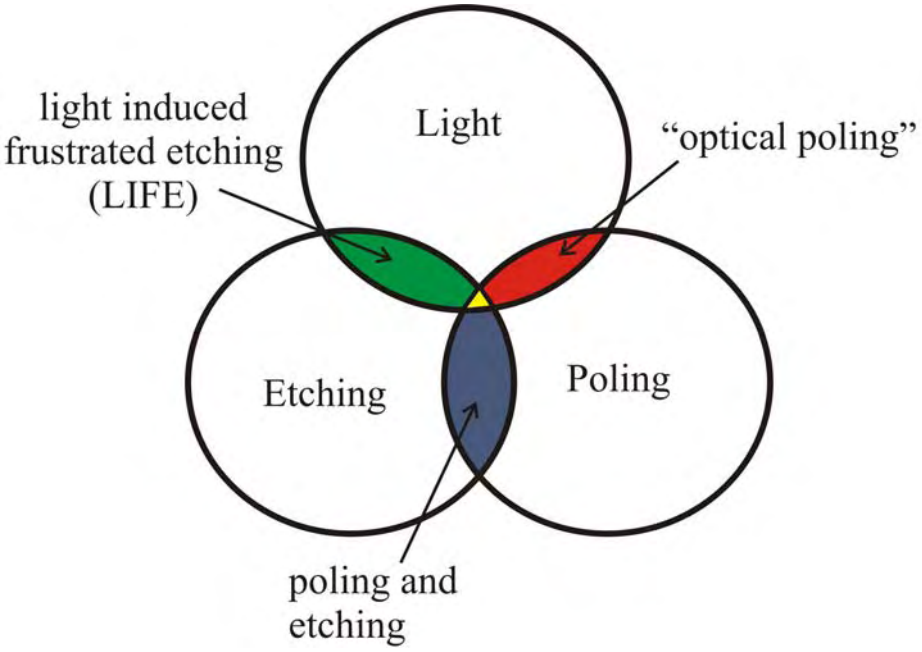

Fig. 1.1. Schematic illustrating possible routes to domain engineering and microstructuring

Domain inversion by electric field poling followed by etching is one of the key routes to microstructuring and with the use of suitable etchants high sensitivity to domain orientation can be observed. This technique has been demonstrated by Barry et al [Barry98] and has been used extensively since to fabricate and characterise structures of ~μm scale dimensions. However the use of “optical poling”, where light has been used to define the pattern for domain inversion using an electric field [Brown99], and light induced frustrated etching (LIFE) which has combined the use of light and etching to achieve patterning of Fe doped LN [Barry99], also show promising routes to microstructuring. The need for structuring methodologies for, and accurate control of, the patterning, processing and subsequent revealing stages leading to smaller features sizes is of great interest.

1.2 Outline

The history of LN and its properties relevant to this thesis are discussed in chapter 2, which includes growth mechanisms, crystal structure and optical, ferroelectric and linear electro-optic properties. Chapter 3 introduces the theory behind electric field poling for both the creation of single domain crystals and selective domain inversion. The etching of LN and suggested mechanisms for differential etching are also discussed. A summary of reported microstructuring techniques for LN is also included.

Chapters 4 – 6 comprise the experimental work carried out. In chapter 4 an in-depth study of the LIFE process of Fe doped LN is reported. The study was carried out in order to build a detailed picture of the theory behind the process so that attempts can be made to control it and therefore produce useful 2D and 3D structures. The parameters investigated experimentally include illumination and etching times, Fe dopant levels, and irradiance levels. The structures produced have been analysed with a variety of metrological techniques including optical and scanning electron microscopes (SEM) and the images from these have subsequently been analysed using two dimensional Fourier transforms. The structures have also been analysed using a localized charge force microscopy to investigate the surface charge associated with the structures. Chapters 5 and 6 report a device demonstrating novel techniques for electro-optically controlled total internal reflection (TIR) switching and deflection of beams of light incident on a domain engineered interface respectively. The TIR switch reported in chapter 5 offers the potential of very high contrast ratio switching as TIR is a 100% efficient process. The light beam deflector reported in chapter 6 has been used to demonstrate large angular deflections of the order ~18^{o}.

Chapter 7 discusses areas of future work and potential applications for the techniques and devices reported in ch's 4 - 6. A summary of the conclusions drawn from this work is reported in chapter 8.

1.3 References

[Ballman65] Ballman, A. A. (1965) *J. Am. Ceram. Soc*, **48,** 112.

[Barry98] Barry, I. E., Ross, G. W., Smith, P. G. R., Eason, R. W. and Cook, G. (1998) *Materials Letters*, **37,** 246-254.

[Barry99] Barry, I. E., Eason, R.W., Cook, G. (1999) *Applied Surface Science*, **143,** 328.

[Brown99] Brown, P. T., Ross, G. W., Eason, R. W. and Pogosyan, A. R. (1999) *Optics Communications*, **163,** 310-316.

Chapter 2

Lithium niobate

2.1 Overview

Lithium niobate is an artificial material which was first synthesized in 1949 [Matthias49] and has been found to have an attractive combination of piezoelectric, nonlinear and electro-optic as well as linear optical properties. These properties have meant that it has remained an extensively studied material since its first reported successful single crystal growth by the Czochralski technique (described in 2.2) in 1965 [Ballman65]. The initial results characterising the materials aspects of LN were published in a set of five sequential papers from the Bell Laboratories [Nassau66a, Nassau66b, Abrahams 66a, Abrahams 66b, Abrahams 66c]. Today there is still an enormous amount of interest in the material and its applications which is shown by the fact that between 1989 and today over 6500 research papers have been published and worldwide over 80 tons of lithium niobate is grown per year and fabricated into wafers [Wong]. In this chapter only the properties relevant to this project will be discussed.

2.2 Growth mechanisms

There are a number of techniques used to grow LN but the most widely used for industrial growth is known as the Czochralski method, so we limit our discussion to this method only in this section.

The Czochralski growth method starts with the pure compound (e.g. powder or crystal fragments) of the material to be grown being melted in a crucible. A seed crystal suspended from a rotating seed rod is then lowered into the furnace cavity, and the tip is touched into the melt. If the melt temperature is just above the melting point of the material (1250^{o}C for LN), growth of a crystal can be initiated by slowly withdrawing the seed rod. As the growth progresses, the diameter of the growing crystal is controlled by adjusting the crucible temperature and the pulling rate. Lowering the temperature will accelerate the crystallisation and lead to a diameter increase, while increasing the temperature will reduce the crystal diameter. The components of a Czochralski system are: the crucible containing the melt, the heat generation with surrounding insulation, seed pull and rotation mechanism, and a feedback system for diameter control [Jundt]. An example of a Czochralski system can be seen in fig. 2.1.

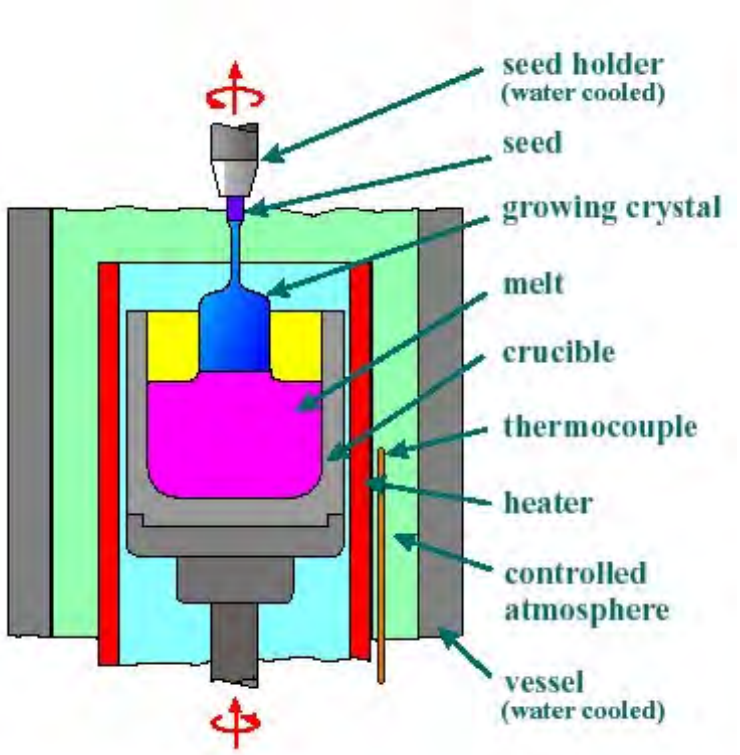

Fig. 2.1. Schematic of a Czochralski crystal growth system [Max-Planck-Institute]

2.3 Crystal properties

2.3.1 Crystal structure

LN is a member of the perovskite type family of structures. Below the Curie temperature it is ferroelectric and has a structure consisting of planar sheets of oxygen atoms in a distorted hexagonal close-packed configuration. The octahedral interstices formed in this structure are one-third filled by lithium atoms, one-third filled by niobium atoms, and one-third vacant. Above the Curie temperature LN is paraelectric and the Li atoms lie in an oxygen layer and the Nb atoms are centred between oxygen layers. The relative positions of the lithium and niobium atoms with respect to the oxygen octahedra in the ferroelectric and paraelectric phases can be seen in fig. 2.2 and fig. 2.3. In fig. 2.3 the positions of the atoms can be seen for both ferroelectric domain orientations.

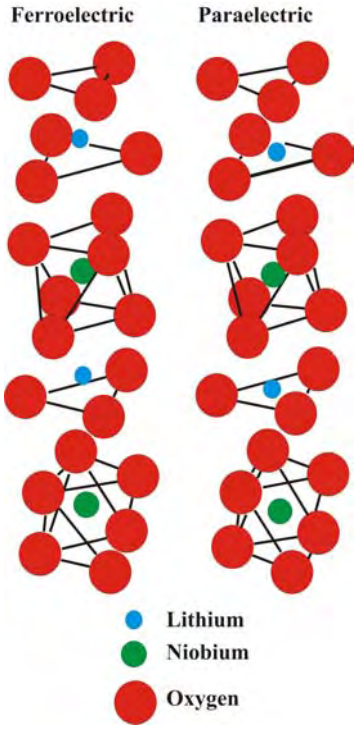

Fig. 2.2. Positions of the lithium atoms and niobium atoms with respect to the oxygen octahedra in the ferroelectric and paraelectric phases of lithium niobate.

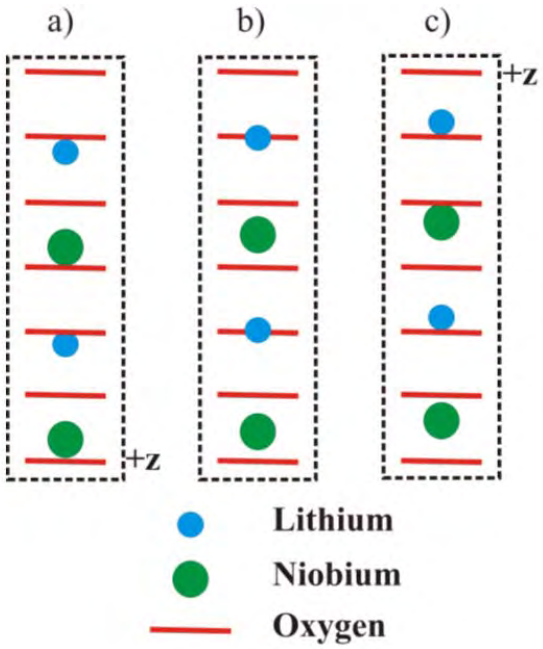

Fig. 2.3. Positions of the lithium and niobium atoms in paraelectric phase (b) and the two domain directions for the ferroelectric phase (a+c).

Due to the high Curie temperature of LN the remainder of this chapter will only refer to the ferroelectric phase.

In the ferroelectric phase LN is a trigonal crystal as it exhibits three-fold rotation symmetry about its *c*-axis. It also has mirror symmetry about three planes that are 60^{o} apart and intersect forming a three-fold rotation axis, which is shown in fig. 2.4. These two symmetry operations mean that LN is classified as a member of the 3m point group [Weis85].

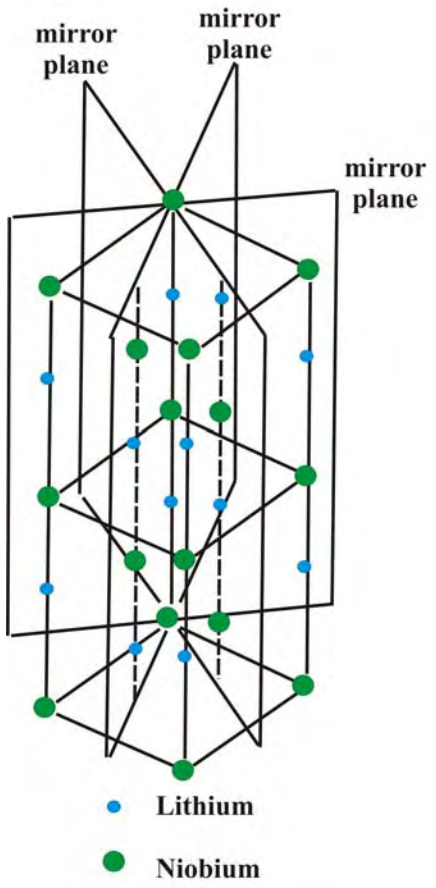

Fig. 2.4. Planes of mirror symmetry associated with lithium niobate.

Trigonal crystals such as LN can be represented by a hexagonal unit cell, as shown in fig. 2.5. The *c*-axis is labelled, with the +*c* orientation being assigned to the face that becomes positive as the crystal cools after growth. The three equivalent *a*-axis (a_1, a_2, a_3) lie in the plane normal to the *c*-axis and are 120^o apart.

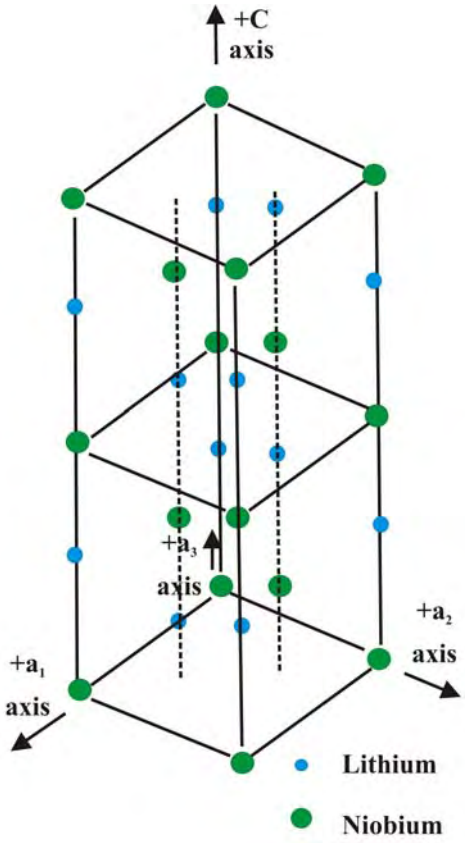

Fig.2.5. Hexagonal unit cell of lithium niobate showing hexagonal axis (c, a_1, a_2, a_3).

The physical tensor properties are described by a Cartesian *x*, *y*, *z* coordinate system. The convention that relates these coordinates to the hexagonal axes described previously is that the *z*-axis is chosen to be parallel to the *c*-axis. The *x*-axis is chosen to coincide with any of the equivalent *a*-axes. The y-axis is then chosen so that a right-handed system is specified; therefore it must lie in a plane of mirror symmetry. When working with tensors the x, y, and z axes are often referred to as the x_1, x_2, and x_3 axes, respectively. The Cartesian coordinates can be seen in fig. 2.6.

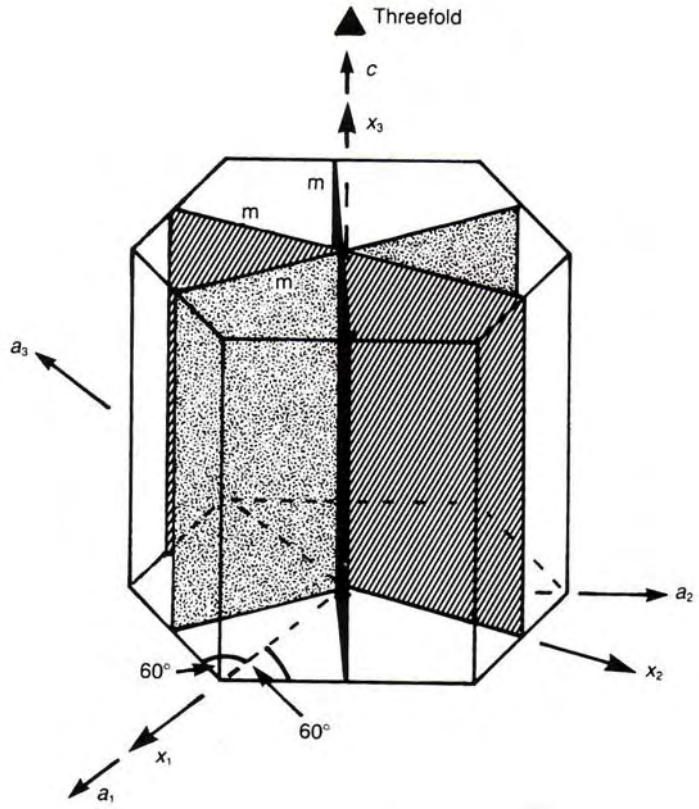

Fig.2.6. Schematic of the 3m hexagonal unit cell showing Cartesian coordinates [Lovett]

2.3.2 Ferroelectric properties

Following crystal growth, the crystal is left to cool. As the temperature decreases from the Curie temperature, the elastic forces of the crystal become dominant and force the lithium and niobium atoms into new positions. The charge separation resulting from this shift of ions relative to the oxygen octahedra causes LN to exhibit spontaneous polarisation [Weis85]. Because of this spontaneous polarisation there will be a permanent electrostatic charge on the surfaces of the crystal, with one face positive and another negative. These charges are not normally observed because the atmosphere usually contains sufficient free positive and negative ions to neutralise the free surface charge by being attracted to, and adsorbed on, the surface. As LN possesses this spontaneous polarisation, it is classified as a ferroelectric crystal. A

crystal is said to be ferroelectric when it has two or more orientational states of polarisation, in the absence of an applied electric field [Anderson].

If a crystal is allowed to cool below T_c in the absence of an applied field there are at least two directions along which the spontaneous polarisation can develop. To minimise the depolarising fields, different regions of the crystal polarise in one of these two equivalent directions and each macroscopic volume of uniform polarisation is known as a domain. The result is a domain structure which reduces the net macroscopic polarisation nearly to zero. To obtain single domain crystals a process called poling is used which will be discussed in more detail in 3.2. Poling of a crystal is done by applying an electric field (E) greater than the coercive field across it; this has the effect of forcing the polarisation into the direction of the applied field throughout the crystal and therefore forcing the crystal into a single domain structure. The coercive field (E_c) is the applied electric field required that would result in reducing the spontaneous polarisation (P_s) to zero. Typical values of P_s and E_c for LN at room temperature are of the order ~0.72μCmm^{-2} [Kim02] and ~21kVmm^{-1} [Kim02] respectively.

2.3.3 Optical properties

LN is a negative uniaxial crystal, which means that its optical properties are defined by two refractive indices, the extraordinary refractive index (n_e) and the ordinary refractive index (n_o), where n_e is less than n_o. LN is transparent from ~ 0.35μm to > 5μm [Rauber]. The absorption spectrum of undoped LN can be seen in fig. 2.7.

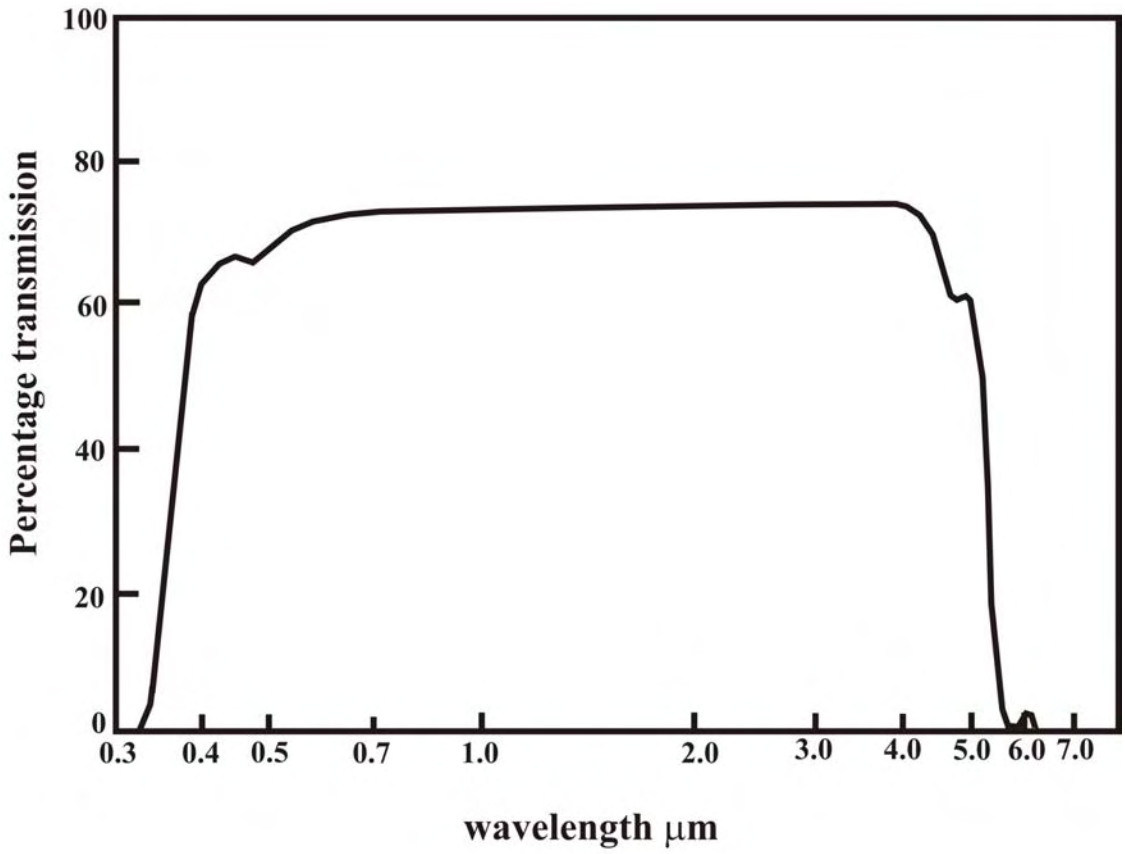

Fig. 2.7. Transmission spectrum of undoped lithium niobate before Fresnel losses are accounted for [Nassau66b]

The refractive indices of congruent LN have been measured at 24.5°C over the wavelength range 0.40μm – 3.05 μm [Nelson74] and have been confirmed by others [Smith76]. The data of [Nelson74] and the temperature dependent measurements at two wavelengths (0.633 μm and 3.39 μm) reported in [Smith76], were fitted to temperature dependent Sellmeier equations. Converting to the format of [Hobden66], the generic equation becomes:

$$n^2(\lambda,T) = a_1 + \frac{a_2 + b_1 f(T)}{\lambda^2 - \left(a_3 + b_2 f(T)\right)^2} + b_3 f(T) + a_4 \lambda^2 \qquad \textbf{(2.1)}$$

where λ is the free-space wavelength (nm) and $f(T)=(T-T_0)(T+T_0+546)$ with T_0=24.5°C, the temperature of the original measurements [Nelson74]. The other coefficients in eqn. 2.1 are given in table 2.1 [Kirkby].

	n_o	n_e
a_1	4.9048	4.5820
a_2	1.1775×10^{5}	0.9921×10^{5}
a_3	2.1805×10^{2}	2.1090×10^{2}
a_4	-2.7153×10^{-8}	-2.1940×10^{-8}
b_1	2.2314×10^{-2}	5.2716×10^{-2}
b_2	-2.9671×10^{-5}	-4.9143×10^{-5}
b_3	2.1429×10^{-8}	2.2971×10^{-8}

Table 2.1. Coefficients for Sellmeier equation 2.1

2.3.4 Linear Electro-optic properties

The linear electro-optic effect is defined as a change in n_e and n_o that is linearly proportional to an applied electric field. This effect only exists in crystals that do not possess inversion symmetry.

Mathematically, the linear electro-optic effect is represented as a deformation of the index ellipsoid. For a uniaxial crystal such as LN, where $n_x = n_y = n_o$ and $n_z = n_e$, the index ellipsoid in the absence of an applied electric field is represented by [Yariv]:

$$\frac{x^2}{n_x^2}+\frac{y^2}{n_y^2}+\frac{z^2}{n_z^2}=1 \qquad \textbf{(2.2)}$$

where x, y, and z are the principal axes.

The effect of an electric field on the propagation of light can be expressed as changes in the constants $\frac{1}{n_x^2}$, $\frac{1}{n_y^2}$ and $\frac{1}{n_z^2}$ of the index ellipsoid. The index ellipsoid in the presence of an electric field then becomes:

$$\left(\frac{1}{n^2}\right)_1 x^2 + \left(\frac{1}{n^2}\right)_2 y^2 + \left(\frac{1}{n^2}\right)_3 z^2 + 2\left(\frac{1}{n^2}\right)_4 yz + 2\left(\frac{1}{n^2}\right)_5 xz + 2\left(\frac{1}{n^2}\right)_6 xy = 1 \quad \textbf{(2.3)}$$

The linear change in the coefficients

$$\left(\frac{1}{n^2}\right)_i \qquad i = 1, ..., 6$$

due to an arbitrary dc electric field E (E_x) is defined by

$$\Delta\left(\frac{1}{n^2}\right)_i = \sum_{j=1}^{3} r_{ij} E_j \qquad \textbf{(2.4)}$$

where in the summation over j the convention 1 = x, 2 = y, and 3 = z is used. Expression (2.4) can be expressed in matrix form as:

$$\begin{vmatrix} \Delta\left(\frac{1}{n^2}\right)_1 \\ \Delta\left(\frac{1}{n^2}\right)_2 \\ \Delta\left(\frac{1}{n^2}\right)_3 \\ \Delta\left(\frac{1}{n^2}\right)_4 \\ \Delta\left(\frac{1}{n^2}\right)_5 \\ \Delta\left(\frac{1}{n^2}\right)_6 \end{vmatrix} = \begin{vmatrix} r_{11} & r_{12} & r_{13} \\ r_{21} & r_{22} & r_{23} \\ r_{31} & r_{32} & r_{33} \\ r_{41} & r_{42} & r_{43} \\ r_{51} & r_{52} & r_{53} \\ r_{61} & r_{62} & r_{63} \end{vmatrix} \begin{vmatrix} E_1 \\ E_2 \\ E_3 \end{vmatrix} \qquad \textbf{(2.5)}$$

Due to the symmetry operations of the 3m point group the electro-optic coefficients for LN reduce to the form [Lovett]:

$$\begin{pmatrix} 0 & -r_{22} & r_{13} \\ 0 & r_{22} & r_{13} \\ 0 & 0 & r_{33} \\ 0 & r_{51} & 0 \\ r_{51} & 0 & 0 \\ -r_{22} & 0 & 0 \end{pmatrix}$$

where $r_{42}=r_{51}$, $r_{22}=-r_{12}=-r_{61}$, *and* $r_{13}=r_{23}$. Therefore the electro-optic effect in LN can be described by four independent coefficients.

Typical literature values for these coefficients measured using light of 633nm are [Yariv]:

Electro-optic coefficients $(10^{-12}\ mV^{-1})$	
r_{13}	9.6
r_{22}	6.8
r_{33}	30.8
r_{51}	32.6

Table 2.2. Typical values of the electro-optic coefficients for LN [Yariv]

2.3.5 Photorefractive properties

The photorefractive effect, also commonly know as optical damage because of its detrimental effect on the quality of an optical beam passing through the crystal, refers

to an optically induced change in the refractive indices . This effect was first reported by Ashkin [Ashkin66] and then by Chen [Chen67]. Chen suggested that the change in the refractive index of the crystal was caused by photoexcited carriers being transported along the polar axes of the crystal and subsequently being trapped [Chen69]. Chen assumed the carriers to originate from impurities or defects in the LN crystal.

Because LN has a high electrical resistance at room temperature, even a small current flowing in the crystal can cause a high space field charge which will modify the refractive indices of the crystal via the electro-optic effect. This change in refractive index (Δn) is reversible. The magnitude of Δn which can vary from 10^{-6} to 10^{-3} depends on the laser radiation intensity (10^{-1} – 10^{3} Wcm^{-2}) and its dose (1-10^{3} Jcm^{-2}). The time relaxation of Δn is dependent on the temperature of the crystal and the impurity concentration and can range from 10^{-4} s to several years [Wong].

There is general agreement that the photoexcited carriers come from Fe^{2+} impurities in LN crystals and the photorefractive sensitivity is proportional to its Fe^{2+} concentration [Wong]. The Fe^{2+} ion is photoionized via the reaction:

$$Fe^{2+} + h\upsilon \rightarrow Fe^{3+} + e^{-} \qquad \textbf{(2.6)}$$

When the electron is first excited its charge is compensated by the ion, but as the charge carrier moves away from the ion an electric field builds up. Although electrons are mentioned here as the method of charge transfer holes may also be responsible, in this situation Fe^{3+} ions act as donors and Fe^{2+} as acceptors. The charge migration can be produced by diffusion, drift, bulk photovoltaic effect, or a combination of these

effects. In LN the dominant charge migration mechanism is the bulk photovoltaic effect [Weis85].

2.4 References

[Abrahams 66a] Abrahams, S. C., Reddy, J.M., and Bernstein, J.L. (1966) *J. Phys. Chem. Solids,* **27,** 997-112.

[Abrahams 66b] Abrahams, S. C., Reddy, J.M., and Bernstein, J.L. (1966) *J. Phys. Chem. Solids,* **27,** 1013-1018.

[Abrahams 66c] Abrahams, S. C., Reddy, J.M., and Bernstein, J.L. (1966) *J. Phys.Chem. Solids,* **27,** 1019-1026.

[Anderson] Anderson, J. C., Leaver, K.D., Rawlings, R.D., and Alexander, J.M. (1991) *Materials Science,* Chapman and Hall, London.

[Ashkin66] Ashkin, A., Boyd, G.D., Dziedzic, J.M., Smith, R.G., Ballman, A.A., Levinstien, H.J., Nassau, K. (1966) *Applied Physics Letters,* **9,** 72.

[Ballman65] Ballman, A. A. (1965) *J. Am. Ceram. Soc*, **48,** 112.

[Chen67] Chen, F. S. (1967) *J. Appl. Phys.*, **38,** 3418.

[Chen69] Chen, F. S. (1969) *J. Appl. Phys.*, **40,** 3389-96.

[Hobden66] Hobden, M. V., and Warner, J. (1966) *Phys. Lett. (Netherlands),* **22,** 243.

[Jundt] Jundt, D. H., and Foulon, G. (2002) In *Properties of Lithium Niobate*(Ed, Wong, K. K.) INSPEC, London, pp. 25-27.

[Kim02] Kim, S., Gopalan, V. and Gruverman, A. (2002) *Applied Physics Letters,* **80,** 2740-2742.

[Kirkby] Kirkby, C. J. G., updated by Florea, C. (2002) In *Properties of Lithium Niobate*(Ed, Wong, K. K.) INSPEC, London, pp. 119-128.

[Lovett] Lovett, D. R. (1999) *Tensor Properties of Crystals*, Institute of Physics Publishing, Bristol, UK.

[Matthias49] Matthias, B. T., and Remaika, J.P. (1949) *Phys. Rev.*, **76,** 1886-1887.

[Max-Planck-Institute] http://www.mpi-stuttgart.mpg.de/crystal/czochralski.pdf

[Nassau66a] Nassau, K., Levinstein, H.J., and Loiacono, G.M. (1966) *J. Phys. Chem. Solids*, **27,** 983-988.

[Nassau66b] Nassau, K., Levinstein, H.J., and Loiacono, G.M. (1966) *J. Phys. Chem. Solids*, **27,** 989-996.

[Nelson74] Nelson, D. F. a. M., R.M. (1974) *J. Appl. Phys.*, **45,** 3688.

[Rauber] Rauber, A. (1978) In *Current topics in Materials Science*(Ed, Kaldis, E.) North-Holland, Amsterdam, pp. 481-601.

[Smith76] Smith, S. D., Riccius, H.D., and Edwin, R.P. (1976) *Optics Communications*, **17,** 332.

[Weis85] Weis, R. S. and Gaylord, T. K. (1985) *Applied Physics a-Materials Science & Processing*, **37,** 191-203.

[Wong] Wong, K. K. (2002) In *Properties of Lithium Niobate*(Ed, Wong, K. K.) INSPEC, London.

[Yariv] Yariv, A. (1997) *Optical Electronics in Modern Communications*, Oxford University Press, Oxford.

Chapter 3

Domain-engineering of lithium niobate

3.1 Overview

There has been a great interest in the structuring and domain-engineering of LN ever since the first reports of single crystal growth in 1965 [Ballman65]. LN has found applications in many areas including optoelectronics, laser systems and Q-switching. However further domain-engineering, micron / nano-scale bulk or surface modifications could increase the range of applications to include such possibilities as routes to MEMS and MOEMS devices, electro-optic switches, nonlinear optical and piezoelectric devices etc.

In this chapter electric field poling and chemical etching will be described in detail as these processes form the basis of the experimental work reported in later chapters. Overviews of some of the alternative structuring and domain-engineering procedures will also be reported.

3.2 Electric field poling

3.2.1 Creation of single-domain crystals

In order to be able to make any controlled domain structures in LN it is important to start with a single domain crystal. Crystals grown by the Czochralski method are usually many-domain. There are a few ways of changing them into single domain crystals [Nassau66a], the most commonly used methods are:

i. growing crystals in an electric field

ii. application of an electric field to a crystal at temperatures close to the Curie temperature

The first method has shown successful single domain formation (almost 100%) but often leads to large defect regions (cavities) within the crystal. As a result of this the most widely used method for creation of a single domain crystal is method ii). Although crystals can be poled anywhere below the Curie temperature the electric field required becomes very large as the temperature drops significantly below the transition temperature [Myers95]. Because of this a multi-domain crystal is harvested from the growth furnace after having been cooled to room temperature, and is then heated to a temperature above the Curie temperature [Nassau66a]. While at room temperature a crystal that has been grown along the *z*-axis direction would have electrodes placed at the top and bottom so that the field can be applied along the *z* axis direction. To ensure adequate and uniform contact, the areas where the voltage is applied are often covered with a platinum paste (suspension of platinum particles in a solvent). After the paste has dried, the electrodes are connected, and the crystal is heated to above the Curie temperature. A small electric field, 0.2 – 5 Vcm^{-1} [Nassau66a], is then applied, as the crystal is cooled below the Curie temperature. Once the crystal has cooled a few degrees below the transition temperature, the field can be switched off without any danger of depolarisation. The time required for the voltage to be applied is mainly determined by the crystal temperature uncertainty and the cooling rate.

3.2.2 Selective domain inversion

The use of an external electric field for the domain inversion of ferroelectric LN to produce periodically poled (PPLN) structures at room temperature is a well reported technique [Yamada93, Burns94, Webjorn94, Myers95]. Selective domain inversion is not limited to periodically poled structures and can be used to create other feature shapes including cylindrical lenses [Yamada96] and 2D hexLN [Broderick00].

The preparation procedure for poling of optical-grade LN wafers is as follows:

- cut wafer to the desired shape and size for the chosen application
- thorough cleaning using a multi-step procedure (see appendix 1)
- photoresist is spun onto the –*z* face of the sample
- this resist is patterned using photolithography
- a 4mm wide strip of insulating tape is then placed around the area to be poled to prevent electrical breakdown
- liquid electrodes are then evenly applied within the taped area as well as the corresponding region on the +*z* face

The sample is then placed in the poling rig as illustrated in fig.3.1. For domain inversion to occur an electric field greater than (E_c) must be applied across the sample. To ensure that this field is applied the charge corresponding to the area to be domain inverted is calculated. This charge, Q, is calculated using the expression:

$$Q = 2 \times P_s \times A \qquad \textbf{(3.1a)}$$

where P_s is the spontaneous polarisation and A is the area.

However, an additional empirical factor (EF) is usually required to correct for variations in supplier-dependent material stoichiometry, precise values of thickness

across the sample, and electrical characteristics of the poling supply itself. Therefore expression (3.1a) is modified to become:

$$Q = 2 \times P_s \times A \times EF \qquad \textbf{(3.1b)}$$

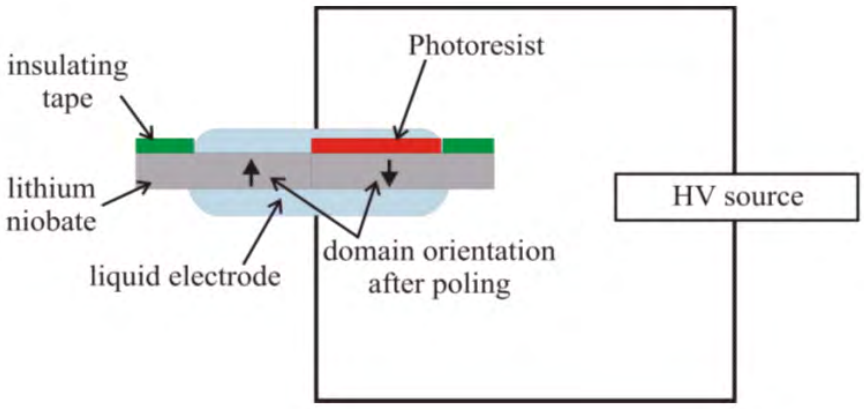

Fig.3.1. Schematic of electric field poling apparatus

When poling is carried out the current is monitored to ensure the correct amount of charge flows through the sample. When the current corresponding to the value of charge as calculated by expression 3.1b has passed through the circuit the apparatus automatically switches off.

The quality of the poling result i.e. how precisely the domains follow the desired pattern is dependent on many factors, which include:

- crystal flatness (parallelism)
- quality of surface polishing – no scratches
- sample cleanliness
- patterning – quality of photolithography
- good contact – use of liquid electrodes

To obtain high quality poling of straight line domains better results are achieved when patterning is aligned parallel to the y-axis.

Optical microscopy cannot be used to observe the domain structure of LN, because the index ellipsoids in 180^{o} domains have the same orientation. However, the use of cross-polarizers may be used to reveal domain walls in LN, which are rendered visible because of the presence of stress birefringence that arises near the domain walls. An investigation into the presence of birefringence at a single domain boundary is discussed in section 5.5.

3.3 Etching

Etching has been reported as a way of differentiating between domain orientations from as early as 1966 [Nassau66b]. Various reagents have been have been reported including a potassium hydroxide (KOH) melt at 400^{o}C, and a mixture of two parts of 30% hydrogen peroxide and one part of sodium hydroxide at 50^{o}C. The use of a mixture of two parts of nitric acid (HNO_3) and one part hydrofluoric acid (HF) was also reported [Nassau66b] and showed better results and became the chief method of revealing domains in LN crystals [Prokhorov]. Etching is able to reveal the domain structure of LN because the two domain orientations have very different etching characteristics: although the etch rate of the –z face varies with temperature and etchant ratio, the +z face does not etch at all. Although the 2:1 etchant ratio of HNO_3:HF was widely accepted it is was not until 2002 that Sones *et al* [Sones02a] reported a parametric study of etch rates and etch quality as a function of the specific ratio of HF:HNO_3. This report also included a possible explanation for the mechanism behind the differential etching.

To investigate the dependence of etch rate on etchant ratios a single sample of LN was poled to create two oppositely oriented domain regions, this sample was then cut into four identical samples consisting of the two domain regions. This procedure was necessary to ensure as much uniformity as possible in both the source material, and the processing associated with poling. Each sample was then immersed in etchants consisting of different HNO_3:HF ratios at 60°C for 15 hours.

The results shown in fig.3.2 clearly show that the etch rate increases almost linearly with the amount of HF added to nitric acid.

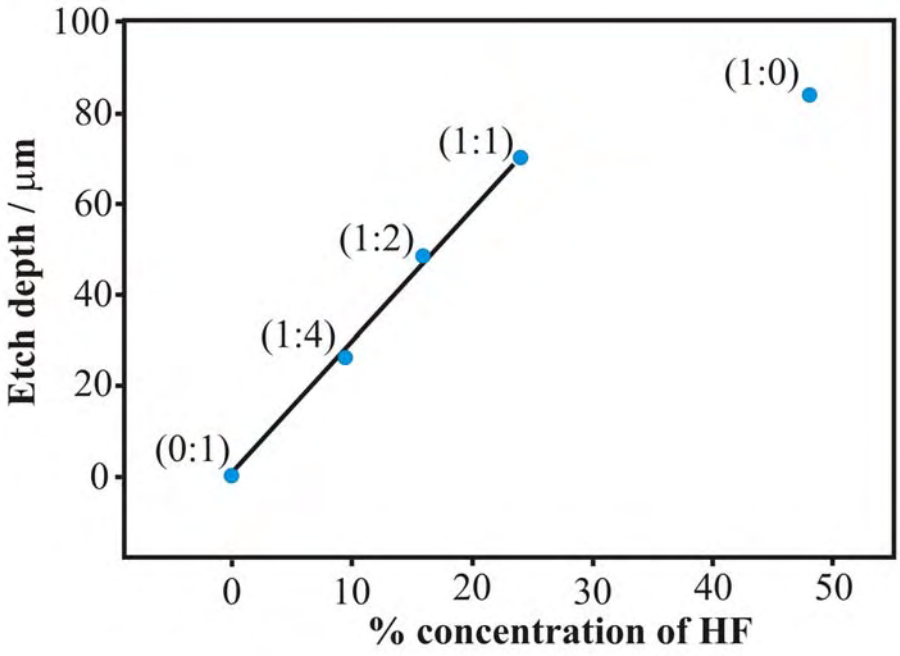

Figure 3.2. Etch depth as a factor of HF/HNO_3 ratio used in etchant. The depth corresponds to etching for 15 hours at a temperature of 60°C. The numbers in brackets correspond to the ratio used [Sones02a].

Sones *et al* suggest that the etching mechanism is initiated by surface protonation, which would explain some of the qualitative observations made:

a) differential etching – the negative face is etched faster due to easier absorption of the positively charged proton.

b) faster etching – the etch rate increases with increasing concentration of acidic protons.

In the model suggested for etching with HF/HNO_3 solutions it assumes that HNO_3 is probably strong enough to saturate the negatively charged surface with protons, dehydroxylate completely and then cover the M_s^+ surface with nitrate:

$$MOH_s + H^+ \rightarrow M_s^+ \rightarrow MNO_3 \qquad \textbf{(3.2)}$$

The subsequent reaction is determined by the rate of fluoride substitution at the surface.

$$MNO_3 + H_2F_2 \rightarrow MF + HNO_3 + HF \qquad \textbf{(3.3)}$$

As well as being a method of distinguishing between domain orientations, in combination with selective domain poling, etching can be used as a method for making microstructured devices. Devices reported to date include alignment grooves for efficient fibre-pigtailing to LN modulators [Barry98] and piezoelectrically controlled micro-cantilevers [Sones02b].

3.4 Structuring techniques

3.4.1 Ion beam milling

Ion beam (IB) milling (also known as ion beam etching) is an inert-gas ion etching mechanism where material is removed by a momentum exchange between a highly

collimated beam of ions colliding with the atoms in the material being sputtered [Puckett].The ions are produced from an inert gas such as argon and are then accelerated in an electric field and directed towards the target. A schematic diagram of the apparatus for IB can be seen in fig.3.3. IB milling of LN [Smith74] is a difficult process that has very low etch rates and produces by-products that are not easily removable during the milling process leading to undesirable redeposition. The main aspects of IB can be summarised as:

- slow etch rates
- substrate faceting
- redeposition of sputtered material
- poor selectivity of LN to mask materials

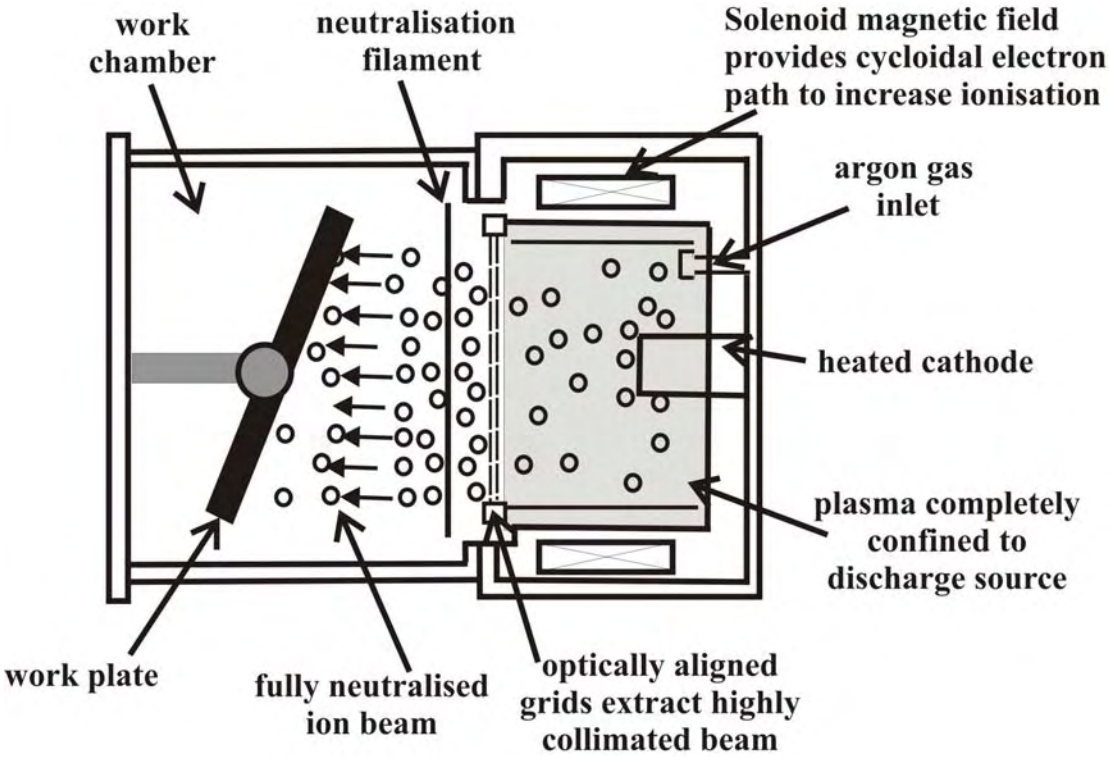

Fig. 3.3. Schematic of ion beam milling apparatus [after ionbeammilling]

3.4.2 Plasma and reactive ion etching

Plasma etching requires an RF excited cathode around which the plasma is formed. The sample to be etched is placed on a grounded substrate table in close proximity to the plasma region; ions emerging from the plasma strike the sample usually at modest energy (10-300 eV) and at incident angles from almost 0^o to 90^o. The etching action is almost entirely chemical, the formation of volatile products between the sample and the active ion, as apposed to momentum transfer, being the main mechanism of removal [Pitt]. The earliest forms of this mechanism used inert gas ions, but the process is used more frequently with reactive gases and is then referred to as reactive ion etching (RIE). Fig.3.4. shows a schematic diagram of apparatus used for RIE.

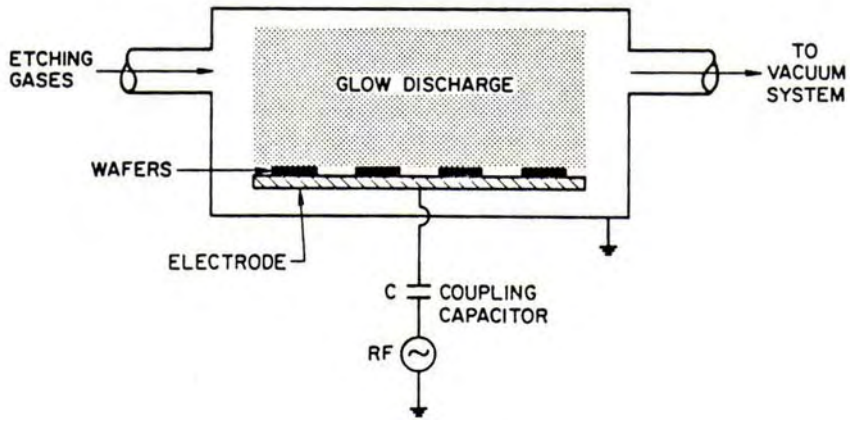

Fig. 3.4. Schematic diagram of apparatus used for RIE [Oehrlein]

Plasma etching [Lee79] and reactive ion etching (RIE) [Jackel81] of LN has shown:

- higher selectivity than IB milling
- undercutting

3.4.3 Reactive ion beam etching

Reactive ion beam etching (RIBE) refers to the mechanism similar to that described in 3.4.1 but where a chemical reaction between the target material and the gas from which the ions are made enhances the sputtering with a reactive etching contribution.

RIBE of LN [Matsui80, Ren87] can provide better results than inert-gas milling since additional material removal is obtained through the chemical reaction involving the reactive gas.

3.4.4 Electron beam direct writing

Electron beam direct writing methods use modified scanning electron microscopes (SEM) to produce a beam of electrons that are highly focusable and controllable by electric and magnetic fields. An SEM consists of an electron beam that is focused and steered by magnetic fields produced by current-carrying coils.

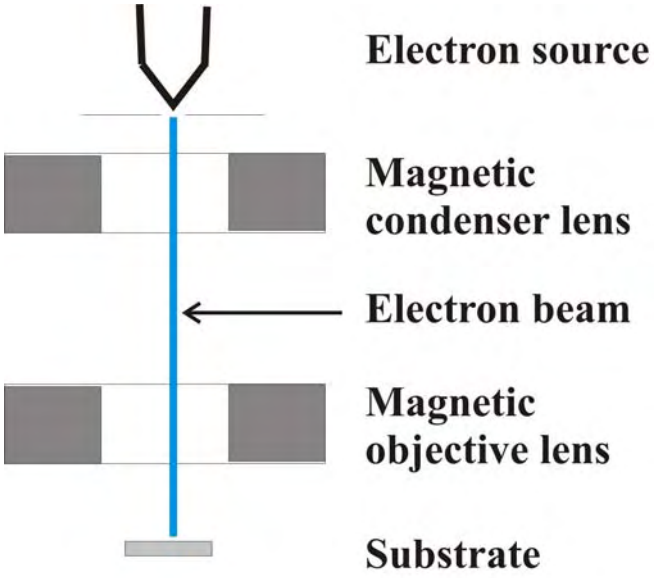

Fig. 3.5. Schematic of SEM used for electron beam direct writing

Ferroelectric domain inversion of LN with an electron beam (EB) has been reported where early methods were carried out at high temperatures with the application of an electric field [Haycock86, Keys90]. These methods were superseded by the use of direct write EB scanning at room temperature with no applied field [Itoh91, Yamada91, Nutt92, Fujimura92, Fujimura93] to form domain inverted gratings. The mechanism for this method of domain inversion was suggested by Restoin *et al*

[Restoin00]. Restoin *et al* suggest that the process can be represented as local electric field poling because LN is an insulator; the charges of the electrons generate an electric field across the crystal and LN spontaneous polarization reversal follows from displacement of the ions in the structure.

The main aspects of direct write e-beam poling can be summarised as:

- does not require lithography
- claims 5nm resolution [Restion00]

3.4.5 Laser-enhanced chemical etching

Laser-enhanced chemical etching either in molten salts [Ashby86] or in a gas atmosphere [Beeson88] is another process for removing material. In the salt-fusion process [Ashby86] which is carried out in air, powdered potassium fluoride (KF) was sprinkled on the surface. Since KF is extremely deliquescent, water is rapidly absorbed from the air. Pulses from an Nd-YAG-pumped frequency-doubled dye laser at 270nm wavelength are then used to heat the surface to create a fusion reaction between the KF and the molten LN. The resulting solid is highly water soluble. The insolubility of LN permits subsequent removal of the irradiated area by rinsing in water. The material removal rate is reported to be 10μm min^{-1}.

Beeson *et al* [Beeson88] report another combined chemical/ablation process where LN is exposed to pulses from a frequency doubled argon-ion laser at 257nm wavelength in an atmosphere of chlorine (Cl_2). A 0.8μm deep hole was achieved from a 10 second exposure.

The aspects of laser assisted chemical etching can be summarised as:

- maskless micromaching

- poor surface roughness when compared to gas-etched LN

3.4.6 Ablation

Laser ablation refers to the use of high laser power densities, i.e. greater than 10^6 Wcm^{-2}, to etch a solid rapidly without the deliberate introduction of a chemically reactive species [Ashby]. Ablation of LN has been reported by Eyett *et al* [Eyett87]. A XeCl excimer laser of 308nm wavelength was used, and the results indicated a threshold for ablation at ~1 Jcm^{-2}. The ablation rate per pulse varied from ~0.02 μm per pulse (1 Jcm^{-2}) to 0.14 μm per pulse (3 Jcm^{-2}).

3.4.7 Optically assisted electric field poling

This process involves a technique where light is used to assist in the process of domain inversion. In this technique the is electric field is applied via electrodes, while the light is used to define the pattern for the regions to be domain inverted. This technique has been demonstrated by Ross *et al* [Ross97], where UV light from an argon-ion laser was used. A schematic of the experimental apparatus can be seen in fig.3.6.

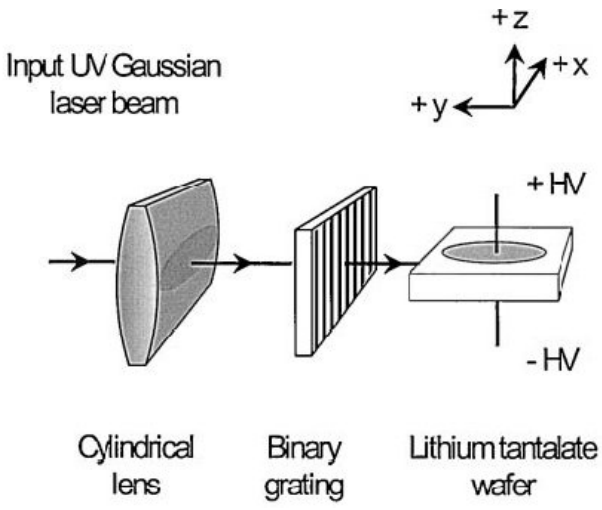

Fig.3.6. Schematic of experimental setup [Ross97]

This method has subsequently demonstrated that the domain structure can be periodically inverted using optical interference patterning techniques [Brown99].

3.4.8 Direct bonding

Domain boundaries equivalent to those created by poling could also be created by bonding two suitably oriented single domain crystals together. This could be done by bonding two z-cut crystals side-by-side or face-to-face as illustrated in fig.3.7.

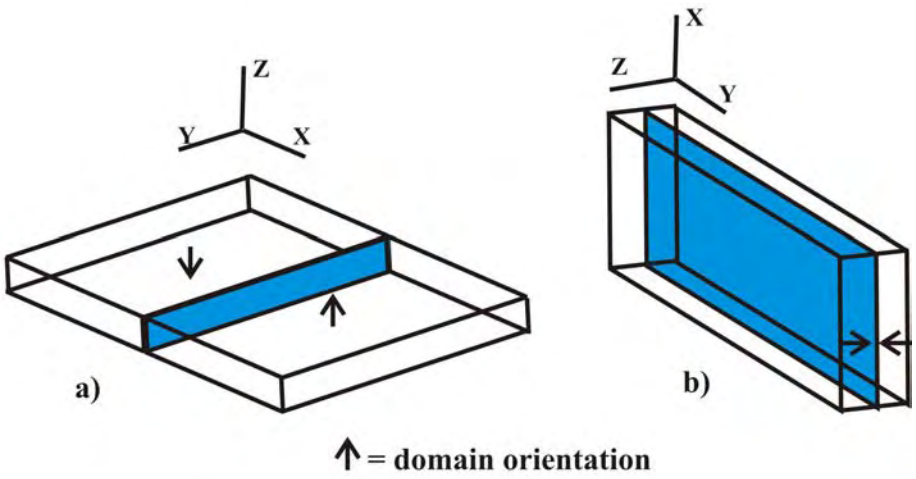

Fig.3.7. Possible bonding configurations to form a boundary between oppositely oriented domains

Bonding of LN has been demonstrated by Gawith *et al* [Gawith99]. To ensure good bonding, the samples need to be thoroughly cleaned (appendix1), then treated to render the surfaces hydrophilic. The mixture used for this was H_2O_2-NH_4OH-H_2O (1-1-6), followed by rinsing thoroughly in de-ionised water. The samples are then brought into contact at room temperature. Immediately after contact they were heated to 120^{o}C. The resultant electrostatic attraction forces any excess liquid or air from between the surfaces, while bringing them close enough to enable the formation of hydrogen bonds. The final step in the process is to anneal the samples at 320^{o}C to make the bonds strong enough for further machining [Gawith99].

3.5 Summary

In this chapter the techniques of electric field poling and etching have been described and possible explanations of the mechanisms behind these processes suggested. Other techniques for structuring or domain-engineering of LN have also been discussed. It is clear to see that there are numerous methods for structuring or domain-engineering of LN which confirms the large interest in this area.

3.6 References

[Ashby] Ashby, C. I. H. (1991) In *Thin film processes II*(Ed, Vossen, J. L., and Kern, W.) Academic Press Inc, London.

[Ashby86] Ashby, C. I. H., and Brannon, P.J., (1986) *Applied Physics Letters,* **49,** 475-477.

[Ballman65] Ballman, A. A. (1965) *J. Am. Ceram. Soc*, **48,** 112.

[Barry98] Barry, I. E., Ross, G. W., Smith, P. G. R., Eason, R. W. and Cook, G. (1998) *Materials Letters,* **37,** 246-254.

[Beeson88] Beeson, K. W., Houlding, V.H., Beach, R., and Osgood, R.M. Jr (1988) *J. Appl. Phys.,* **64,** 835-840.

[Broderick00] Broderick, N. G. R., Ross, G.W., Offerhaus, H.L., Richardson, D.J., and Hanna, D.C. (2000) *Phys. Rev. Letts.,* **84,** 4345-4348.

[Brown99] Brown, P. T., Ross, G. W., Eason, R. W. and Pogosyan, A. R. (1999) *Optics Communications,* **163,** 310-316.

[Eyett87] Eyett, M., and Bauerle, D. (1987) *Applied Physics Letters,* **51,** 2054-5055.

[Fujimura92] Fujimura, M., Suhara, T., and Nishihara, H. (1992) *Electronics Letters,* **28,** 721-722.

[Fujimura93] Fujimura, M., Suhara, T., and Nishihara, H. (1993) *Journal of Lightwave Technology,* **11,** 1360-1367.

[Gawith99] Gawith, C. B. E., Shepherd, D.P., Abernethy, J.A., Hanna, D.C., Ross, G.W., and Smith, P.G.R. (1999) *Optics Letters,* **24,** 481.

[Haycock86] Haycock, P., and Townsend, P.D. (1986) *Applied Physics Letters,* **48,** 698-700.

[ionbeammilling] www.ionbeammilling.com

[Ito91] Ito, H., Takyu, C., and Inaba, H. (1991) *Electronics Letters,* **27,** 1221-1222.

[Jackel81] Jackel, J. L., Howard, E.L., Hu, E.L., and Lyman, S.P. (1981) *Applied Physics Letters,* **38,** 907.

[Keys90] Keys, R. W., Loni, A., De La Rue, R.M., Ironside, C.N., Marsh, J.H., Luff, B.J., and Townsend, P.D. (1990) *Electronics Letters,* **26,** 188-190.

[Lee79] Lee, C. L., and Lu, C.L. (1979) *Applied Physics Letters,* **35,** 756.

[Matsui80] Matsui, S., Yamato, T., Aritome, H., and Namaba, S. (1980) *Jpn. Appl. Phys.,* **19,** 463.

[Nassau66a] Nassau, K., Levinstein, H.J., and Loiacono, G.M. (1966) *J. Phys. Chem. Solids,* **27,** 989-996.

[Nassau66b] Nassau, K., Levinstein, H.J., and Loiacono, G.M. (1966) *J. Phys. Chem. Solids,* **27,** 983-988.

[Nutt92] Nutt, A. C. G., Gopalan, V., and Gupta, M.C. (1992) *Applied Physics Letters,* **60,** 2828-2830.

[Oehrlein] Oehrlein, G. S. (1990) In *Handbook of plasma processing technology*(Ed, Rossnagel, S. M., Cuomo, J.J., and Westwood, W.D.,) Noyes Publications, Park Ridge, USA.

[Pitt] Pitt, C. W. (2001) In *Properties of Lithium Niobate*(Ed, Wong, K. K.) IEE, London.

[Prokhorov] Prokhorov, A. M., and Kus'minov, Y.S., (1990) *Physics and Chemistry of Crystalline Lithium Niobate,* Adams Hilger, Bristol.

[Puckett] Puckett, P. R., Michel, S.L., and Hughes, W.E. (1991) In *Thin Film Process II*(Ed, Vossen, J. L., and Kern, W.) Academic Press, Inc, London.

[Restoin00] Restoin, C., Darraud-Taupiac, C., Decossas. J.L., Vareille, J.C., Hauden, J., and Martinaz, A. (2000) *J. Appl. Phys.*, **88,** 6665-6668.

[Ross97] Ross, G. W., Smith, P.G.R., and Eason, R.W. (1997) *Applied Physics Letters,* **71,** 309-311.

[Smith74] Smith, H. I. (1974) *IEEE Proceedings,* **62,** 1361.

[Sones02a] Sones, C. L., Mailis, S., Brocklesby, W. S., Eason, R. W. and Owen, J. R. (2002) *Journal of Materials Chemistry,* **12,** 295-298.

[Sones02b] Sones, C. L., Mailis, S., Apostolopoulos, V., Barry, I.E., Gawith, C.B.E., Smith, P.G.R., and Eason, R.W. (2002) *Journal of Micromechanics and Microengineering,* **12,** 53-57.

[Yamada91] Yamada, M., and Kishima, K. (1991) *Electronics Letters,* **27,** 828-829.

[Yamada96] Yamada, M., Saitoh, M. and Ooki, H. (1996) *Applied Physics Letters,* **69,** 3659-3661.

Chapter 4

Light Induced Frustrated Etching

4.1 Overview

Structuring of photonic and optoelectronic materials at sub-micron scale lengths is of considerable interest in areas such as photonic crystal structures [Joannopoulos], Bragg grating fabrication [Kashyap], tips for scanning probe microscopes, and the developing area of MOEMS [Walker]. In all cases, such structuring requires methodologies for, and accurate control of, the patterning, processing and subsequent revealing stages for the features to be fabricated. In this chapter new results in the microstructuring of iron doped lithium niobate single crystals for which the normal etch characteristics are modified through a photochemical process at the LN/etchant interface will be reported. This work is a continuation of initial results reported by Barry [Barry99], however it differs in that this previous work was mainly directed at total suppression of etching and used crystals with higher dopant concentration (0.2% Fe). This chapter reports an investigation of the partial suppression of etching. Initial results were reported in [Boyland00] with a more detailed analysis reported in [Scott03]. Partial frustration of etching refers to a regime where despite uniform illumination of a region on a sample in the presence of etchant a process occurs that results in the formation of sub-micron filamentary structures that are resistant to the etchant, while the area between these structures etches as though light was not present. This is in contrast to total suppression of etching where the entire illuminated region is prevented from etching.

4.2 Theory

As previously mentioned in chapter 2, one of the characteristic features of LN is its strong photovoltaic effect [Glass74], the strength of which is associated with the concentration of Fe doping – the major impurity found in LN. Fe plays a major role in both the photovoltaic effect, which is linearly dependent on Fe^{2+} concentration, and the photoconductivity which is determined by electron transfer from Fe^{2+} to Fe^{3+} centres [Sommerfeldt88]. This transfer of charges is particularly pronounced in the visible absorption bands of Fe^{2+} at ~2.6eV (476nm) and Fe^{3+} at ~2.55eV (488nm) and 2.95eV (420nm). The doping concentration therefore clearly leads to increased numbers of mobile charges being available. The absorption spectra for undoped LN and LN doped with a range of Fe dopant concentrations were measured using a spectrophotometer as shown in fig. 4.1.

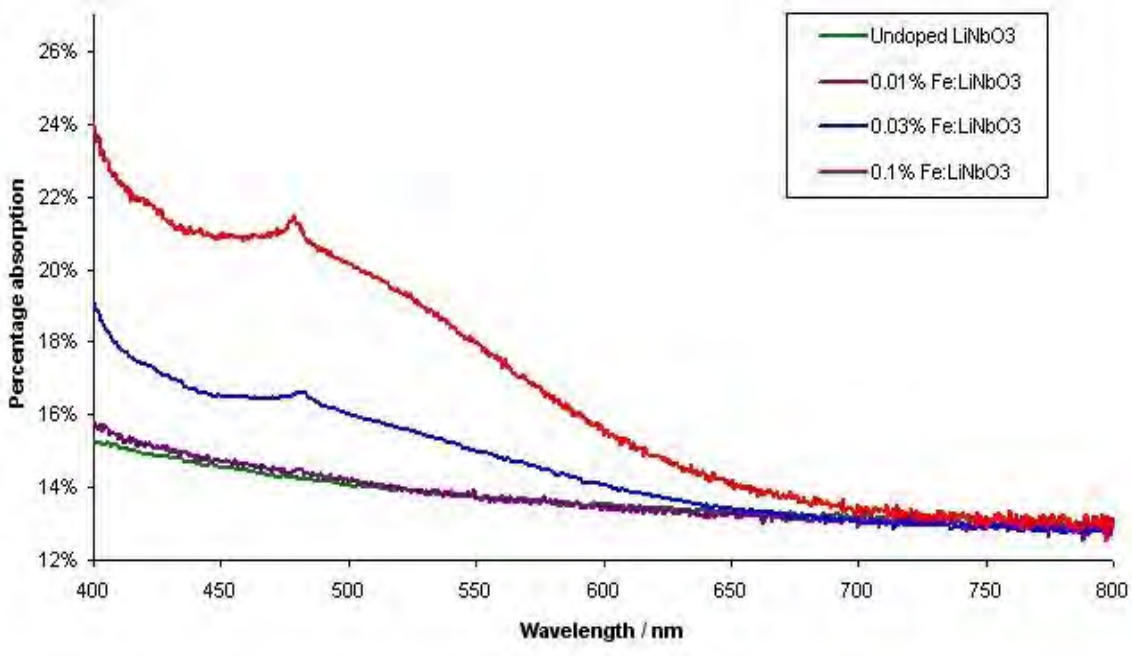

Figure 4.1. Measured absorption data for undoped and Fe: doped LN before Fresenel losses are accounted for

When setting up the experiment to ensure that the sample is exposed to a value of irradiance that is within the region necessary for partial suppression of etching, expressions 4.1 and 4.2 are used. The initial spot size ω_1 after focussing is found using [Svelto]:

$$\omega_1 = \frac{\lambda f}{\pi \omega_0} \tag{4.1}$$

where ω_0 is the spot size of the output beam from the laser, λ is the wavelength of the laser light, and f is the focal length of the lens.

Using this and the experimentally measured total power in the beam (P) the peak intensity (I_0), and the intensity ($I(r)$) at distance (r) from the peak, can be calculated using the following expression [Siegman]:

$$I(r) = I_0 e^{\frac{-2r^2}{\omega_1^2}} = \frac{2P}{\pi \omega_1^2} e^{\frac{-2r^2}{\omega_1^2}} \tag{4.2}$$

Barry [Barry99] observed the sub-micron filamentary structures associated partial frustration of etching for 0.2% Fe doped LN at intensities of the order of ~3.7 Wcm^{-2} using light of 488nm wavelength.

4.3 Experimental procedure

To allow illumination of the –z face of the crystal from below while it is being etched from above required the use of an etch resistant cell. The etch cell seen in fig. 4.2 is constructed from a stainless steel ring with a PTFE sleeve through the centre. The

PTFE is used because of its good resistance to the 1:2 mixture of HF:HNO_3 being used as an etchant.

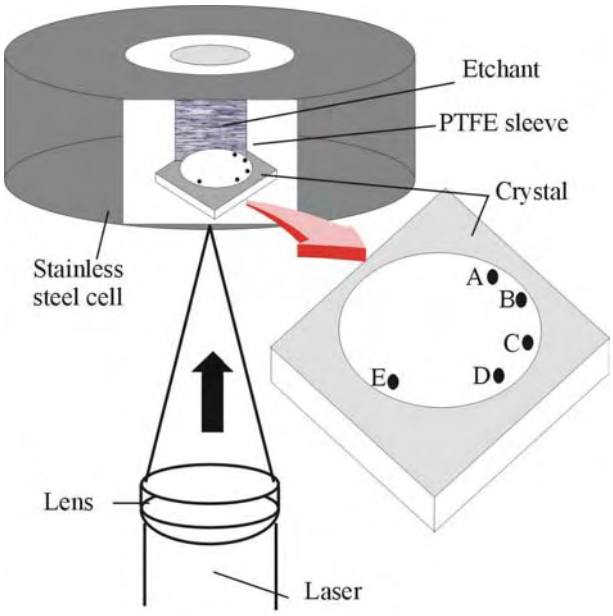

Fig. 4.2. Schematic arrangement of cell used to conduct LIFE experiments with Fe:doped lithum niobate.

4.3.1 Initial experiment (488nm)

The initial experiment was carried out using the setup as in fig 4.2. The crystal used was 0.05% Fe: doped LN and an argon ion laser at 488nm was focused through the crystal onto the upper face (-z) and a site on the sample was illuminated in the presence of the etchant. After 1 hour the laser was turned off, the cell was disassembled and the crystal was examined using optical and scanning electron microscopes. This experiment was used to determine the power levels required to observe partial frustration of etching in LN crystals doped with this level of Fe. Barry [Barry99] observed the sub-micron filamentary structures associated partial frustration for intensities of the order of ~3.7Wcm^{-2} for 0.2% Fe doped LN, because of the lower dopant levels used in this experiment and the reduced absorptivity

associated with this it is expected that partial frustration will also be observed for higher intensity levels.

4.3.2 Latent LIFE (488nm)

In order to investigate the dynamics behind the structuring of these samples, an experiment was designed to investigate whether any latency effects were present in the LIFE process. A latency effect is defined as an effect that still occurs after the stimulus that caused the initial effect has been removed. The latency characteristics examined by this experiment will determine whether sites that have been prevented from etching due to illumination are still etch resistant after the light has been removed. Five sites (labelled A-E) of a 0.05% Fe doped LN crystal were exposed to laser illumination from an argon ion laser at 488nm, at the same power density, each for one hour in duration. The total etch run lasted 5 hours, and was conducted at room temperature without the cell being adjusted or disturbed, other than to turn it around to expose a new site to laser illumination. Site A was the first site and therefore had 1 hour of illuminated etching, followed by 4 hours of unilluminated etching, whereas site E had the complementary procedure of 4 hours unilluminated etching, followed by an hour of illuminated etching. This procedure is illustrated schematically in fig. 4.3. After 5 hours, the cell was disassembled, and the sample was examined. By illuminating the sites in this sequence the duration of the latency effect can be investigated.

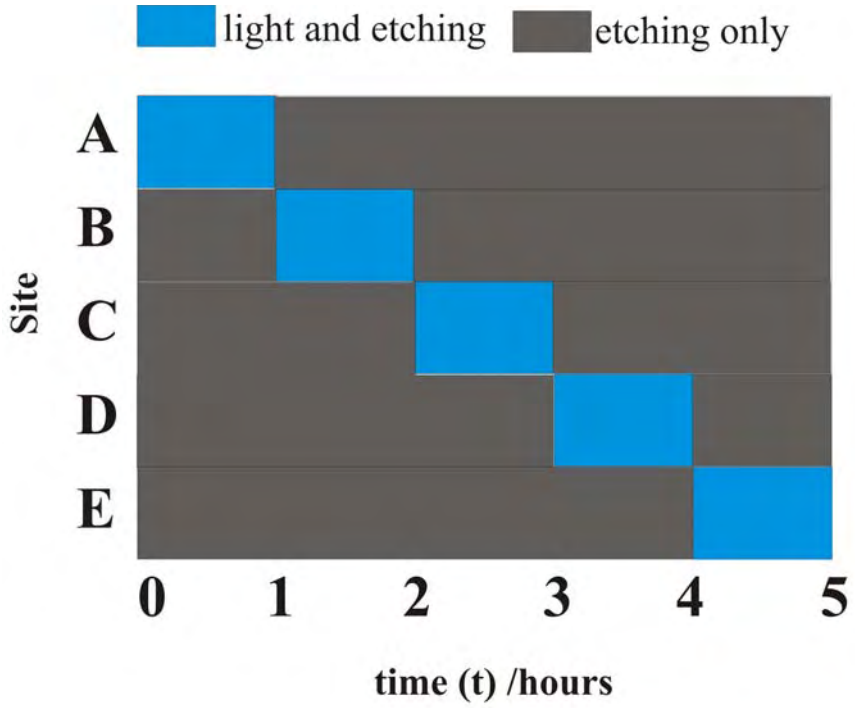

Fig. 4.3. Schematic to illustrate the temporal sequencing of illumination used at each etch site A-E.

4.3.3 Latent LIFE (532nm)

The experiment described in (4.3.2) was repeated using a frequency-doubled solid state laser at 532nm. This laser was used to replace the argon ion laser which had two large cooling fans built-in. It was felt that these fans may be causing undesirable vibrations that might affect any patterning processes occurring. Due to the difference in wavelength and therefore absorptivity in the Fe: doped crystals this experiment was carried out to ensure that the effects would be the same as those seen previously using light of 488nm wavelength.

4.3.4 Fe: Dopant concentrations

The effects of other Fe: dopant concentrations were then investigated. A range of dopant concentrations (0.01%, 0.03% 0.05%, and 0.1%) Fe were chosen for this

experiment. Before experiments were carried out a spectrophotometer was used to record the absorption characteristics for the different dopant concentrations and these results can be seen in fig. 4.1. The experiment described in (4.3.3) was then carried out for all chosen dopant concentrations.

4.3.5 Exposure time

In this experiment the effects of varying the exposure time are investigated for one dopant concentration, the purpose being to build up a picture of how the structures develop with time. Due to the large variety of features seen in the previous experiments the 0.1% Fe samples were chosen. In this experiment the first sample was placed in the setup as in fig. 4.1, and then illuminated at 532nm in the presence of etchant for 5 minutes. The apparatus was then disassembled and the sample was examined. A new sample was then placed in the cell and the procedure was repeated for illumination times of 10, 20, 40 and 80 minutes.

4.3.6 Ion beam milled sample

Following analysis of the results achieved from the previous experiments it was felt that it was necessary to check that the growth of these structures was not being influenced by surface defects such as those that might by induced during the polishing process. In order to check this, ion beam milling was used to remove approximately the top 1-2 μm from the –z face of a 0.1% Fe doped sample. A single site was then etched in the presence of light for 20 mins.

4.4 Results

On the completion of each of the experiments the samples were examined using optical and scanning electron microscopy (SEM), and an alphastep profilometer. In some cases a modified atomic force microscope (AFM) technique was used to determine the surface charge associated with the features which will be described later in section 4.5.2.

4.4.1 Initial experiment

The observations made from this experiment confirmed that the laser power levels were in the correct range to induce partial frustration of etching for a sample of 0.05% Fe: dopant concentration. Partial frustration was observed for the intensity range 330Wcm^{-2} and below. So that a large intensity range could be observed on each site the laser beam was loosely focused. The sub-micron filamentary structures associated with partial frustration were observed at intensities of the range ~ 6 Wcm^{-2} and below.

4.4.2 Latent LIFE (488nm)

The samples were first examined using an optical microscope, where under high magnification (x1000) the sites were seen to be made up of micron scale structures. Figure 4.4 shows an example of an image obtained using an optical microscope and it is clear that at the edge of the illuminated region that the structures follow three directions that are approximately 120^{o} apart.

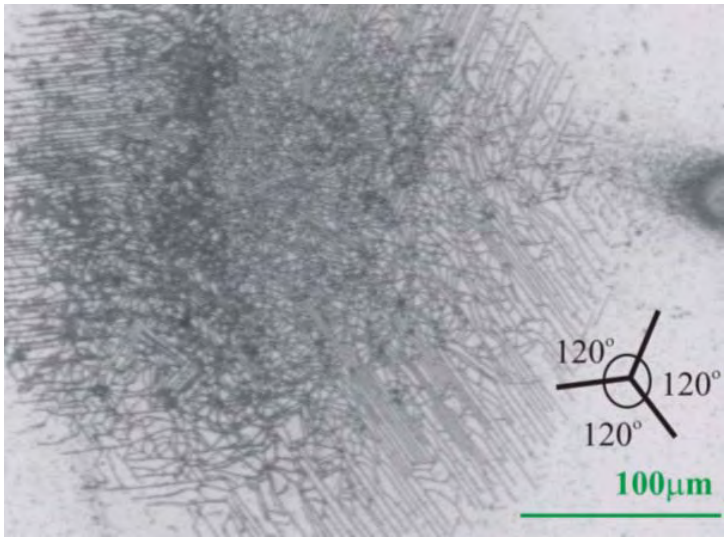

Figure 4.4. Optical microscope image of site B, showing that the pattern appears to follow 3 preferred directions.

The sample was then examined using an SEM, where an overview of all sites clearly showed that the site that was etched in the presence of light during the first hour (A) was larger than the sample etched during the second hour (B) and this characteristic followed for the subsequent sites. An overview of all sites can be seen in fig. 4.5.

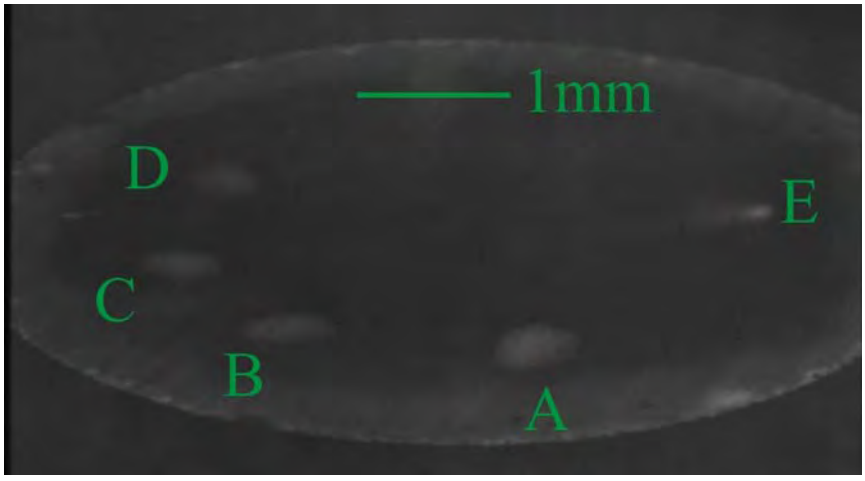

Fig. 4.5. SEM image showing overview of all sites (A-E).

Under closer examination with the SEM it was observed that in some regions of the sites the structures had grown as long parallel lines and that these lines in some places

also had a structure which will be referred to as “teeth”, and that these teeth seem to be periodic or show similar quasi-periodic structuring. Examples of these parallel lines and “teeth” can be seen in fig.4.6.

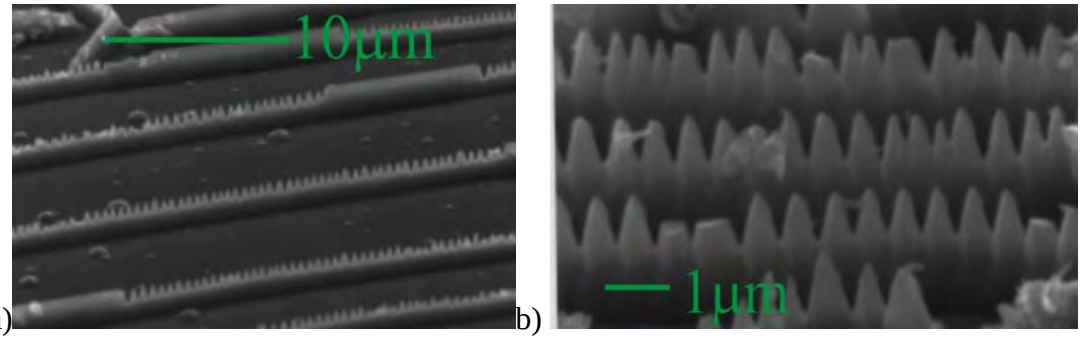

Figure 4.6. Examples of features of interest from experiment 4.3.3.

The alphastep profilometer measurements were used to examine the respective heights of the material left unetched at each site. Fig. 4.7 shows the results from the five sites that were illuminated during the experiment described in (4.3.2), as well as an area labelled U which corresponds to the etch depth of an unilluminated region. It is clear that there is a systematic trend in the measured heights of material that remains unetched, and that this reflects the illumination sequencing adopted. Figure 4.7(a) shows the raw data, while fig. 4.7(b) has been replotted on a semi-logarithmic scale. The linear fit obtained indicates that a characteristic time constant applies to the process by which the etching can remain partially frustrated, and this lies in the region of a few hours, at this temperature, and dopant concentration. The difference in heights of sites U and A shows that the frustration of etching does not occur immediately when a site is illuminated.

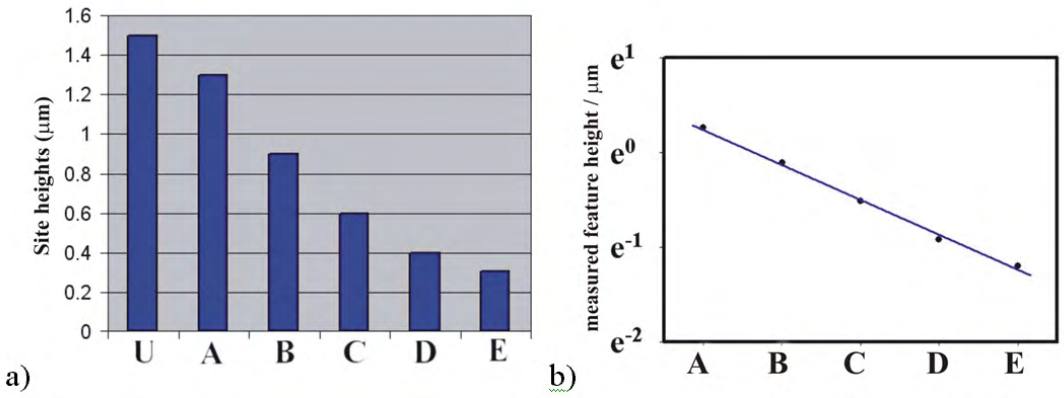

Fig. 4.7. Histogram of heights of etched material at each site (A-E), presented as a linear plot (a), and a semi-logarithmic plot (b).

4.4.3 Latent LIFE (532nm)

The initial results at 532nm showed similar features and patterns as expected. Some examples of the features formed can be seen in fig. 4.8 and has been assembled to include features of interest from all experiments.

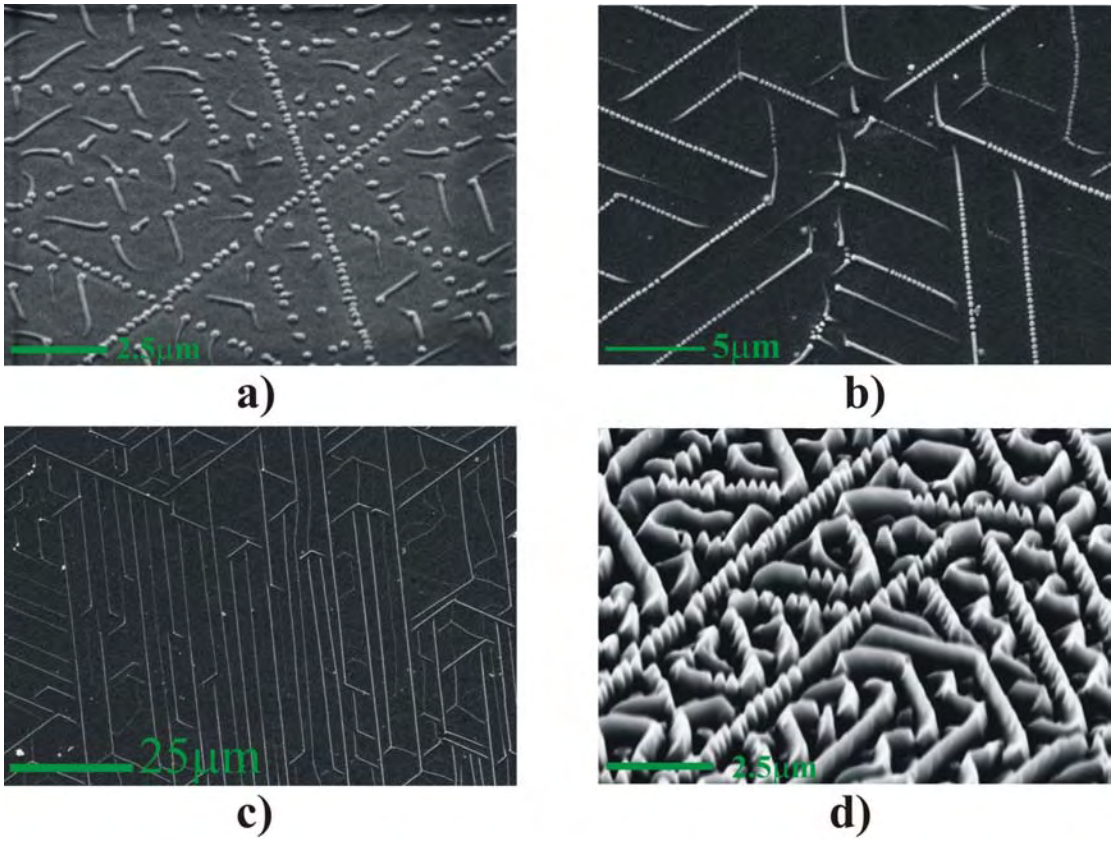

Fig. 4.8. SEM images of various features of interest

Figure 4.8 shows:

a) initial growth sites in the early stages of development

b) these initial sites can grow to follow 3 preferential directions

c) some areas show many lines growing parallel to each other

d) many of these lines are seen to consist of smaller “teeth” like structures

4.4.4 Fe:Dopant concentrations

Figures 4.9 and 4.10 show SEM images of the sample used at each end of the range of dopant concentrations used. The difference in appearance is immediately apparent, both the overall site size and the smaller structures that make up the site are of greatly different dimensions. In the case of the 0.01% Fe doped samples both the absorptivity and hence the amount of photoexcited charge will be lower than that of the 0.1% Fe

doped sample. This would therefore lead to less initial sites for the structures to originate from but would leave the structures that do form space to grow freely. In the case of the 0.1% Fe doped sample the increased absorptivity and amount of free charge will result in a greater density of sites for the initial growth sites. This will in turn result in the growth of the structures being restricted.

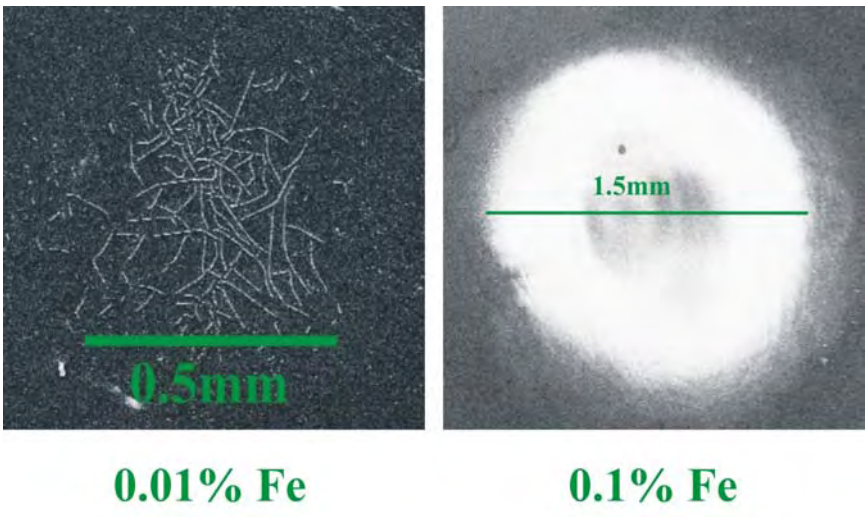

Fig.4.9. Comparison of spot and feature size for dopant concentrations of 0.01% and 0.1% Fe

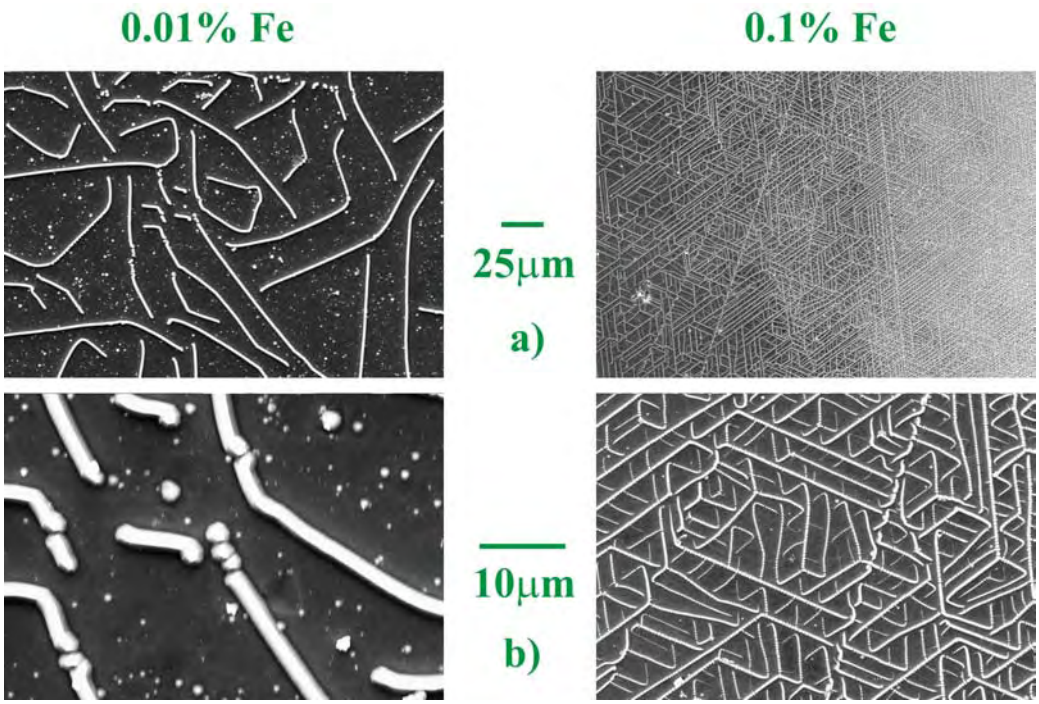

Fig. 4.10. Comparison of pattern and feature size for 0.01% Fe and 0.1%Fe

where a) x5000 and b) x20000

4.4.5 Exposure times

The variations in exposure time also lead to variations in site and feature size as can be seen from figures 4.11 - 4.13. It seems that the structures grow continually and fill in the gaps if they have the freedom to do so. The sites appear to grow from the centre and spread outwards with time.

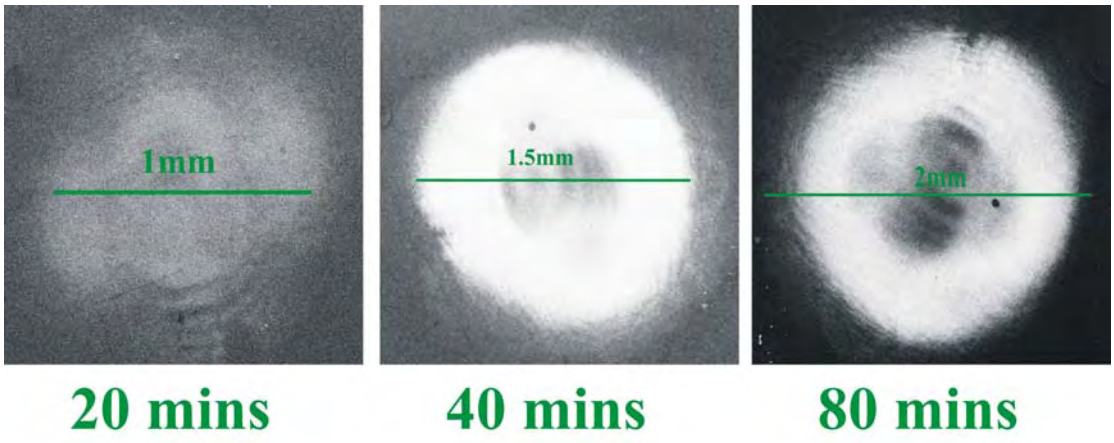

Fig. 4.11. Comparison of spot size with exposure time for 0.1% Fe doped sample.

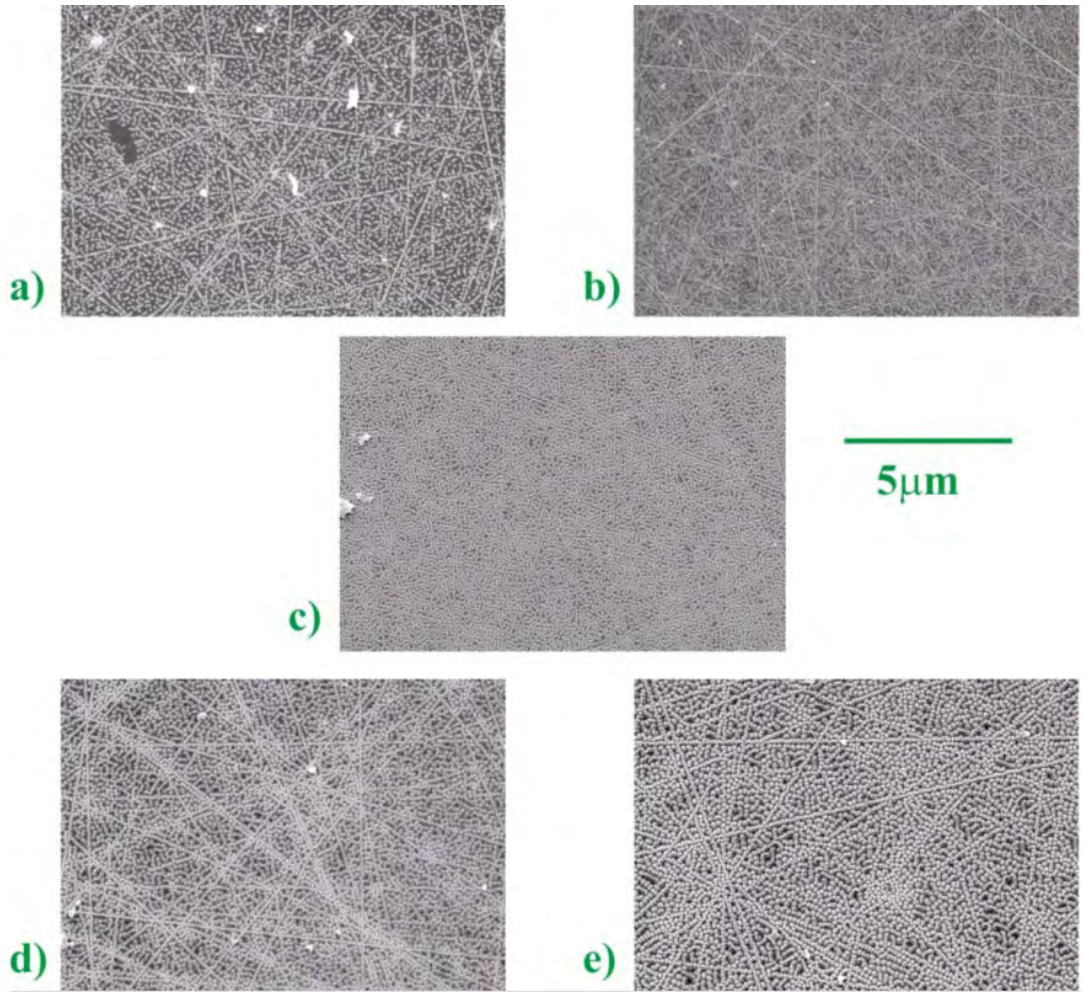

Fig. 4.12. Development of pattern with time for 0.1% Fe, with a=5mins, b=10mins, c=20mins, d=40mins, and e=80mins. Magnification = 5000 times.

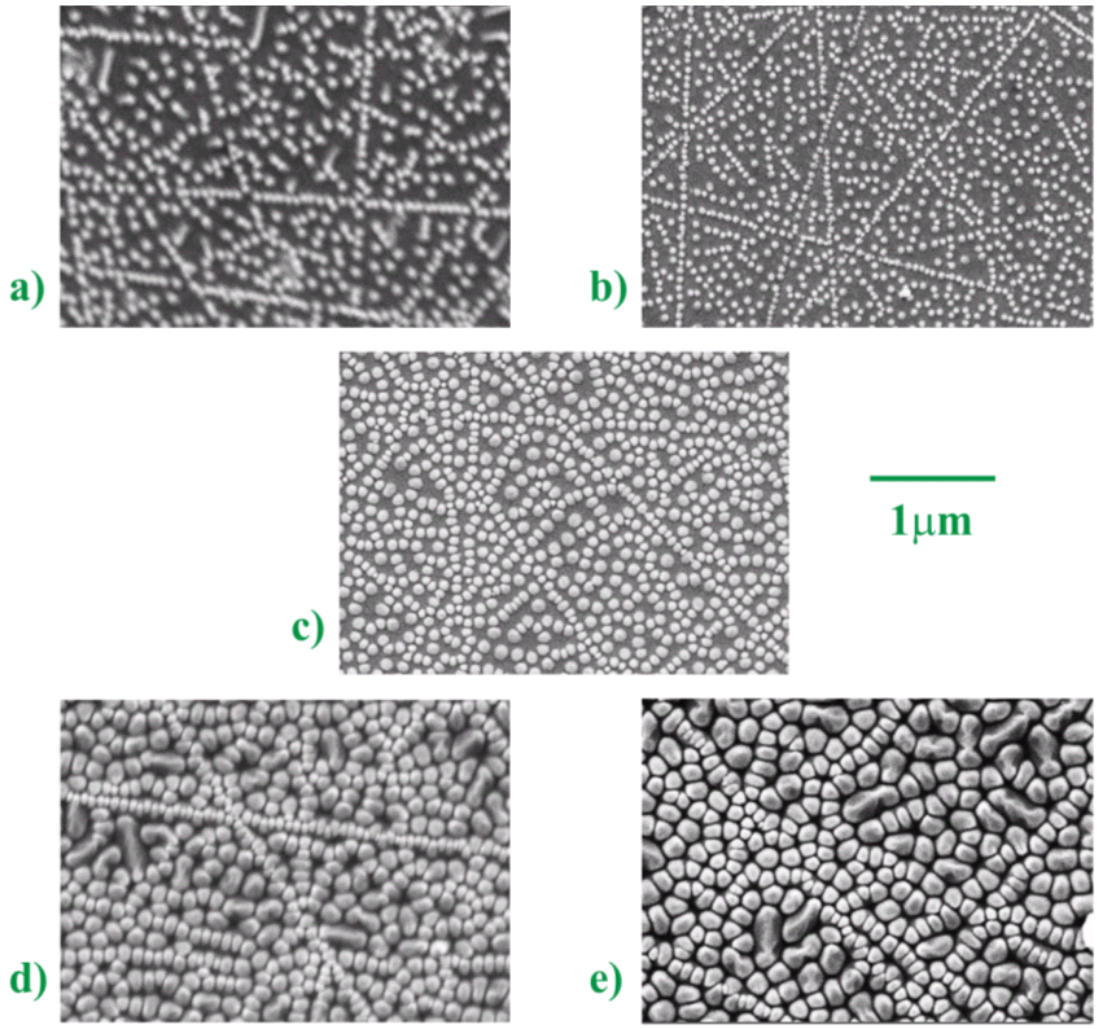

Fig. 4.13. Development of pattern with time for 0.1% Fe, with a=5mins, b=10mins, c=20mins, d=40mins, and e=80mins. Magnification = 20000 times.

4.4.6 Ion beam milling

Figure 4.14 shows a comparison between a sample that has been etched as supplied by the manufacturer and a sample that has had the top1-2μm of the –z face removed using ion beam milling.

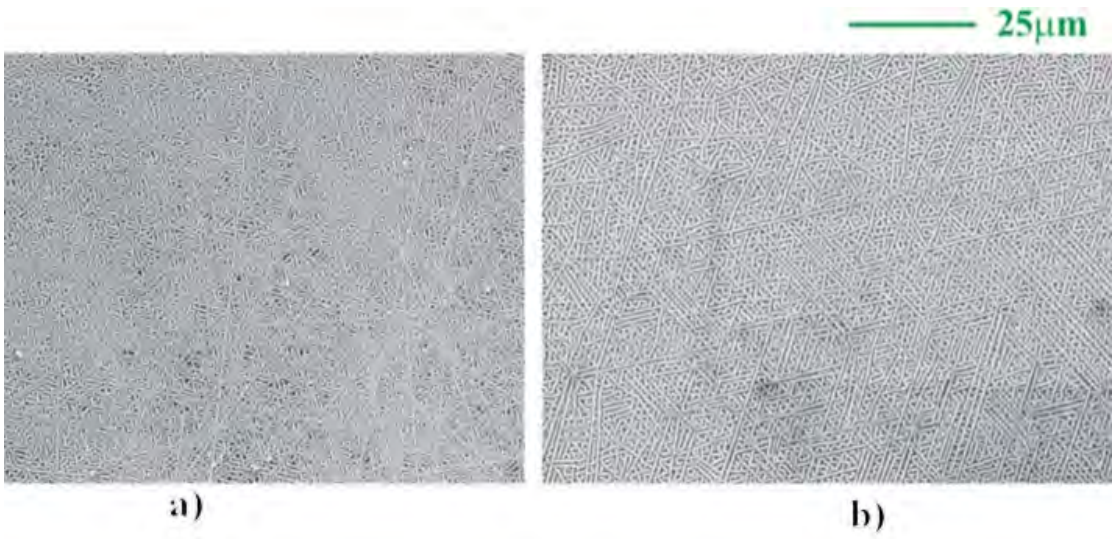

Fig. 4.14. O.1% Fe doped LN etched for 40 mins in the presence of light, a) is a sample as supplied, and b) has had 1-2μm of the –z face removed

It can be observed that the features that have characterised the discussions so far are visible and very similar. However, the features that we have attributed to surface damage, most likely being caused by the polishing process, have been removed in the sample that has been ion beam milled. This has confirmed that the structuring patterns are an intrinsic feature of the overall process, and are not results of surface defects induced by polishing.

4.4.7 Irradiance levels

Figure 4.15 shows a sequence of SEM images as a function of distance from the centre and therefore distance from I_0 as calculated from eqn. (4.2).It is observed that the higher irradiance levels lead to a higher density of initial growth sites. However another interesting observation to be made is that there appears to be structure growth even where the irradiance levels would appear to be negligible (i.e. $< 10^{-10}Wcm^{-2}$).

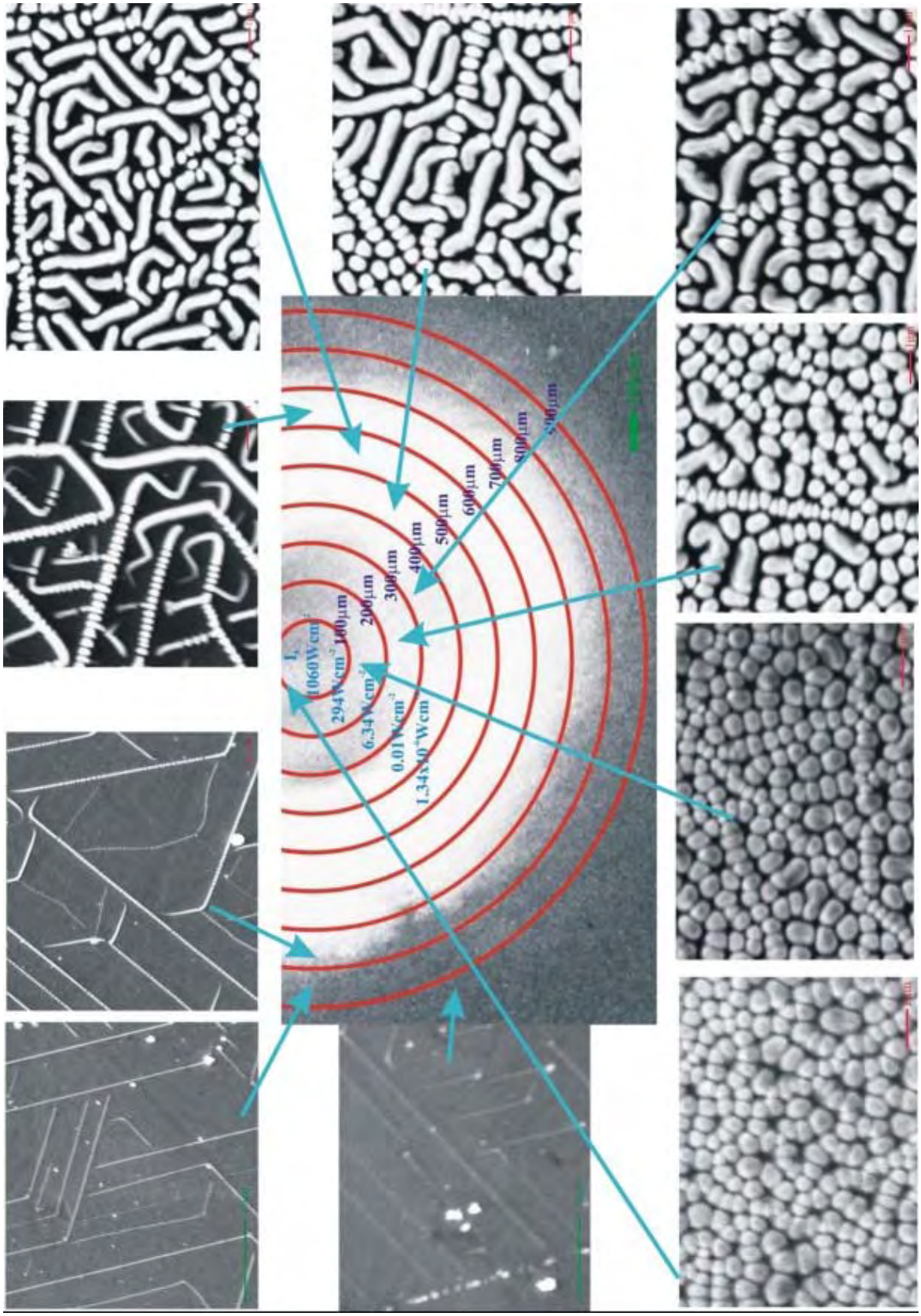

Fig. 4.15. Features as a functions of distance from peak intensity I_0

4.5 Analysis of results

4.5.1 Fourier transforms

An important step in understanding the microscopic structure formation process was to investigate whether the structured growth followed any preferential directions, or had repetitive structure, spacing or size. It was important to be able to then determine whether these factors were determined by irradiance, Fe: dopant concentration or time.

An analysis method using two-dimensional Fourier transforms (2DFT's) was developed. A Fourier transform (FT) is a mathematical function that can be used to convert a spatial domain pattern into a frequency domain pattern; in the case of 2D images it is necessary to use the 2DFT. A routine was written in collaboration with Jeffery Scott (another member of the research group) that included the use of a predefined 2DFTfunction in a computer software pack (MATLAB).

Initial results as shown in fig 4.16, gave further evidence towards the idea that in some regions of the illuminated sites, structures form along three preferential directions.

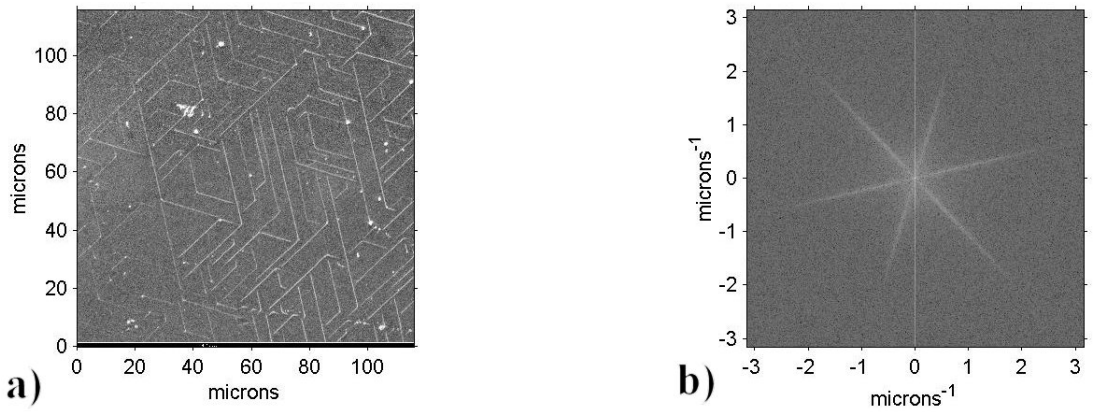

Fig.4.16. SEM image (a) and corresponding 2d-Fourier transform (b) taken from an area close to the edge of the illuminated site for a 0.1% Fe doped sample exposed for 40 mins.

This result shows that although there are preferential directions present because each of the directions is represented by an extended dense pattern of points rather than an individual point, in each direction there are a range of frequencies present.

Fig. 4.17 shows an image taken ~100μm closer to the centre of the illuminated region than the previous figure.

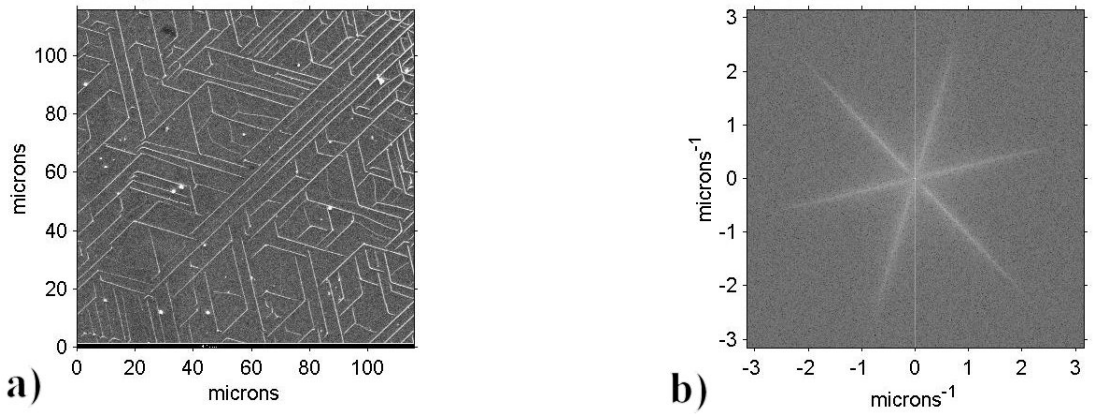

Fig.4.17. SEM image (a) and corresponding 2d-Fourier transform (b) taken ~100μm from the edge of the illuminated site for a 0.1% Fe doped sample exposed for 40 mins.

The image above shows that the pattern of dots making up the arms of the FT (fig.4.17b) appear wider than in the previous case. This would indicate that the

features of (fig. 4.17a) are deviating from the preferred directions more so than in the case of (fig. 4.16).

Fig. 4.18 shows another image and its corresponding Fourier transform for the case where the region chosen is close to the centre of illumination.

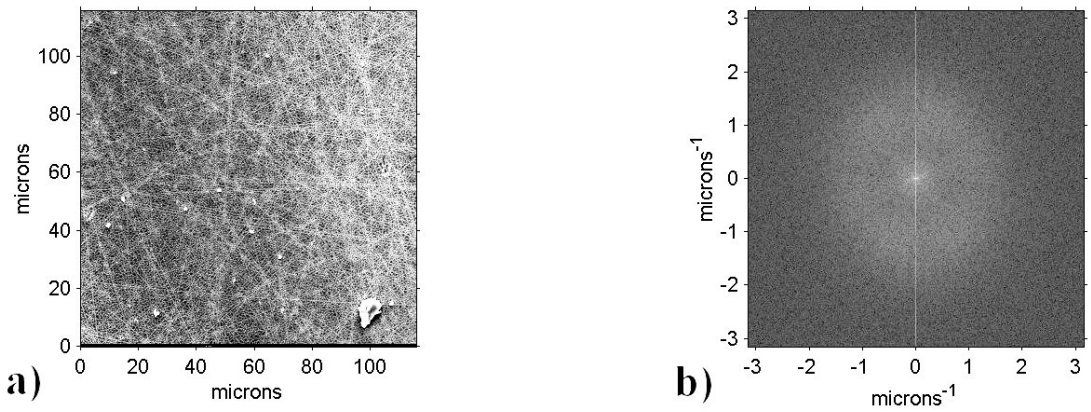

Fig.4.18. SEM image (a) and corresponding 2d-Fourier transform (b) taken from an area close to the centre of the illuminated site for a 0.1% Fe doped sample exposed for 40 mins.

In this image it is seen that there are no longer any lines representing the preferential directions as indicated previously. When examined closely a circular pattern can be seen which indicates that there is still an overall scale-length for the features produced however.

An explanation for the resulting differences in the Fourier transforms as a function of the distance from the centre of the illuminated site could be that fig.4.16 shows an area where there are few sites of initial growth and the structures can grow relatively freely and follow the preferential directionality we observe. However it can be seen that as the level of irradiance is increased that the number of initial growth sites also increases resulting in structures being allowed less freedom to grow and not always able to grow in the preferred directions. This therefore results in the widening of the

Fourier transform pattern and a schematic representing this process can be seen in fig. 4.19. At the centre of the site where the irradiance levels are at their highest, the density of initial growth sites is so great that there is very little freedom to grow at all. This therefore results in a Fourier transform pattern of repetitive feature size with no apparent preferential growth direction.

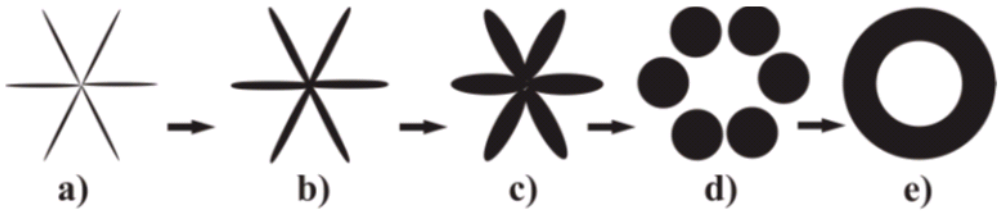

Fig. 4.19. Schematic showing the changing shape of the Fourier transform.

Figure 4.20 shows the gradual change in the shape of the Fourier transform pattern as the illuminated site is examined as a function of distance from the centre and therefore peak irradiance level.

A further step was taken to gain quantitative results from the Fourier transform data. This involved recording pixel value data along an imaginary line originating from the centre of the transform image, and then rotating this line by 1 degree and adding the pixel data for the new line to that of the original. This step is repeated for 360^{o} and results in a 1 dimensional line representing the sum of all the pixel data for a 2DFT. A Gaussian curve has then been fitted to the broad peak in the data where the peak of this curve corresponds to the most regularly occurring spatial frequency of the original image. Fig.4.21 shows this data for all regions as a function of distance from the peak intensity for a 0.1% Fe: doped sample that has been etched in the presence light for 40 mins. Figure 4.22 shows a comparison of this data obtained for samples

that have been etched in the presence of light for 20, 40 and 80 minutes. This indicates that there is a trend of increasing scale-length for the features as the distance from the site centre increases.

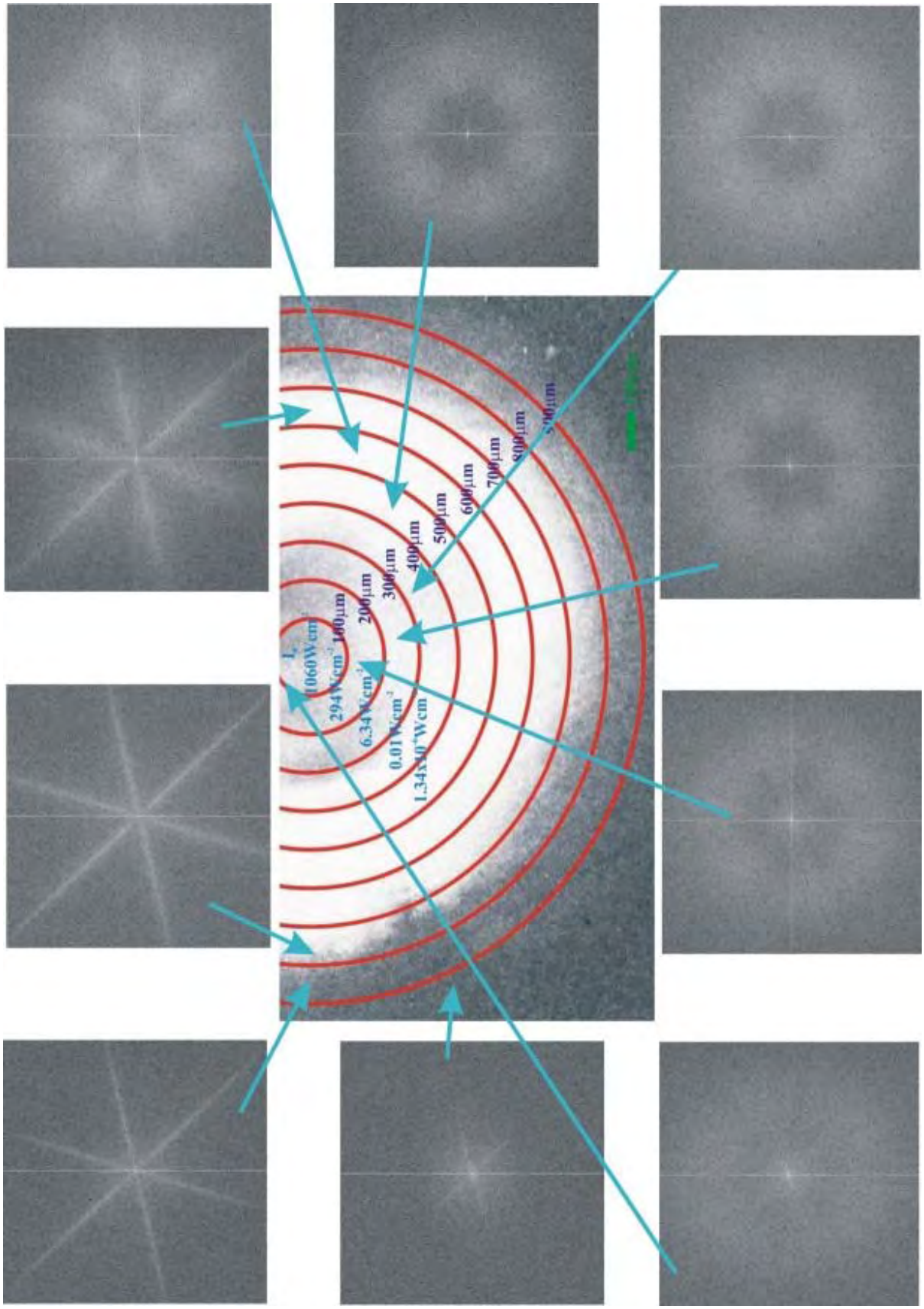

Figure 4.20. Fourier transformations as a function of distance from peak intensity I_0

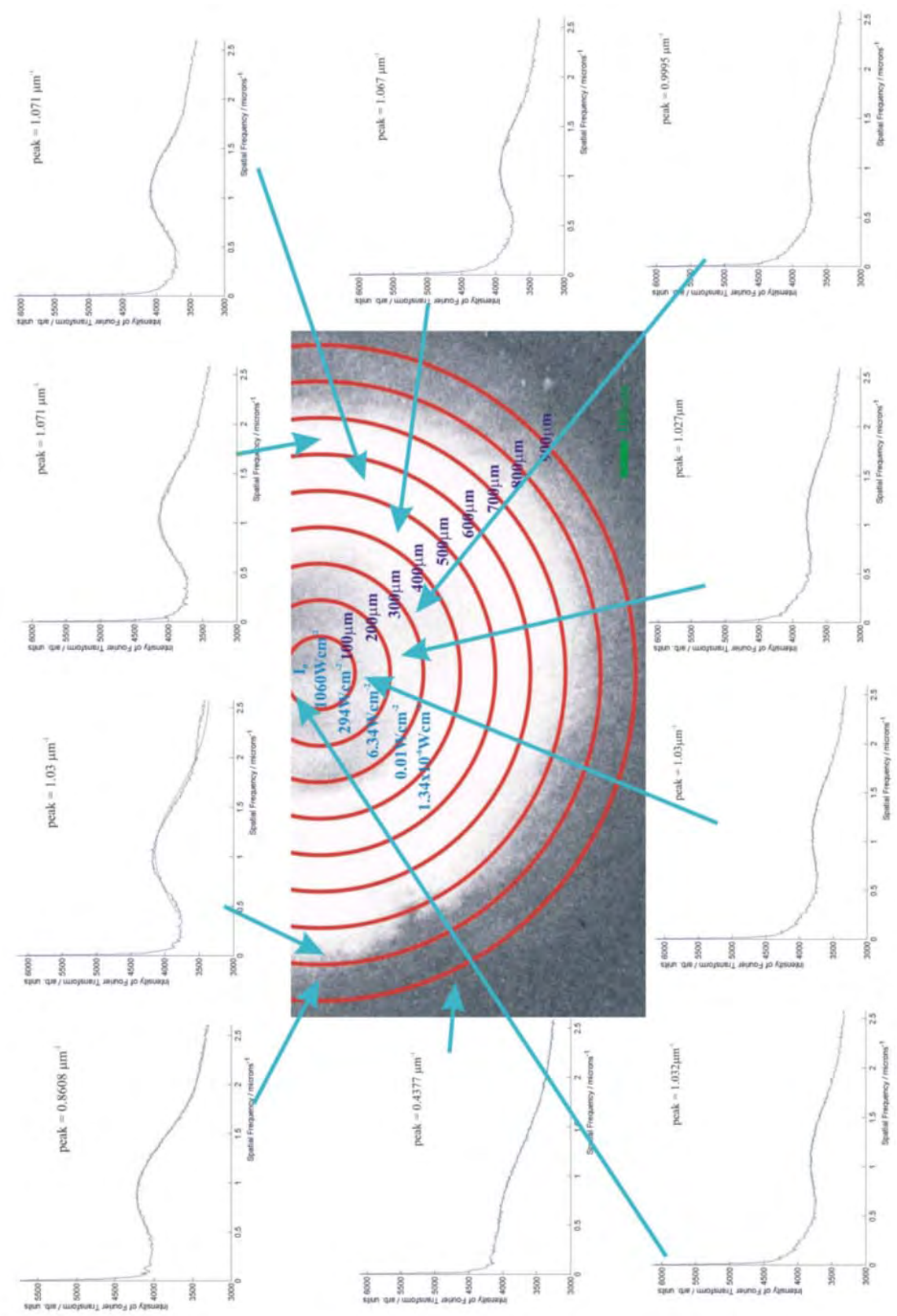

Fig.4.21. Sum of Fourier transformations as a function of distance from peak intensity I_0

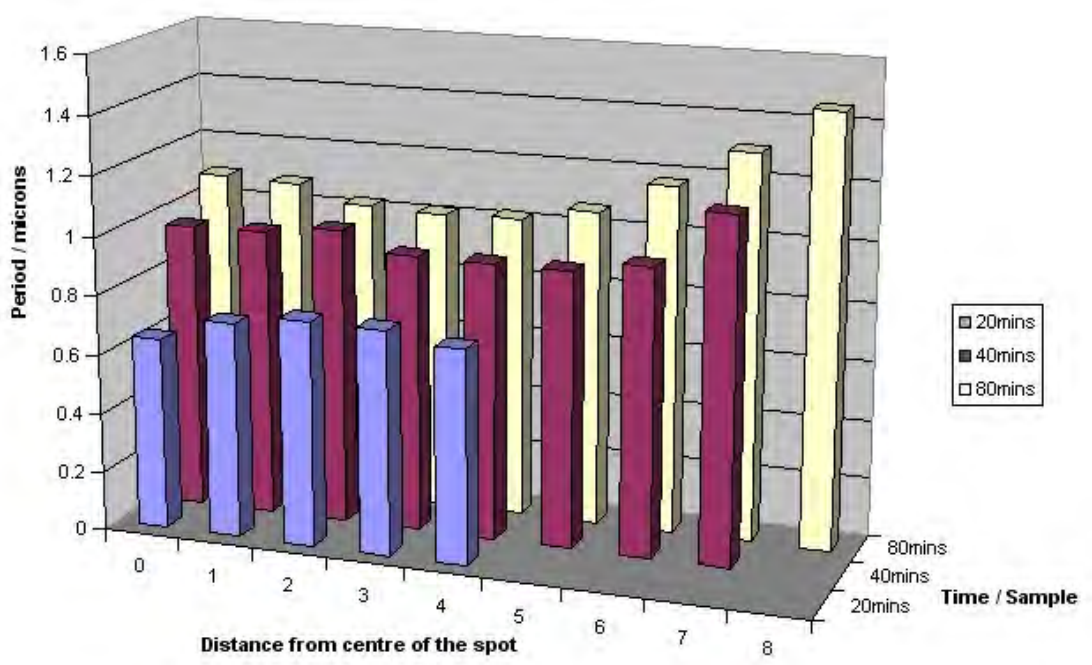

Fig.4.22. Comparison of period of features as a function of the distance from the centre of the site, for sites etched for 20, 40, and 80 minutes.

4.5.2 Localized charge force microscopy

The principles of force microscopy [Binnig86] and the imaging of electrostatic charge using a modified technique have been described in detail previously [Stern88, Martin87, Terris89, Terris90]. This technique involves applying a voltage between the force microscope tip and the sample. The technique has previously been used to image topographical features on both conducting [Erlandsson88] and insulating [Martin88] surfaces and also for the imaging of ferroelectric domain walls [Saurenbach90].

A schematic for this modified technique can be seen below in fig. 4.23. This method has a lever/tip which is mounted on a piezoelectric bimorph that is oscillated near its resonant frequency. As the tip scans above the sample surface, variations in the tip-to-

surface force gradient will alter the effective spring constant of the lever changing its resonant frequency. In this system there are three contributors to the force gradient:

1. the electrostatic force on the tip due to surface charge distribution
2. the electrostatic force due to a voltage applied between the tip and the back electrode
3. the van der Waals force between the tip and the sample

When there is a charge present on the surface, the force gradient will increase as the tip scans over the charged region due to the attractive interaction between the surface charge and the induced charge on the tip. The amount of charge on the surface can be estimated by measuring the force on the tip as a function of distance as the tip approaches a charged surface. The force is obtained by measuring the static tip deflection and assuming a value for the spring constant which can be calculated from geometry [Stern88].

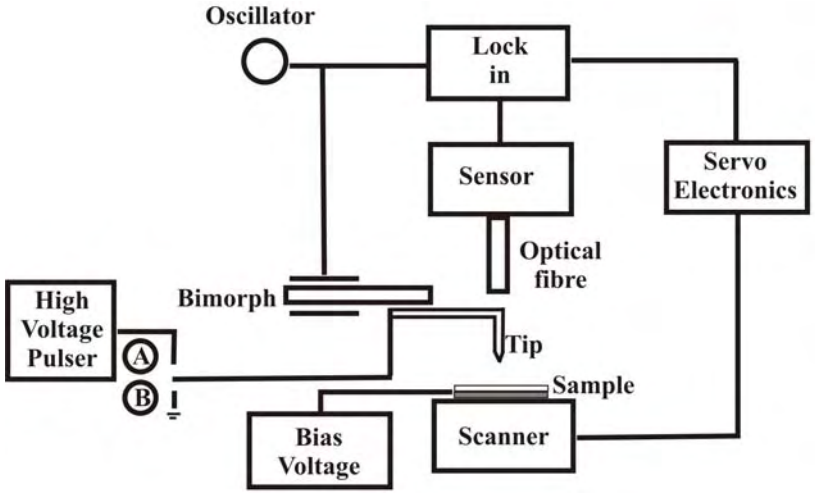

Fig. 4.23. Schematic of the force microscope. Charge is deposited on the sample with the switch in position A, and imaging of the charged surface is carried out with the tip grounded, in position B [Stern88]

The method described above has been used to examine structures created by the experiments reported in this chapter. This analysis was carried out by the research

group of Prof. Karsten Buse, from the University of Bonn, Germany. The results obtained from a 0.01% doped Fe sample can be seen in figures 4.24 and 4.25.

a) b)

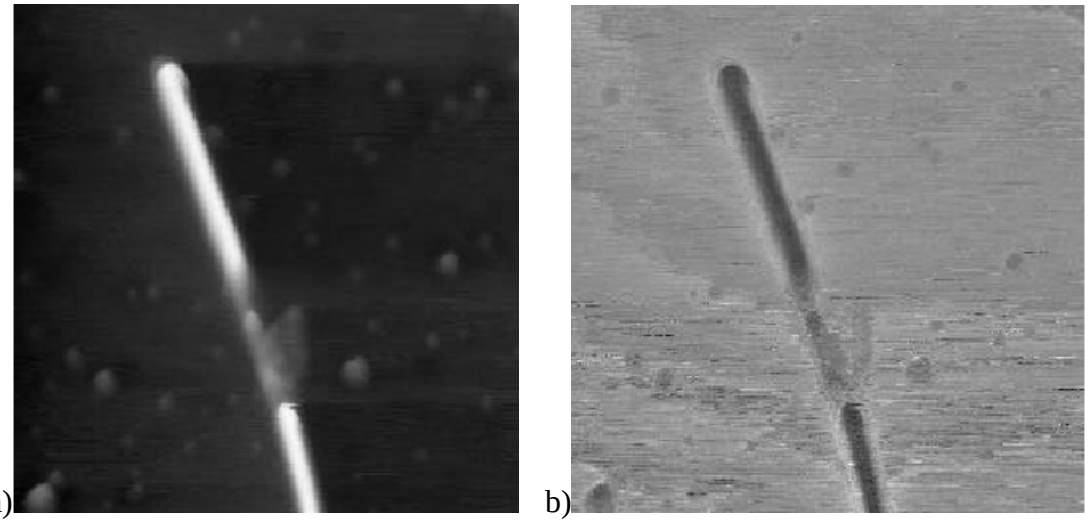

Fig. 4.24. Topography (a) and charge profile (b) obtained using force microscopy, for a 0.01%Fe doped sample

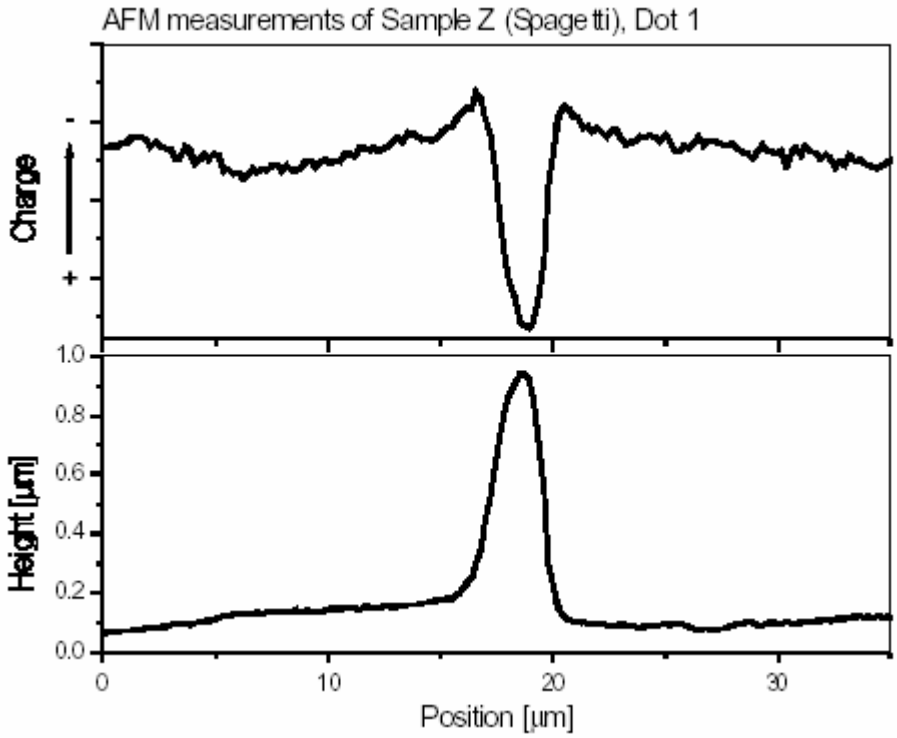

Fig. 4.25. Charge and height profiles obtained using force microscopy corresponding to the images seen in fig.4.24.

By analysing figures 4.24 and 4.25 it can be seen that the images show a negative surface (-z) with an etch resistant structure that stands above the surface and is positively charged.

4.6 Explanations

The suggested process that leads to the formation of these structures has been built up through the observations reported in this chapter. The light induced photovoltaic current leads to the free electrons from the Fe dopant being excited. These electrons then move through the crystal along the *c* axis with a preferred direction of motion. It is the inhomogeneities and their local electric fields that determine the charge transfer mechanism [Kanaev98]. As suggested by [Kanaev98], there is no significant light absorption in the perfect crystalline regions; absorption only takes place where defect regions exist. These discretely spaced inhomogeneities serve as donors and traps for electrons. Photovoltaic current flowing in one direction and only through defects leads to accumulation of charges and can subsequently lead to repolarisation [Nagata00]. It is this repolarisation that leads to the creation of the structures seen that can be referred to as microdomains. The revelation of the patterns is due to the preferential etching as discussed in chapter 3.

Once the domain has been inverted the etching process “freezes” the domain in the state. The domains propogate along their preferred direction until they meet and are repelled by a similar charge. If space permits they then change direction to follow one of the other preferential directions. Although the reasons why the domain structuring follows 3 preferential directions is not fully understood it is no surprise that 3 preferential directions are apparent because Neumann’s principle (*The symmetry*

elements of any physical property of a crystal must include the symmetry elements of the point group of the crystal [Lovett].) must clearly apply here.

The main effect contributing to the creation of these structures is the bulk photovoltaic effect. This effect is dependent on the amount of free charge so is therefore dependent on levels of irradiance, exposure time and dopant concentration.

There is much evidence supporting the theory that these structures are poled domains. This evidence includes:

1. Structures are etch resistant (*as are +z oriented domains*)

2. Structures are positively charged (*as are +z oriented domains*)

3. Structures have the < μm width that is associated with domains [Terabe03]

4. Structures are still crystalline (as determined by Raman spectroscopy)

Following the observations made an attempt was made to develop a simple model for the behaviour of the pattern of the features as they grow. The aim was to limit the model to a simple set of rules, which were derived from the observations taken from SEM images and the Fourier transforms. The initial set of rules was that:

1. Lines grow from dots

2. Lines can propagate only along one of three directions, at 120^{o} to each other

3. Lines cannot touch or cross over each other

4. Lines may change direction to avoid another line.

5. Line growth stops when a crossing would inevitably occur

The implementation of these rules into a model was carried out by J.G.Scott, another member of the research group. For completeness some example results from this model can be seen in appendix 2.

4.7 Summary

An in-depth study of the parameters affecting LIFE has been carried out. It has been observed that structuring is dependent on:

- exposure time
- Fe dopant concentration
- level of irradiance

It has also been observed that the structures:

- propagate along one of three preferential directions each 120^{o} apart
- are most probably poled domains

4.8 References

[Barry99] Barry, I. E., Eason, R.W., Cook, G. (1999) *Applied Surface Science*, **143,** 328.

[Binnig86] Binnig, G., Quate, C.F., and Gerber, C. (1986) *Physical Review Letters*, **56,** 930.

[Boyland00] Boyland, A. J., Mailis, S., Barry, I. E., Eason, R. W. and Kaczmarek, M. (2000) *Applied Physics Letters*, **77,** 2792-2794.

[Erlandsson88] Erlandsson, R., McClelland, G.M., Mate, C.M., and Chiang, S. (1988) *J.Vac.Sci.Technol.,* **A6,** 266.

[Glass74] Glass, A. M., von der Linde, D., and Negran, T.J. (74) *Applied Physics Letters*, **25,** 233.

[Joannopoulos] Joannopoulos, J. D., Meade, R.D., Winn, J.N. (1995) *Photonic crystals*, Princeton University Press, Princeton.

[Kanaev98] Kanaev, I. F., and Malinovsky, V.K. (1998) *Ferroelectrics*, **218,** 27.

[Kashyap] Kashyap, R. (1999) *Fibre Bragg Gratings*, Academic, San Diego, CA.

[Lovett] Lovett, D. R. (1999) *Tensor Properties of Crystals*, Institute of Physics Publishing, Bristol, UK.

[Martin87] Martin, Y., Abraham, D.W., and Wickramasinghe, H.K. (1987) *Applied Physics Letters*, **52,** 1103.

[Nagata00] Nagata, H., Ichikawa, J., Sakima, M., Shima, K. and Haga, F. M. (2000) *Journal of Materials Research*, **15,** 17-20.

[Saurenbach90] Saurenbach, E., and Terris, B.D. (1990) *Applied Physics Letters*, **56,** 1703-1705.

[Scott03] Scott, J.G., Boyland, A.J, and Eason, R.W. *to be submitted Nature Materials April 03*

[Siegman] Siegman, A. E. (1986) *Lasers,* University Science Books, Sausalito.

[Stern88] Stern, J. E., Terris, B. D., Mamin, H. J. and Rugar, D. (1988) *Applied Physics Letters,* **53,** 2717-2719.

[Sommerfeldt88] Sommerfeldt, R., Holtmann, L., Kratzig, E. and Grabmaier, B. C. (1988) *Physica Status Solidi a-Applied Research,* **106,** 89-98.

[Svelto] Svelto, O. (1993) *Principles of lasers,* Plenum Press, London.

[Terabe03] Terabe, K., Nakamura, M., Takekawa, S., Kitamura, K., Higuchi, S., Gotoh, Y., and Cho, Y. (2003) *Applied Physics Letters,* **82,** 433-435.

[Terris89] Terris, B. D., Stern, J. E., Rugar, D. and Mamin, H. J. (1989) *Physical Review Letters,* **63,** 2669-2672.

[Terris90] Terris, B. D., Stern, J. E., Rugar, D. and Mamin, H. J. (1990) *Journal of Vacuum Science & Technology a-Vacuum Surfaces and Films,* **8,** 374-377.

[Walker] Walker, S. J., Hagel, D.J. (1999) *Optics and MEMS,* Naval Research Laboratory, Washington DC.

Chapter 5

Total internal reflection switching

5.1 Overview

A novel switching technique has been developed [Boyland01a, Boyland01b], that uses the electro-optic effect to induce a change, Δn, in the refractive index of a ferroelectric material that has been domain-engineered to produce a boundary between two anti-parallel domain regions. When a beam of light is incident on the interface between these oppositely oriented domains at a suitably large angle of incidence, total internal reflection (TIR) can occur for a sufficiently large difference in refractive indices induced between these two anti-parallel domains.

This method of electro-optically induced TIR is a novel approach for achieving high contrast switching, and presents many advantages when compared to existing techniques that use electro-optic deflection at a boundary across which a difference in refractive index is induced [Gahagan99, Li96, Yamada96]. These existing techniques will be discussed further in Chapter 6. The values of induced Δn are typically low for electro-optically addressed interfaces between domain-engineered lithium niobate (LN), so prism-type scanning devices have inherently low angular deflection sensitivity. For grazing geometries however, TIR can be extremely sensitive, and for sufficiently large angles of incidence approaching 90^{o}, the voltages required to induce switching can be of order a few volts. The device can also be used to induce large

angle deflections (~18^{o}) across the interface [Eason01, Barrington03] and this topic shall also be reported later in Chapter 6.

5.2 Switching theory

The operation of the device relies on the angle needed for TIR at an electro-optic interface; this angle is given by the expression below [Hecht]:

$$\sin\theta_{tir} = \frac{n+\Delta n}{n-\Delta n} \qquad \textbf{(5.1)}$$

where the equation relating Δn, and electric field, E, is given by the expression [Lovett]:

$$\Delta n = -\frac{1}{2} r_{33} n_e^3 E_z \qquad \textbf{(5.2)}$$

where r_{33} is the largest electro-optic coefficient accessed by *extraordinary s*-polarised light, n_e is the wavelength dependent value of extraordinary refractive index, and E_z is the value of electric field applied across the sample in the *z*-direction. While these coefficients which relate to *s*-polarised light lead to switching at lower values of E_z, switching will also occur when using *ordinary p*-polarised light, that accesses the r_{13} electro-optic coefficient which has a value approximately 1/3 that of r_{33}, with n_e replaced by n_o, the value of the *ordinary* refractive index. The orientation of *extraordinary s*-polarised and *ordinary p*-polarised light in relation to a LN sample is shown in fig. 5.1.

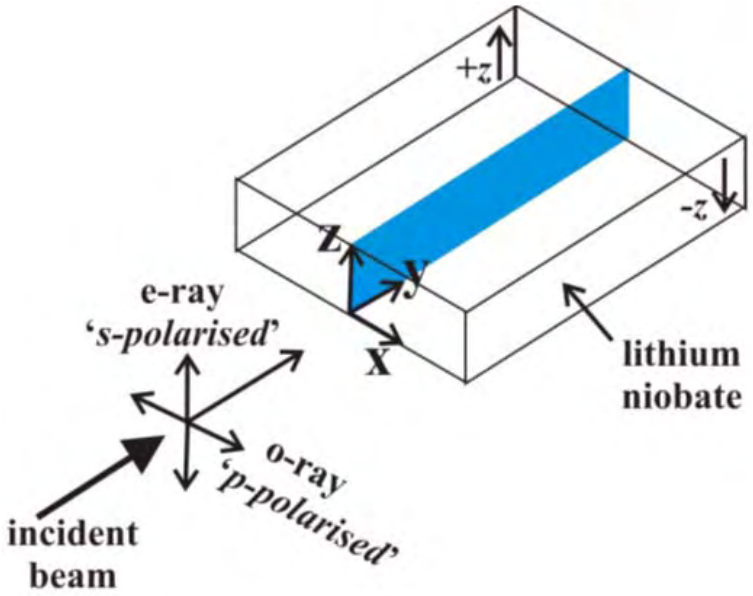

Fig. 5.1. Schematic illustrating the orientation of *extraordinary s*-polarised and *ordinary p*-polarised light in relation to a LN sample

The value used for r_{33} was 30.8 x 10^{-12}mV^{-1} [Weis85] which was the closest published value corresponding to the He-Ne wavelength of 0.543μm, as used for the experimental work, and the value for n_e was 2.2297 evaluated from the Sellmeier equation for this wavelength (see 2.3.3).

Table 5.1 shows values of Δn produced and the angle (θ_{tir}) necessary for TIR for increasing values of applied voltage for a 300μm thick sample, where Δn* is double the value of Δn calculated from eqn. (5.2) as the change in the value of refractive index on each side of the interface is of equal magnitude, but opposite sign. Fig. 5.2 shows the minimum angle required for switching to occur as a function of applied voltage, as calculated using eqns. (5.1) and (5.2). It can be observed from fig. 5.2 that as the angles for TIR approaches 90^o that the applied voltage required to induce a sufficient change in Δn approaches 0V. However because of the grazing angle approach of the incident beam the device length requirements increase with increasing

angle. Therefore for a device of fixed length there is a limit to the incident angle achievable which therefore also limits the minimum applied voltage required for TIR.

Applied voltage (V)	E (Vm^{-1})	Δn^*	θ_{tir} (^{o})
10	3.33×10^4	1.14×10^{-5}	89.82
100	3.33×10^5	1.14×10^{-4}	89.42
1000	3.33×10^6	1.14×10^{-3}	88.16

Table 5.1. Examples of Δn produced and TIR angle implied for a 300μm thick sample as a function of applied voltage

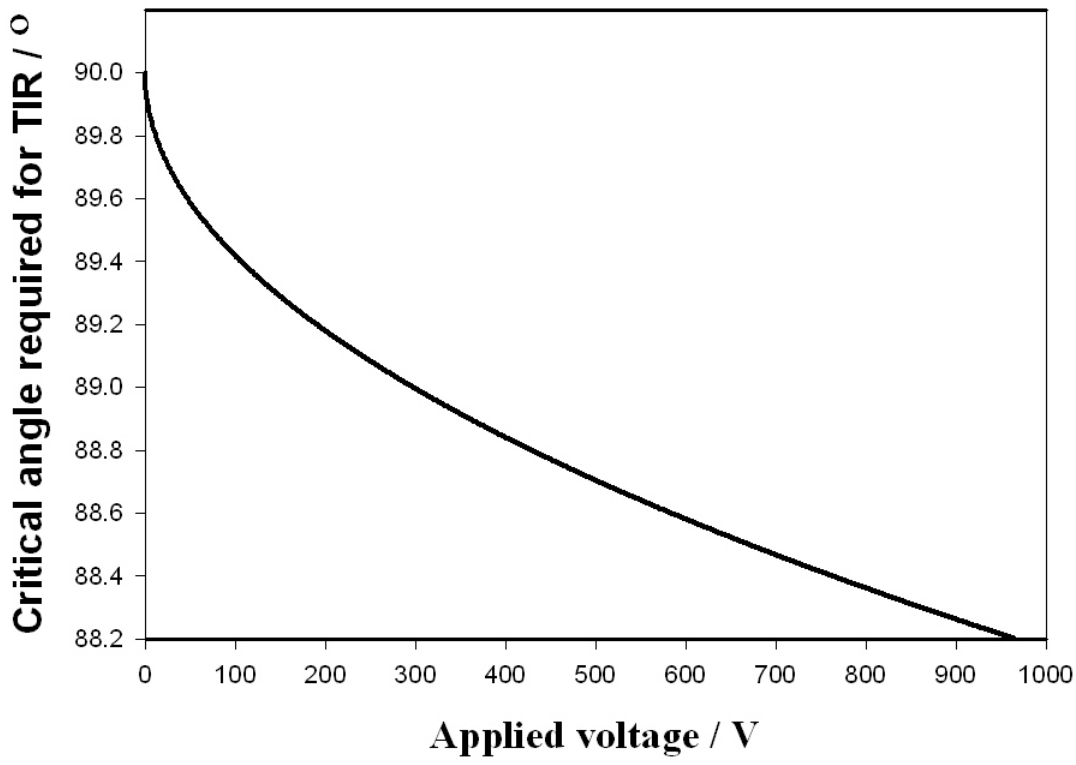

Figure 5.2. Critical angle required for TIR as a function of voltage applied across a device of thickness 300μm

5.3 Experimental procedure

The first device was made from a z-cut sample of congruent LN cut from a commercially available wafer supplied by Yamaju (Japan). The device was of thickness 300μm, and of dimensions 13.5mm by 15mm in the *x*- and *y*- directions respectively. The schematic for the device is shown below in figure 5.3.

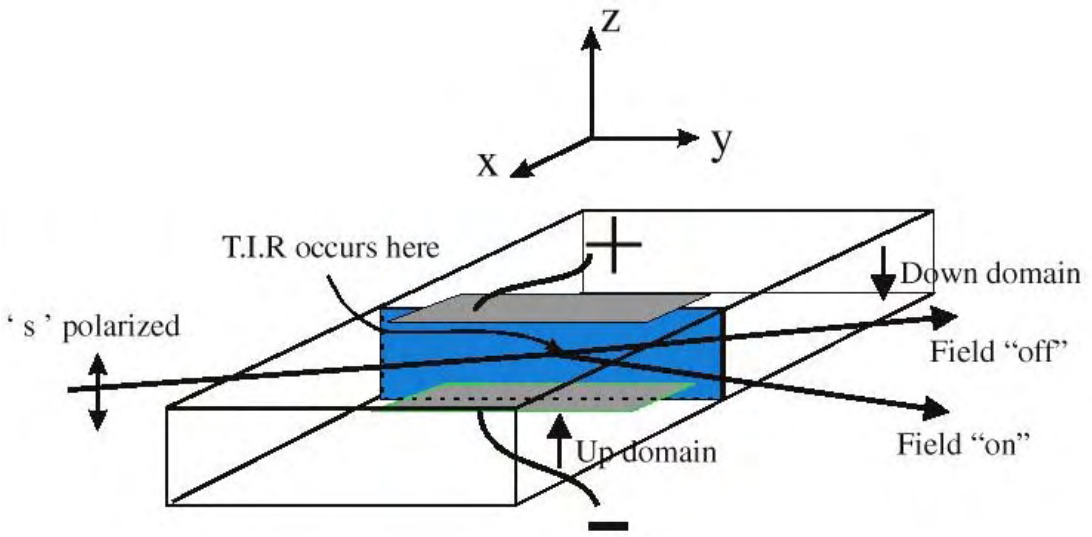

Figure 5.3. Schematic of switch

The two anti-parallel domains were produced by photolithographically patterning the *-z* face and then electric field poling the sample (as described previously in sec 3.2.2). The quality of the interface is an important feature for switching as it determines the contrast ratios achievable and the quality of the output beam. When examined under a polarising optical microscope it was seen to be quite smooth, however under high magnification some variation from absolute straightness was observed. An example of an interface region showing deviation from linearity can be seen in figure 5.4.

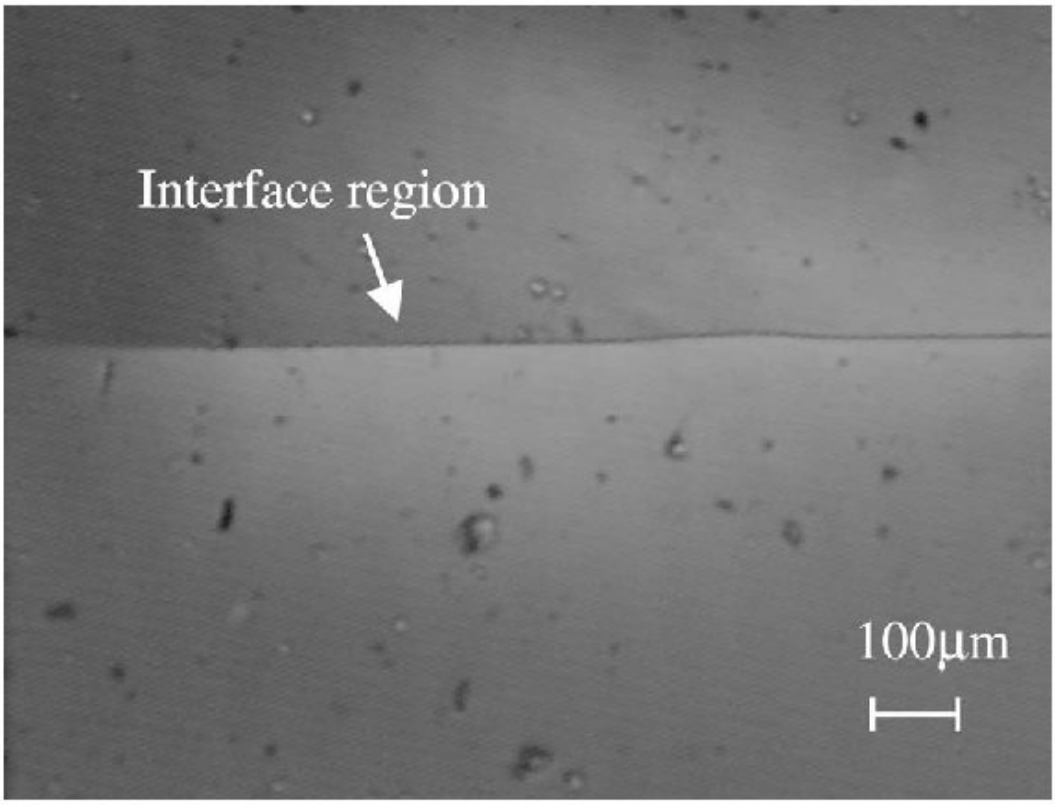

Figure 5.4. Polarising microscope image of interface

This non-uniformity was observed for all samples but its extent was dependent on the poling parameters used, and also varied between individual samples. In an attempt to remove the residual strain at the interface the samples were annealed for several hours at 200^{o}C.

Experimental data was obtained using polarised He-Ne lasers at wavelengths of 0.543μm and 1.52μm. In each case the beam was initially passed through a spatial filter consisting of two microscope objectives (x10) and a pinhole before being focussed into the $LiNbO_3$ sample. Focussing was achieved using a lens of focal length 160mm, which produced a spot size of order 25μm for 0.543μm light, and 64μm for 1.52μm light. The electrodes were fabricated on both -*z* and +*z* faces and were of

dimensions ~12mm x 2mm and were positioned across the domain-interface region. The input and output faces were parallel polished and insulating supports were used to mount the device.

5.4 Theoretical model

A two-dimensional theoretical model for the T.I.R. switch was developed in collaboration with Dr.J.M.Hendricks. The model can be used to predict the switching characteristics expected for any combinations of incident angle (θ_{inc}), wavelength (λ), spot size (ω_0), sample thickness (*d),* and wavelength dependent refractive index (n_e), as determined by the normal Sellmeier equations for $LiNbO_3$ (see section 2.3.3).

The model can be used to characterise the behaviour of the beam incident on the interface for any value of θ_{inc}. A schematic for the interaction of the incident beam at the interface region can be seen in fig.5.5. For the purposes of the model the beam incident along the interface has been divided into a number of slices. The lower part of the figure shows the corresponding intensity profile; it was found that a high level of accuracy could be achieved by using a minimum of 50 slices.

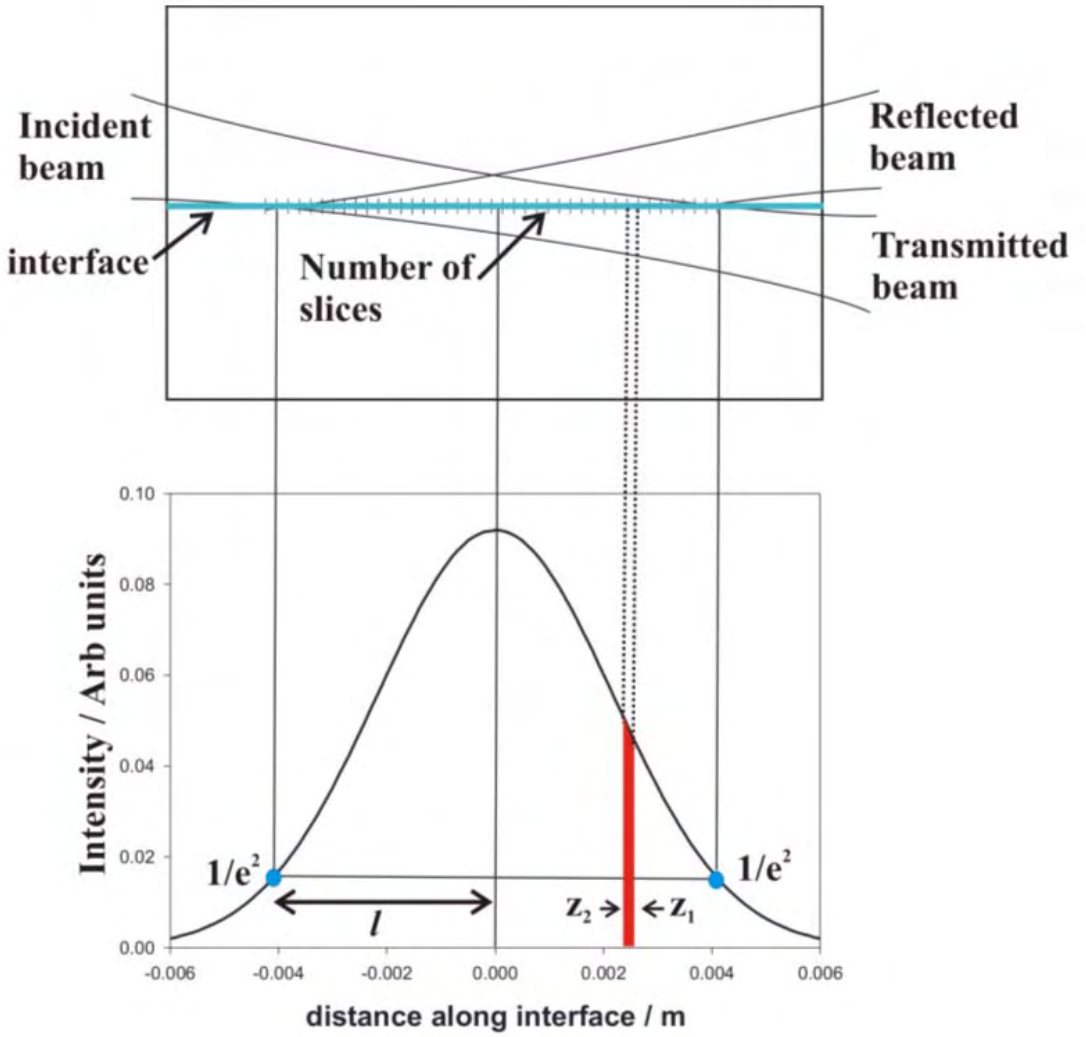

Figure 5.5. Schematic for interaction of the incident beam with interface with the intensity profile of beam projected along the domain boundary for 1.52 μm light with a spot size of 64 μm incident at an angle of 89°

Figure 5.6 below depicts the modelling results showing the extent to which the $1/e^2$ beam contour spreads at the interface due to the grazing angle of incidence and yields values for where the $1/e^2$ beam profile crosses the interface. This can only be done if the assumption is made that the beam profile at the interface is Gaussian. The intensity profile, I, of the beam across the interface can then be given for any angle of θ_{inc} using the expression (5.6) which has been derived from (5.3) [Siegman] as follows:

$$I = I_0 \exp\left(-\frac{2z^2}{l^2}\right) \quad \textbf{(5.3)}$$

therefore

$$P_{total} = \int_{-\infty}^{\infty} I dz = I_0 \int_{-\infty}^{\infty} \exp\left(\frac{-2z^2}{l^2}\right) dz \quad \textbf{(5.4)}$$

where P_{total} is the total input power of the incident beam, l is the $1/e^2$ width of the Gaussian intensity profile projected along the interface and z is the distance along the device where z = 0 corresponds to the position of the beam waist.

The standard integral $\int_{-\infty}^{\infty} e^{-ax^2} dx = \sqrt{\frac{\pi}{a}}$ where a>0, which is true in our case because $a = \frac{2}{l^2}$, is then used and (5.4) becomes:

$$P_{total} = I_0 \sqrt{\frac{\pi l^2}{2}} = I_0 l \sqrt{\frac{\pi}{2}} \quad \textbf{(5.5)}$$

re-arranging (5.5) in terms of I_0 and substituting this into (5.3) becomes:

$$I = \frac{P_{total}}{l} \sqrt{\frac{2}{\pi}} \exp\left(-\frac{2z^2}{l^2}\right) \quad \textbf{(5.6)}$$

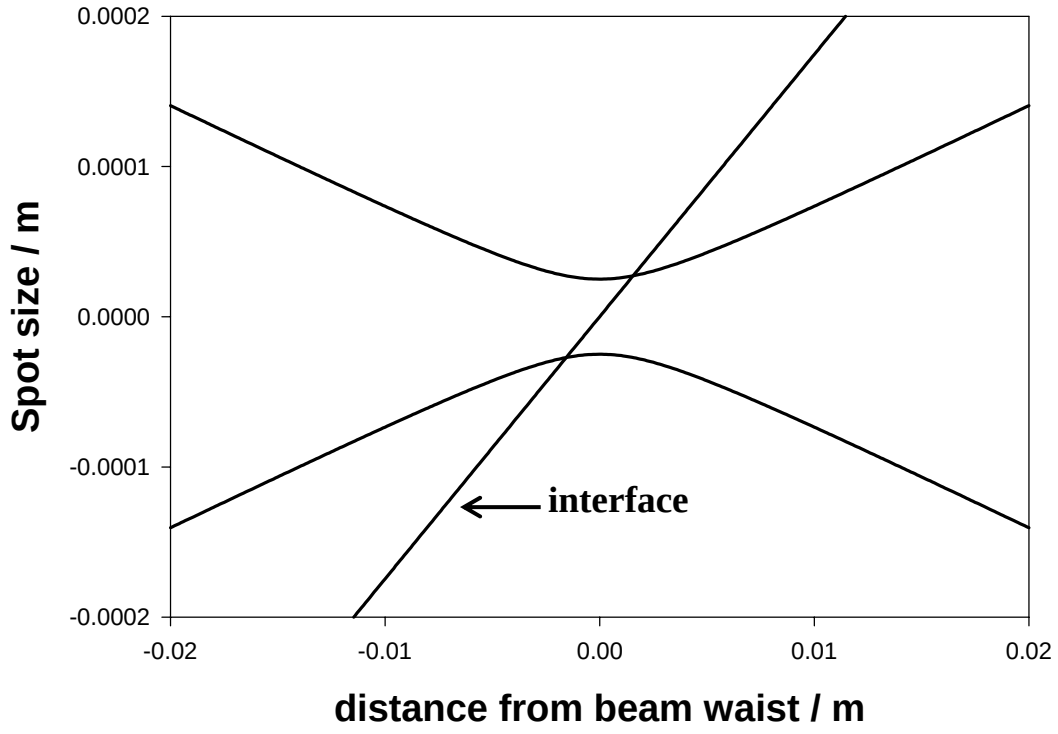

Figure 5.6. Beam profile observed at the domain boundary for 0.543 μm light with a spot size of 25 μm incident at an angle of 89°.

The power in each slice, i.e. between points z_1 and z_2 is then found by using the *error function (erf)* as described below where $erf(x) = \frac{2}{\sqrt{\pi}}\int_0^x e^{-t^2}dt = \frac{1}{\sqrt{\pi}}\int_{-x}^{x} e^{-t^2}dt$ i.e. it is a symmetric function.

In this model, $t^2 = \frac{2z^2}{l^2}$, therefore $dt = \frac{\sqrt{2}}{l}dz$.

At $t=0$, $z = \frac{lt}{\sqrt{2}}$ therefore $z = 0$.

At $t = x$, $z = \frac{lx}{\sqrt{2}}$ and then re-arranging $x = \frac{\sqrt{2}z}{l}$

Therefore:

$$erf\left(\frac{\sqrt{2}z_1}{l}\right)=\frac{2}{\pi}\frac{1}{l}\int_{-z_1}^{z_1}e^{\frac{\sqrt{2}z^2}{l^2}}dz \qquad \textbf{(5.7)}$$

which gives

$$\int_{-z_1}^{z_1}e^{-\frac{2z^2}{l^2}}dz=l\sqrt{\frac{\pi}{2}}erf\left(\frac{\sqrt{2}z_1}{l}\right) \qquad \textbf{(5.8)}$$

which is the area under a curve between $-z_1$ and z_1, see fig.5.7 below.

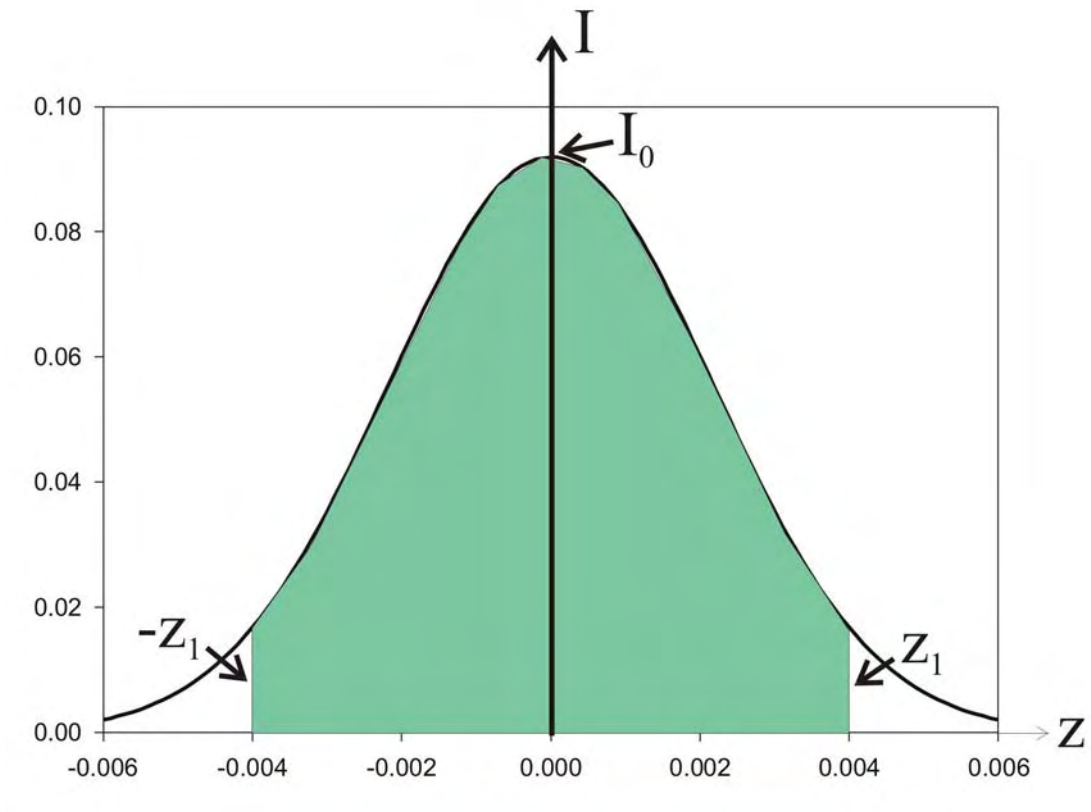

Figure 5.7. Area under curve between points $-z_1$ and z_1

So the power under the curve, $P_{z_1}=\int_{-z_1}^{z_1}Idz=\frac{P_{total}}{l}\sqrt{\frac{2}{\pi}}\int_{-z_1}^{z_1}\exp\left(\frac{-2z^2}{l^2}\right)$

Using (5.8) P_{z_1} becomes:

$$P_{z_1}=\frac{P_{total}}{l}\sqrt{\frac{2}{\pi}}l\sqrt{\frac{\pi}{2}}erf\left(\frac{\sqrt{2}z_1}{l}\right)=P_{total}erf\left(\frac{\sqrt{2}z_1}{l}\right) \qquad \textbf{(5.9)}$$

To find the power in a slice as shown in fig. 5.5, the expression $P_{slice} = \frac{P_{z_1} - P_{z_2}}{2}$ is used. In this case it becomes:

$$P_{slice} = \frac{p_{total}}{2}\left(erf\left(\sqrt{\frac{2z_1}{l}}\right) - erf\left(\sqrt{\frac{2z_2}{l}}\right)\right) \qquad \textbf{(5.10)}$$

where z_1 and z_2 are the two points that define the slice width.

As the beam is focussed into the sample there is a variation in the angle of incidence across the beam width, as shown in fig. 5.8 below.

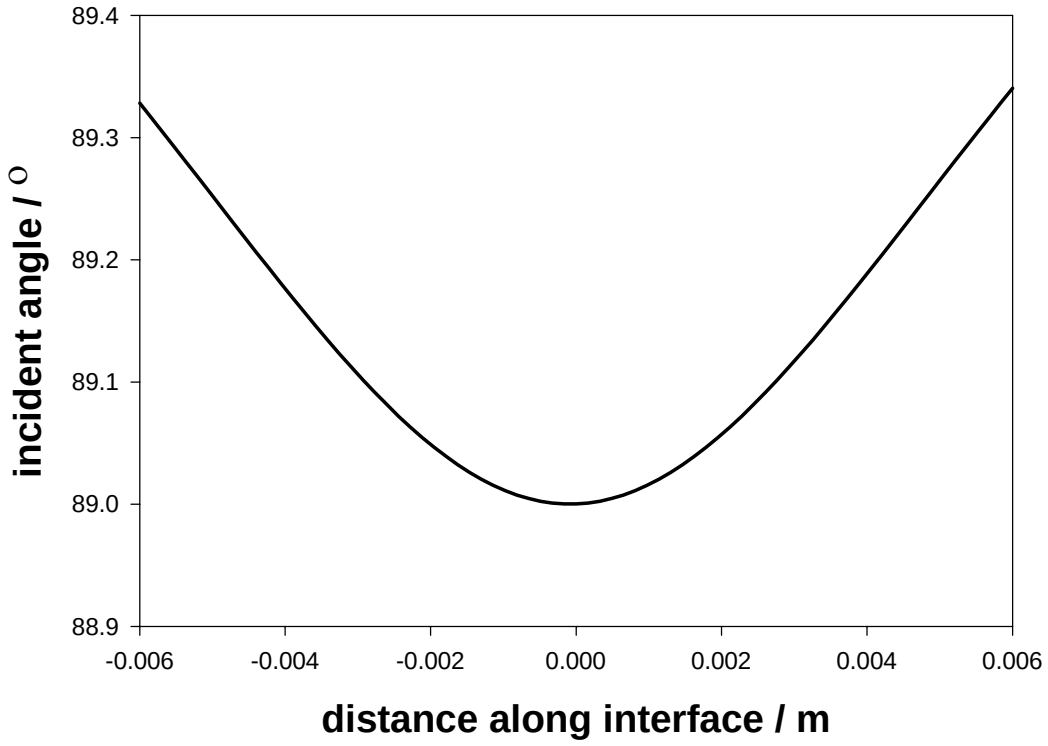

Figure 5.8. Variation of incident beam angle across the boundary for 1.52 μm light with a spot size of 64 μm incident at an angle of 89°.

Due to this variation across the beam each slice has a different effective angle of incidence, and knowing this the reflectivities of each slice can be calculated by

modifying the standard Fresnel equation (5.11) as applicable to fig.5.9 [Hecht] to be in terms of θ_{inc} (5.17). Eqn (5.17) is derived from (5.11) as shown below:

$$r_s = \frac{n_i \cos\theta_{inc} - n_t \cos\theta_t}{n_i \cos\theta_{inc} + n_t \cos\theta_t} \qquad \textbf{(5.11)}$$

where r_s is the amplitude reflection coefficient associated with *s*-polarised light.

This is not the most convenient form of the expression, but it can be re-cast in terms of θ_{inc} and n_{it}, where $n_{it} = n_{inc}/n_t$.

$$r_s = -\frac{\sin(\theta_{inc} - \theta_t)}{\sin(\theta_{inc} + \theta_t)} \qquad \textbf{(5.12)}$$

this can be expanded to become:

$$r_s = -\frac{[\sin\theta_{inc}\cos\theta_t - \cos\theta_{inc}\sin\theta_t]}{[\sin\theta_{inc}\cos\theta_t + \cos\theta_{inc}\sin\theta_t]} \qquad \textbf{(5.13)}$$

using: $n_t \sin\theta_t = n_{inc}\sin\theta_{inc}$

therefore : $\sin\theta_t = n_{it}\sin\theta_{inc}$

Eqn. (5.13) then becomes:

$$r_s = -\frac{[\sin\theta_{inc}\cos\theta_t - \cos\theta_{inc} n_{it}\sin\theta_{inc}]}{[\sin\theta_{inc}\cos\theta_t + \cos\theta_{inc} n_{it}\sin\theta_{inc}]} \qquad \textbf{(5.14)}$$

cancel $\sin\theta_{inc}$ throughout

$$r_s = -\frac{[\cos\theta_t - \cos\theta_{inc} n_{it}]}{[\cos\theta_t + \cos\theta_{inc} n_{it}]} \qquad \textbf{(5.15)}$$

then re-cast $\cos\theta_t$ using : $\cos\theta_t = \cos\left(\sin^{-1}[n_{it}\sin\theta_{inc}]\right)$

Eqn. (5.15) becomes:

$$r_s = -\frac{\left[\cos\left(\sin^{-1}[n_{it}\sin\theta_{inc} - \cos\theta_{inc} n_{it}]\right)\right]}{\left[\cos\left(\sin^{-1}[n_{it}\sin\theta_{inc} + \cos\theta_{inc} n_{it}]\right)\right]} \qquad \textbf{(5.16)}$$

But as $R_s = r_s^2$ where R_s is the reflectance associated with s-polarised light.

$$R_s = \left(\frac{\left[\cos\left(\sin^{-1}\left[n_{it} \sin\theta_{inc} - \cos\theta_{inc} n_{it} \right] \right) \right]}{\left[\cos\left(\sin^{-1}\left[n_{it} \sin\theta_{inc} + \cos\theta_{inc} n_{it} \right] \right) \right]} \right)^2 \quad \textbf{(5.17)}$$

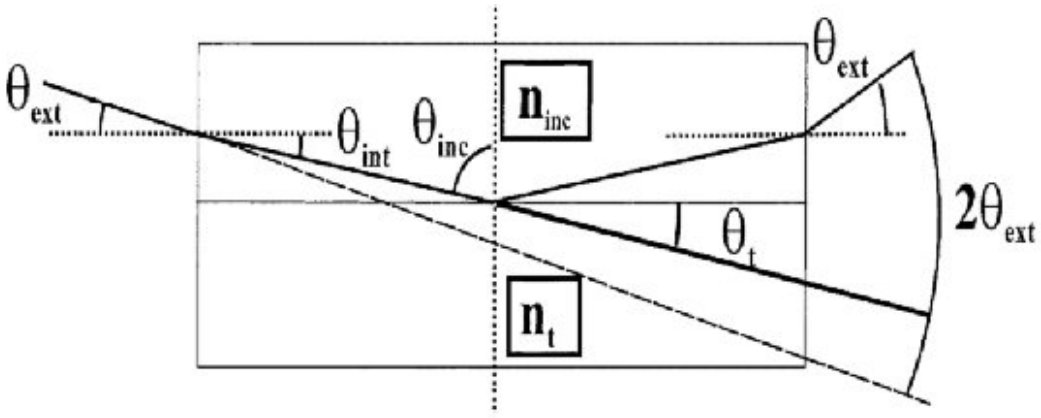

Fig. 5.9 Schematic for Fresnel reflection and geometry of interaction at interface.

The power reflected for each slice is then calculated by multiplying the reflectivity for each slice by the power in each slice. The sum of the power of the slices that have reflectivities that fall within the parameters necessary for TIR is then calculated. This procedure is evaluated for 1000 points between 0 and 1000V. The percentage of the total power is then plotted against voltage, and this allows a comparison to be made with the experimental data collected.

5.5 Results

Fig. 5.9 also shows the geometry of interaction for the beam with the interface for all the results that follow. The $2\theta_{ext}$ angle is determined before measuring any power reflectivities and θ_{inc} is given by the expression:

$$\theta_{inc} = 90 - \theta_{\text{int}} = 90 - \left(\sin^{-1}\left(\frac{\sin\theta_{ext}}{n_e} \right) \right) \quad \textbf{(5.18)}$$

Initially results were taken using the 0.543μm laser to characterise the presence and the strength of any residual refractive index difference at the interface. Powers in the

reflected beam were measured at various angles with no voltage applied. The data was then superimposed onto the standard Fresnel reflectivity curves and visually best fitted to obtain values for Δn in the interface region. An example residual reflection at the interface for incident light of *p*-polarisation, at 0.543μm can be seen below in fig. 5.10.

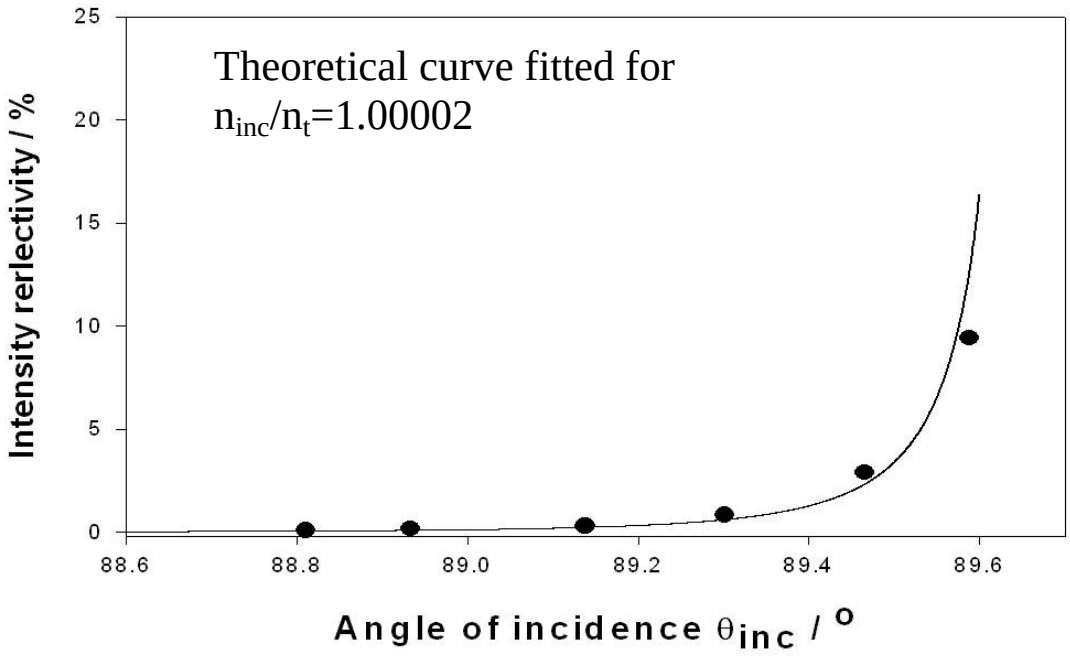

Figure 5.10. Residual reflection at interface for incident light of p-polarisation, λ=0.543μm from a He-Ne laser

The values of residual refractive index for both polarisations as calculated by such visual best fits on each side of the interface can be seen in table 5.2. Where the '+' and '-' signs correspond to whether the best fit Fresnel reflectivity curve is for a value of Δn greater than or less than 1 respectively.

	'+' side	**'-' side**
***s*-polarisation**	1.000046	0.999890
***p*-polarisation**	1.000020	0.999985

Table 5.2. Best-fitted residual refractive index on either side of the domain boundary

Switching data was recorded using the 0.543μm He-Ne laser for both *s*- and *p*-polarised light, and these results are shown in fig 5.11. As expected when considering the values of the respective electro-optic coefficients accessed by each polarisation orientation, the switching for s-polarised light occurs much before that of the p-polarised light. The contrast ratio achieved was observed to be greater than 100:1 (20dB), as shown in fig 5.12.

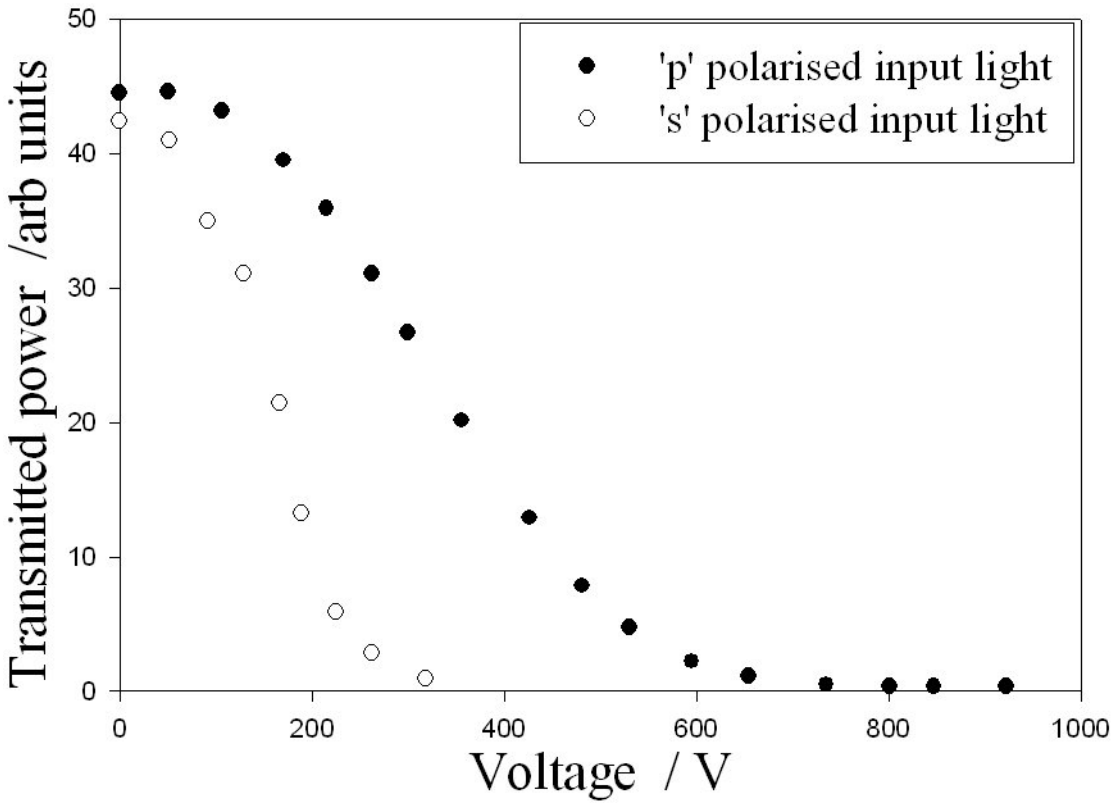

Figure 5.11. Comparison of s-and p-polarised light λ=0.543μm from a He-Ne laser

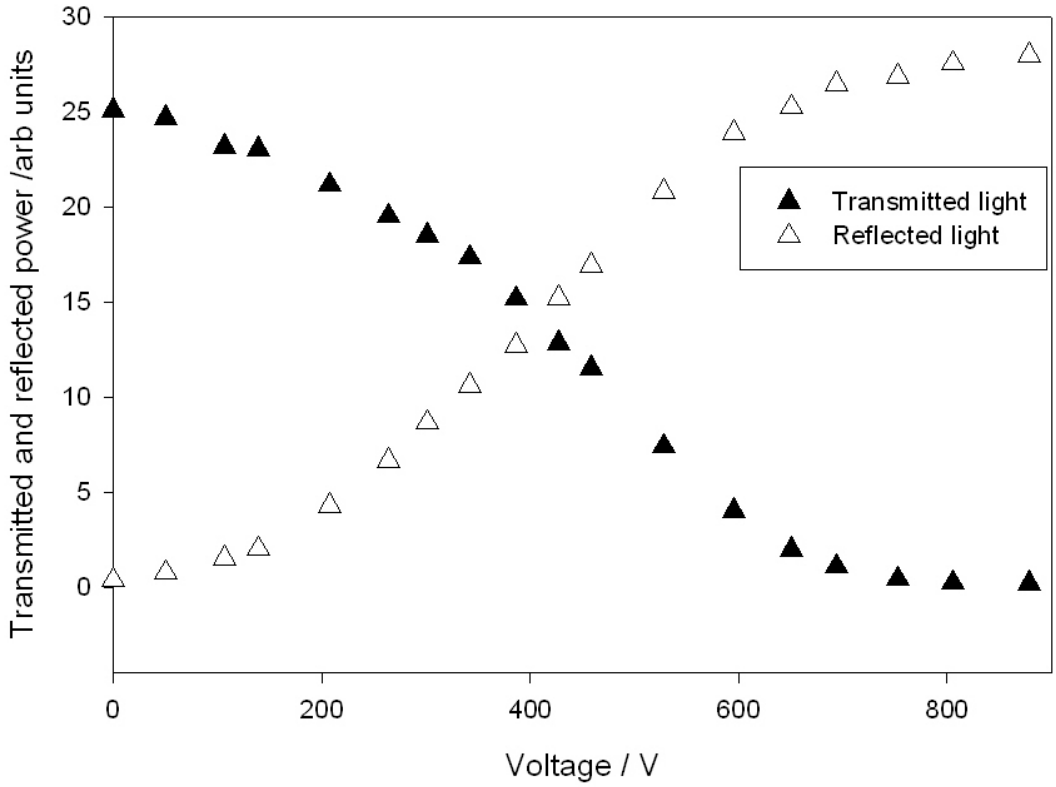

Figure 5.12. Transmitted and reflected beam powers as a function of applied voltage

Switching data was also recorded at the longer He-Ne wavelength of 1.52μm where good switching characteristics where again observed. However for this wavelength the contrast ratios achieved were significantly greater than 100:1 but the measurement of exact values was limited by the resolution of the apparatus used for measurement.

Detailed comparison between the theoretical curves generated by the model, and experimental data points was then possible. Fig. 5.13 shows that good agreement can be obtained for the early stages of switching at low applied voltages. The lack of fit as TIR is approached can be accounted for by introducing a small random angle varying between 0^o and 0.2^o across the interface in the numerical model to closer match the actual randomness observed for the interface. This randomness can give a closer

match to the experimental results obtained; an example of this can be seen in the inset of fig 5.13.

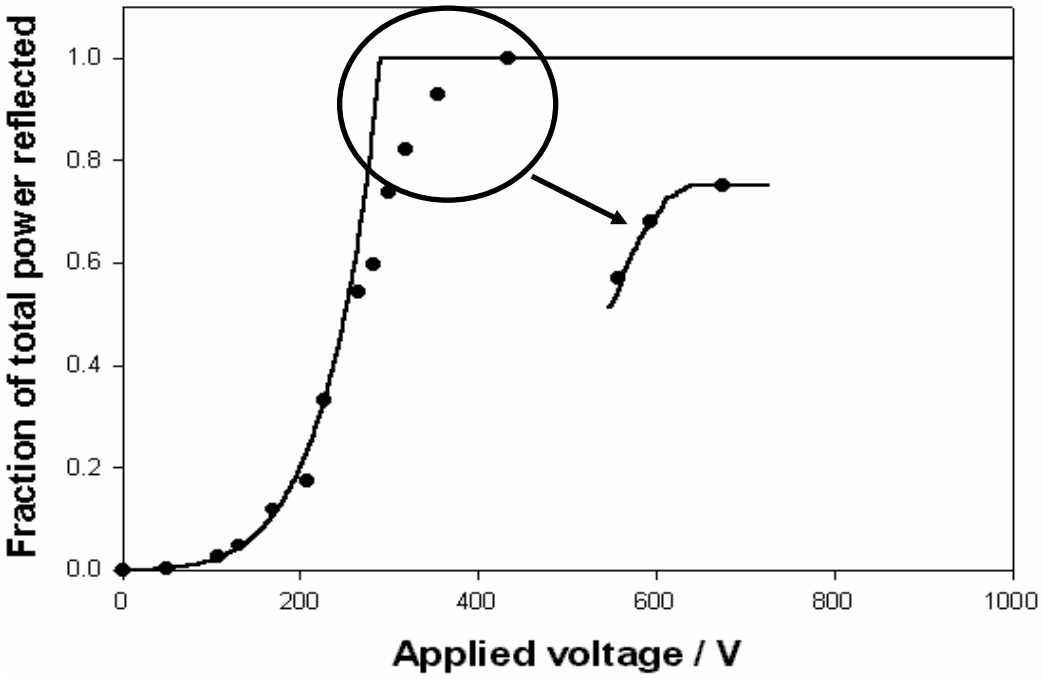

Figure 5.13. Comparison of model and switching data for s-polarised light at 1.52μm incident at an angle of 89.1° (points are experimental measurements, solid line is theoretical fit).

5.6 Comparison with Pockels cell

The switch is much less wavelength dependent than other electro-optic switches such as a Pockels cell, and a comparison of voltages required for TIR for the switch and the half wave voltage, V_π, for a Pockels cell confirms this. V_π for the devices with crystal orientations as illustrated in fig. 5.14 are have been derived.

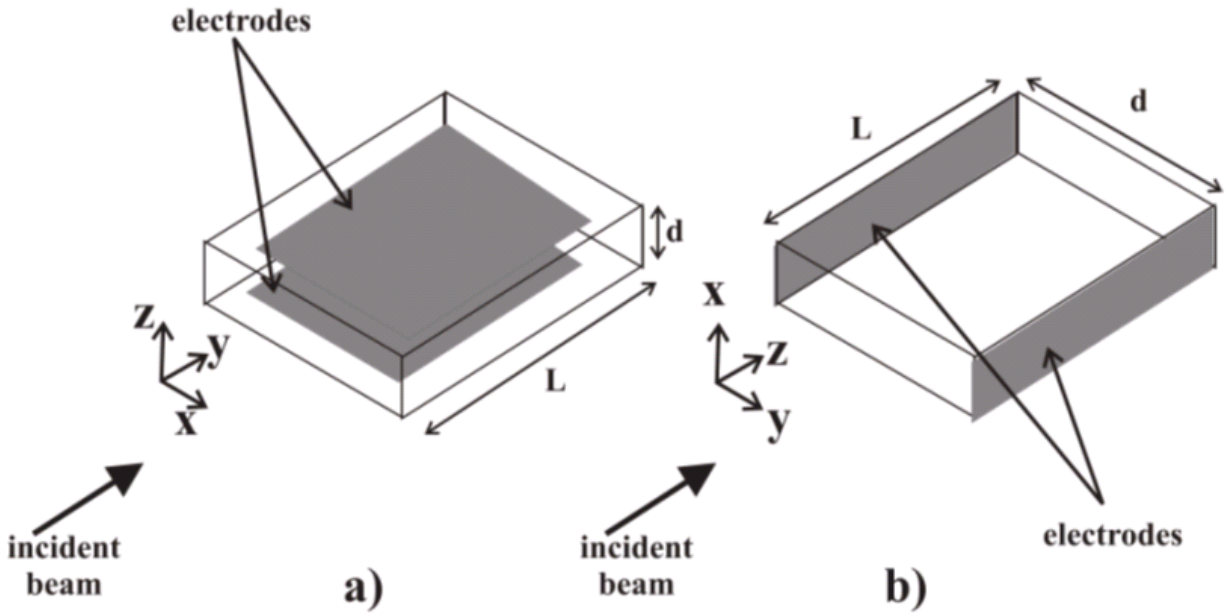

Fig. 5.14. Crystal orientations for Pockels cells in LN

Light polarised at 45^{o} to the *x*- and *z*- axis propagating along the *y*-axis as shown in fig. 5.14a will observe a change in the n_o and n_e when a field is applied across the *z*-axis. The change in refractive index is expressed by:

$$\Delta n_o = -\frac{1}{2} n_o^3 r_{13} E_z \qquad \textbf{(5.19a)}$$

and

$$\Delta n_e = -\frac{1}{2} n_e^3 r_{33} E_z \qquad \textbf{(5.19b)}$$

The relative phase change of the *o*- and *e*- waves after travelling distance L in the crystal, known as the retardation, Γ is expressed as

$$\Delta\Gamma = \Gamma_o - \Gamma_e = \frac{2\pi L}{\lambda}(n_o + \Delta n_o - n_e - \Delta n_e) \qquad \textbf{(5.20)}$$

while their amplitudes are equal. The intensities of the light emerging from the crystal polarised parallel and perpendicularly to the incident polarisation are

$$I^{\square} = I_0 \cos^2\left(\frac{\Delta\Gamma}{2}\right) = \frac{1}{2} I_0 (1 + \cos\Delta\Gamma) \qquad \textbf{(5.21)}$$

and

$$I^{\perp} = I_0 \sin^2\left(\frac{\Delta\Gamma}{2}\right) = \frac{1}{2} I_0 (1 - \cos\Delta\Gamma) \qquad \textbf{(5.22)}$$

where I_0 is the incident intensity.

Thus if the zero field retardation $\frac{2\pi L(n_o - n_e)}{\lambda}$ is an even multiple of π, then $I^{\perp} = 0$

in the absence of an applied field and for $E \neq 0$

$$I^{\perp} = I_0 \sin^2\left\{\frac{\pi L}{2\lambda}(n_e^3 r_{33} - n_o^3 r_{13}) E_z\right\} \qquad \textbf{(5.23)}$$

The voltage required to increase I from 0 to 1 is V_{π} and is expressed as [Lines]

$$V_{\pi} = \frac{\lambda}{n_e^3 r_{33} - n_o^3 r_{13}} \frac{d}{L} \qquad \textbf{(5.24)}$$

An alternative geometry suitable for a Pockels cell also exists in LN as shown in fig. 5.14b. In this geometry light polarised at 45^{o} to the *x*- and *y*- axis propagates along the *z*-axis, while the field is applied across the *y*-axis. When the field is applied the change in refractive index can be expressed as

$$\Delta n_o = -\frac{1}{2} n_o^3 r_{22} E_y \qquad \textbf{(5.25)}$$

because this orientation is optically isotropic in the absence on an applied field.

The retardation for this case can be expressed as

$$\Delta\Gamma = \frac{\pi L}{\lambda} n_o^3 r_{22} E_y \qquad \textbf{(5.26)}$$

Therefore the V_{π} is expressed as [Lines]

$$V_{\pi} = \frac{\lambda}{2r_{22}n_o^3}\frac{d}{L} \qquad \textbf{(5.27)}$$

For the TIR switch, substituting for $E_z = V/d$ where V is the voltage applied across the interface and d is the switch thickness and rearranging eqn. (5.2) the voltage required for TIR switching can be given by the expression:

$$V = \frac{2\Delta nd}{r_{33}n_e^3} = \frac{\Delta n * d}{r_{33}n_e^3} \qquad \textbf{(5.28)}$$

It is clear from eqn's 5.24 and 5.27 that the value of V_{π} is directly proportional to λ, in contrast to the TIR switch where λ does not appear. Table 5.3 shows comparisons of the switching voltages required for both orientations of crystal for the Pockels cell and for two angles of incidence on the TIR switch at wavelengths of 0.633μm, 1.064μm and 3.39μm. As terms relating to the electro-optic coefficients and refractive indices and their intrinsic wavelength dispersion are common to all eqns 5.24, 5.27 and 5.28 this leads to the approximation that the TIR switch operation is effectively wavelength independent.

wavelength	**TIR switch** **89.1° / 89.5°**	**Pockels cell a**	**Pockels cell b**
633nm	225V / 69V	89V	116V
1064nm	240V / 74V	158V	211V
3390nm	266V / 82V	554V	757V

Table 5.3. Comparison of voltages required for TIR switch and Pockels cell

Figure 5.15 shows a comparison of the voltages required for TIR for the wavelengths 633nm, 1064nm and 3390nm.

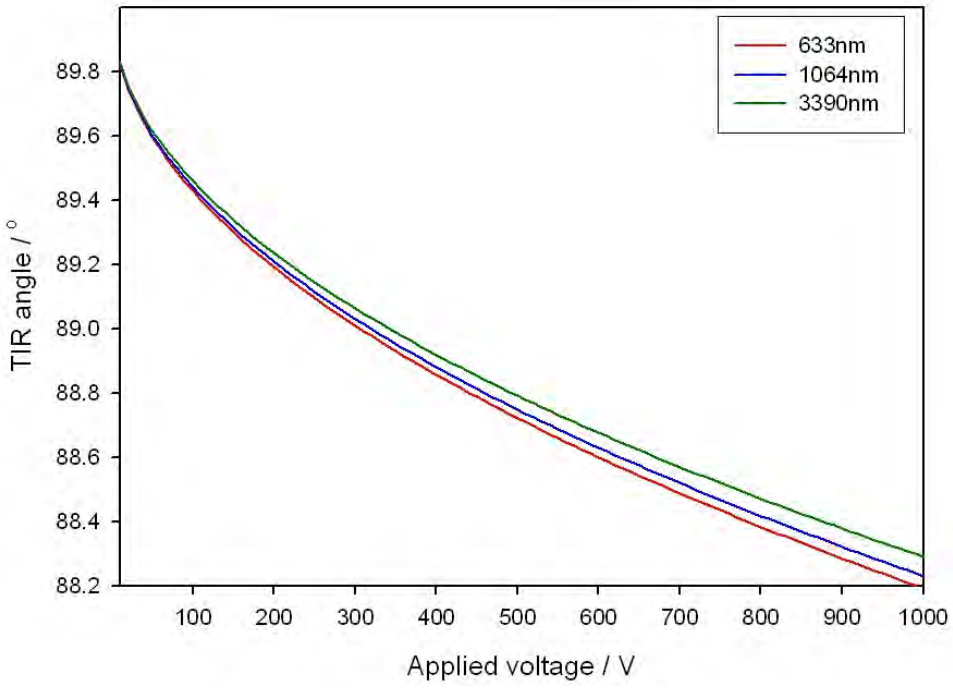

Fig. 5.15. TIR angle against voltage comparison with wavelength, for a 300 μm thick device

Figure 5.16 shows a comparison of the operating voltages for the devices described in this section as a function of wavelength.

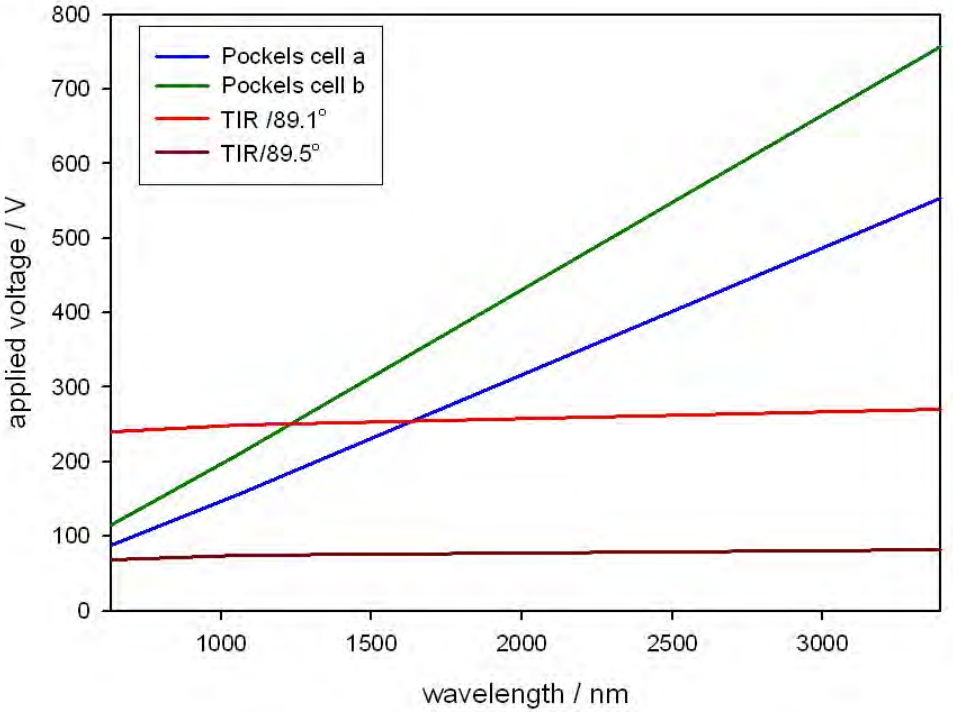

Fig. 5.16. Comparison of device switching voltage against wavelength with all devices having the same dimensions

5.7 Summary

A novel electo-optic switching technique has been described. It has shown good contrast ratios of greater than 100:1 (20dB) and by optimising the manufacturing method the contrast ratio could be increased significantly and fulfil the potential associated with TIR (TIR is a 100% efficient process). The switch has been shown to function well at wavelengths of 0.543μm and the useful telecoms wavelength of 1.52μm. It has also been shown that the switching behaviour fits well to curves as predicted by a theoretical model.

5.8 References

[Boyland01a] Boyland, A. J., Ross, G. W., Mailis, S., Smith, P. G. R. and Eason, R. W. (2001b) *Electronics Letters,* **37**, 585-587.

[Boyland01b] Boyland, A. J., Mailis, S., Hendricks, J. M., Smith, P. G. R. and Eason, R. W. (2001a) *Optics Communications,* **197**, 193-200.

[Barrington03] Barrington, S.J., Boyland, A.J., and Eason, R.W. *Submitted Applied Optics 2003*

[Eason01] Eason, R. W., Boyland, A. J., Mailis, S. and Smith, P. G. R. (2001) *Optics Communications,* **197,** 201-207.

[Gahagan99] Gahagan, K. T., Gopalan, V., Robinson, J. M., Jia, Q. Z. X., Mitchell, T. E., Kawas, M. J., Schlesinger, T. E. and Stancil, D. D. (1999) *Applied Optics*, **38,** 1186-1190.

[Hecht] Hecht, E. (1998) *Optics,* Addison-Wesley, Reading, MA.

[Li96] Li, J., Cheng, H. C., Kawas, M. J., Lambeth, D. N., Schlesinger, T. E. and Stancil, D. D. (1996) *IEEE Photonics Technology Letters,* **8**, 1486-1488.

[Lines] Lines, M. E., and Glass, A.M. (1977) *Principles and Applications of Ferroelectric and Related Materials,* Clarendon Press, Oxford.

[Lovett] Lovett, D. R. (1999) *Tensor Properties of Crystals,* Institute of Physics Publishing, Bristol, UK.

[Siegman] Siegman, A. E. (1986) *Lasers,* University Science Books, Sausalito.

[Weis85] Weis, R. S. and Gaylord, T. K. (1985) *Applied Physics A-Materials Science & Processing,* **37,** 191-203.

[Yamada96] Yamada, M., Saitoh, M. and Ooki, H. (1996) *Applied Physics Letters,* **69,** 3659-3661.

Chapter 6

Electro-optically controlled beam deflector

6.1 Overview

In addition to the switching technique [Boyland01a, Boyland01b] discussed in chapter 5 a similar technique can be used to induce an electro-optically controllable beam deflection for light that is incident on the interface between the two anti-parallel domains[Eason01, Barrington03].

Due to the requirements of speed, compactness and integration the use of domain-engineered ferroelectrics such as lithium niobate and lithium tantalate that permit electro-optic control of the local refractive index, thereby enabling small changes in propagation direction via refraction at an interface, mean that they are the materials of choice. The use of these materials for this application has mostly been reported for prism type geometries in which light is incident on a series of triangular domain-inverted regions, where the deflection angles achievable are a function of both geometry and number of prisms [Chen94, Li96]. Further levels of integration have also been reported, in which scanning has been integrated with focussing elements [Gahagan99], second harmonic generation [Chiu99a], and for use as a laser Q-switch [Abedin95].

Although recent work has addressed the problem of optimising the design of such electro-optic prism scanners, and also discussed the gradient index deflectors, where

the light ray is bent as it propagates through a region of non-uniform refractive index [Chiu99b], there remains a fundamental problem with this method. The linear electro-optic effect in LN and LT is comparatively weak, and at moderate field strengths of ~1kVmm^{-1}, the deflection angles achievable are small. This can be shown using the calculation for deflection angle, δ, achievable for a single e-o prism deflector under four different electric field addressing geometries.

The expression relating the induced refractive index change, Δn, under electro-optic addressing, as a function of electric field strength, E_z, is given by eqn. (5.2). For simplicity, and as a means of comparison between existing electro-optic prism and the near TIR geometry designs, a common set of values for refractive index, electro-optic coefficient, and value of applied field are used. These values are: n_e = 2.23, r_{33} = 30.8 x 10^{-12}mV^{-1} [Weis85], and E_z = 1 kVmm^{-1} (10^6 Vm^{-1}), which relate to single crystal LN for light in the mid-visible spectral region at ~550nm.

Fig. 6.1 shows the geometry for beam deflection via a prism of apex angle, α. There are four possible conditions of electro-optic addressing that can produce beam deflections when an electric field is applied to either the prism and/or the background host material. The value of the deflection can be doubled by simultaneously increasing one refractive index (e.g. n_2), while reducing the other (n_1) by the same amount, as is the case for a uniform field applied to a domain inverted sample.

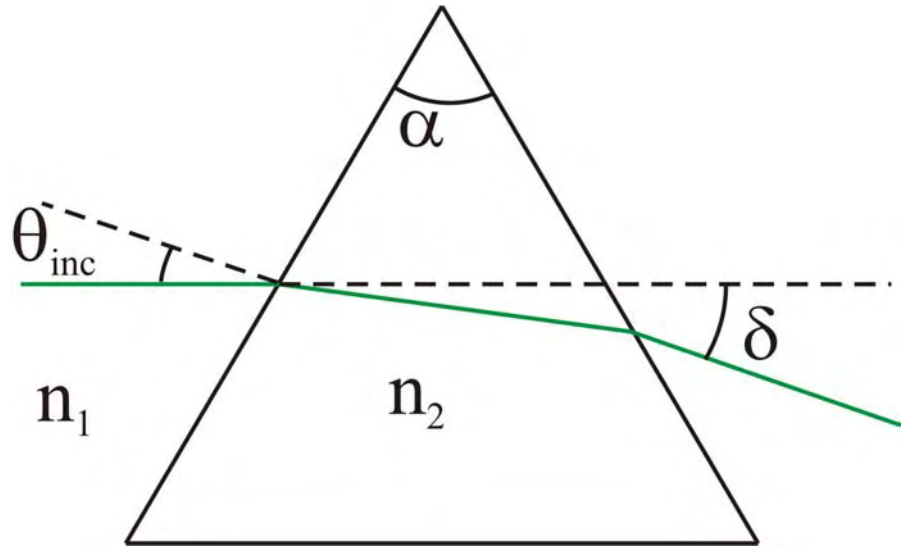

Figure 6.1. Schematic of refraction through a prism of refractive index n_2 in a host medium index of n_1. Overall angular deflection is δ.

Additionally, as has been demonstrated in [Gahagan99] for example, prisms can be cascaded so that the deflection angles are increased as a linear function of the number of prisms. As the beam emerges into air from the LN there is a final magnification of the deflection due to Snell's law operating at the exit interface.

Table 6.1 shows the calculated values of beam deflection angle for these four different geometries, for a common angle of incidence of 30°, with an applied field of 1 kV mm^{-1}. It is interesting to observe the small values obtained for δ, which have been calculated for a single prism of apex angle 60°, for the four possible values of n_2 / n_1, which has been abbreviated to n_{21}. Even for the most favourable case where $n_1 = n - \Delta n$, and $n_2 = n + \Delta n$, the deflection angle is only 0.01°. In [Gahagan99] it refers to the case where seven prisms are used in series, and the applied field was ~4.4kVmm^{-1} producing a total deflection angle of ~0.3°, which is magnified to ~0.66° due to refraction when the beam exits to air. In [Gahagan99] where α was of order 66°, the reported beam deflection was 0.72° (12.65mrad).

n_1	n_2	n_{21}	$\delta/^o$
n-Δn	n+Δn	1.000153	0.010
n	n+Δn	1.000077	0.005
n+Δn	n-Δn	0.999849	-0.010
n	n-Δn	0.999923	-0.005

Table 6.1. Four combinations of indices n_1 and n_2 for electro-optic addressing of prism and/or host material, and resultant values of n_{21} and associated value of δ.

Fig. 6.2 shows calculations of deflection angle δ for the four possible electro-optic geometries, using the following equation for beam deflection via a prism of apex angle α [Hecht]:

$$\delta = \theta_{inc} - \alpha + \sin^{-1}\left(\sin\alpha \left[(n_{21})^2 - \sin^2\theta_{inc} \right]^{\frac{1}{2}} - \sin\theta_{inc}\cos\alpha \right) \qquad \textbf{(6.1)}$$

where θ_{inc} is the angle of incidence. As expected the plots are symmetrical about the zero deflection line, but what is immediately apparent is that the ~30^o angles typically used for θ_{inc} in prism scanners represents the angle for which minimum deviation is produced. This choice of angle is necessary however when cascaded prisms are used as in [Gahagan99], and in-line prisms are the preferred design.

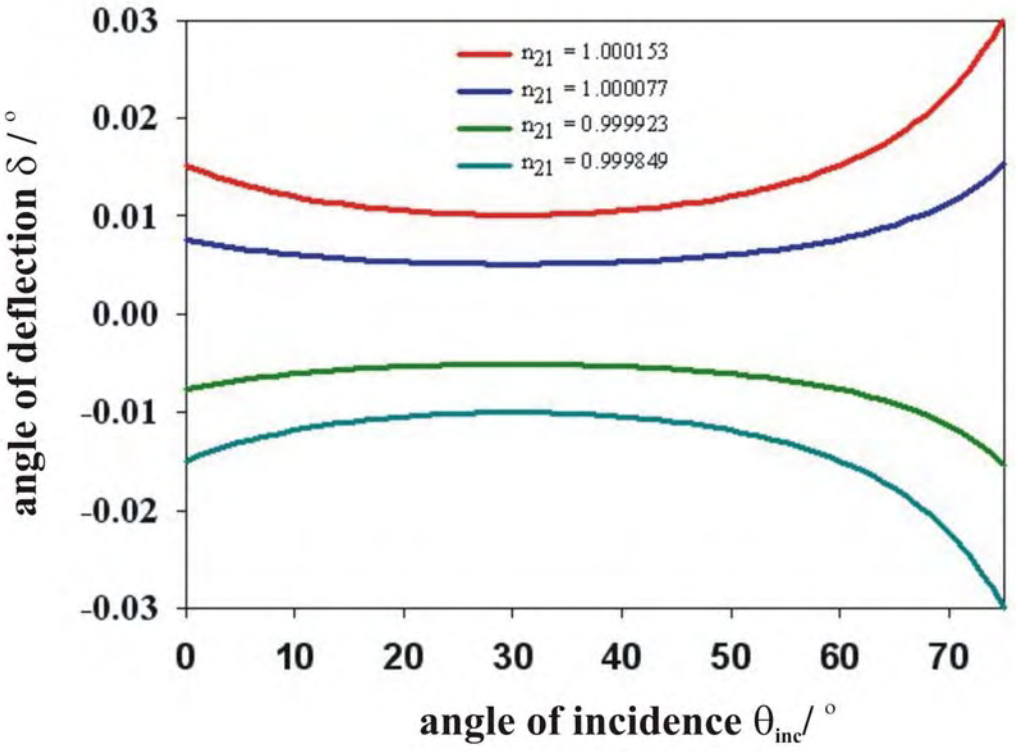

Fig. 6.2. Angle of deflection δ as a function of angle of incidence θ_{inc} for n_{21} values as shown in table 6.1

It is therefore apparent that the single prism deflection result of ~0.01° for a normalised value of applied field of 1kVmm^{-1} may be increased if alternative geometries are used. In this chapter the use of a near TIR geometry will be discussed.

6.2 Experimental procedure

The device used for these experiments is the same as that used in chapter 5 for the TIR switch. The device schematic is the same as that seen in fig. 5.3, but can be seen again here in fig. 6.3a and a plan view of the scanner can be seen in fig. 6.3b.

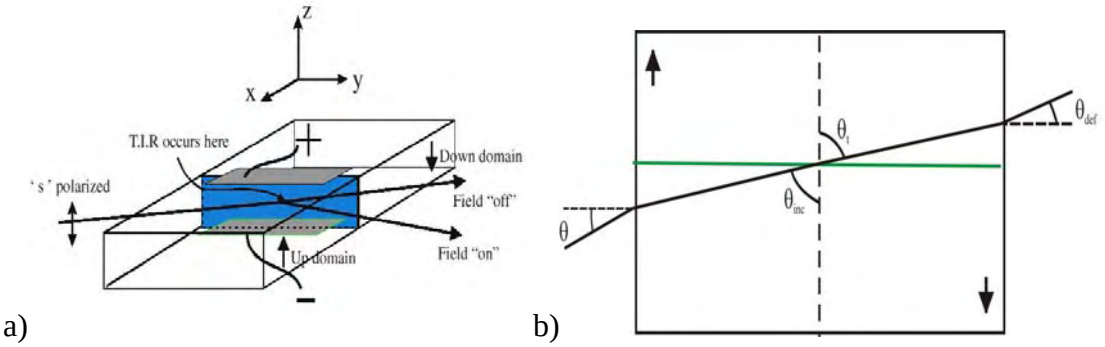

a) b)

Fig. 6.3. a) device schematic b) Plan view of scanner.

The characterisation of the device was again performed using the two polarised He-Ne laser wavelengths of 0.543μm and 1.52μm. Focussing was again achieved using a lens of focal length 160mm, which produced a spot size of 25μm at the midpoint along the interface for the 0.543μm light.

6.3 Theoretical model

The modelling of the deflection angles expected for the refracted ray can be achieved by applying Snell's law to the interface as shown in the expression below:

$$(n+\Delta n)\sin\theta_{inc} = (n-\Delta n)\sin\theta_t \qquad \textbf{(6.2)}$$

Figure 6.4 shows the values of θ_t calculated using (6.2), as a function of the voltage applied across the interface for values of θ_i ranging from 87.7^o to 89.0^o. It is immediately apparent that even for modest voltages of order a few hundred volts, substantial deflections of ~1^o can be obtained.

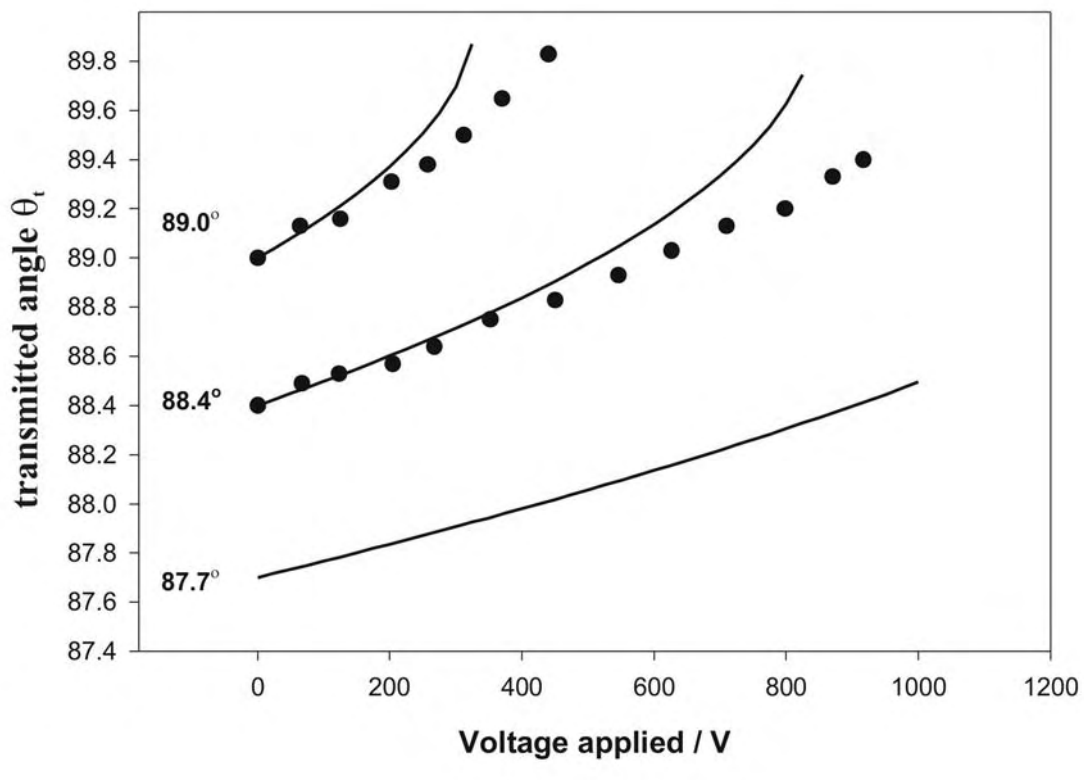

Figure 6.4. Calculated transmitted angles θ_t as a function of applied voltage, for three values of θ_{inc} from 87.7° to 89.0°, a comparison is made with experimental results obtained for θ_{inc} = 88.4° and 89.0°, using light from a 1.52μm He-Ne laser.

For the case of θ_{inc} = 87.7° it can be seen that the relationship is effectively linear for this voltage range. For the case of θ_{inc} = 88.4°, a value we have investigated experimentally and which is relatively easy to implement in a sample with an interface length ~10mm, a voltage of 300V (corresponding to the normalised value of 1kVmm^{-1} across the 300μm thick sample) produces an angular deflection of 0.39°. When compared to the value of angular deflection for the single prism deflector evaluated earlier it is clear to see that this near TIR geometry is ~40 times higher in sensitivity.

The transmitted intensity across the interface is also an important factor that needs to be considered when characterising the device. As the deflection angle increases, and TIR is approached, the transmitted intensity across the interface decreases. This transmitted intensity is calculated using the expression [Hecht]:

$$T_s = \left(\frac{n_t \cos\theta_t}{n_i \cos\theta_i} \right) t_s^2 \qquad \textbf{(6.3)}$$

where T_s is the transmittance (intensity transmission) associated with s-polarised light, and t_s is the amplitude transmission coefficient associated with s-polarised light , $t_s = \frac{2n_{inc}\cos\theta_{inc}}{n_{inc}\cos\theta_{inc} + n_t \cos\theta_t}$.

The transmitted intensity calculated for the same range of applied field as in fig. 6.4 is shown in fig. 6.5. While it is clear that for values of $\theta_i > 89^o$ the transmission falls rapidly as a function of applied voltage, for a value of $\theta_i < 88^o$ the slope is small, and some degree of linearity exists between transmission and applied field.

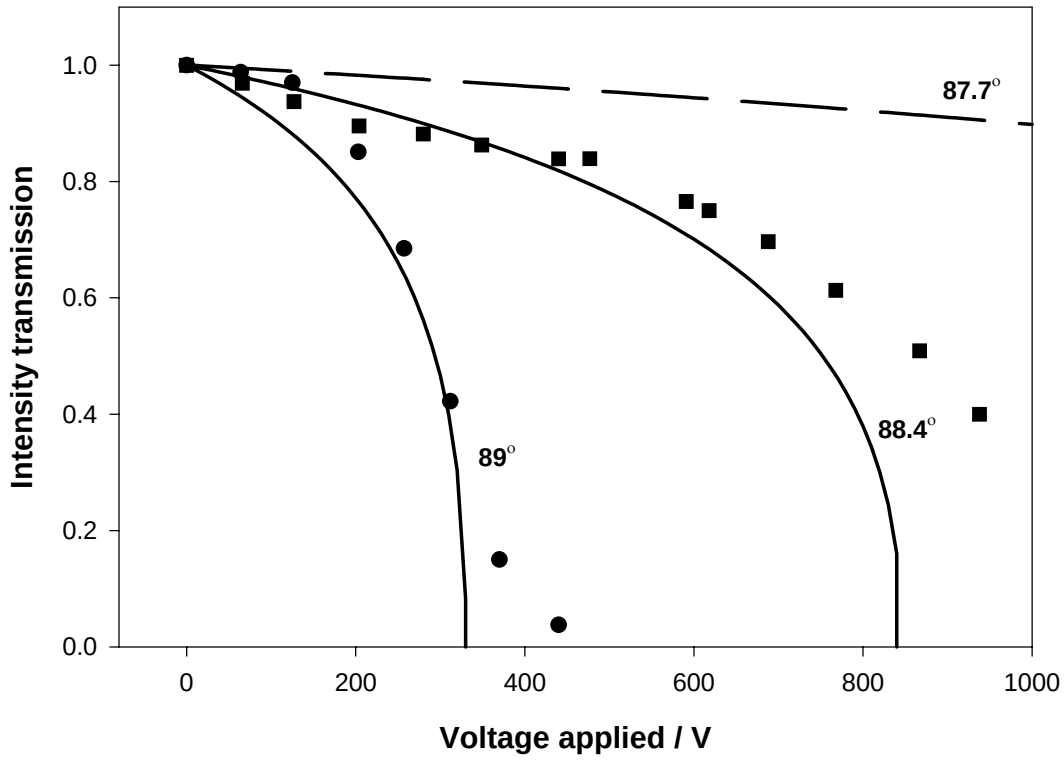

Fig. 6.5. Intensity transmission across the interface as a function of voltage applied, for a range of values of θ_{inc} from 87.7° to 89.0°. A comparison is made with experimental results obtained for θ_{inc} = 88.4° and 89.0°, using light from a 1.52μm He-Ne laser.

6.4 Results

A comparison between the theoretical model shown as solid lines and experimental results represented by dots obtained using *s*-polarised light from the 1.52μm He-Ne laser can be seen in figs 6.4 and 6.5. It can be seen that the overall shape is very similar to the experimental results. These errors occur due to both the uncertainty of the absolute value of θ_i which is difficult to measure precisely at such steep grazing incidence angles and carries an estimated uncertainty of order of 0.1°-0.2°, and also the fact that the interface is not perfectly straight as mentioned previously in 5.2.

6.5 Improvements to the device

Improvements can be made to the device to simultaneously increase the range of the deflection angle, improve the linearity of the device, and also flatten the transmitted intensity characteristics. Fig. 6.6 shows a simple modification to the output face of the device, in which a facet is polished at an angle of β or γ respectively. The facet acts to magnify the angular deflection via Snell's law into a less dense medium, and if the angle is appropriately chosen, there is a compensating behaviour for the previous transmission drop and the nonlinearity of the angular deflection.

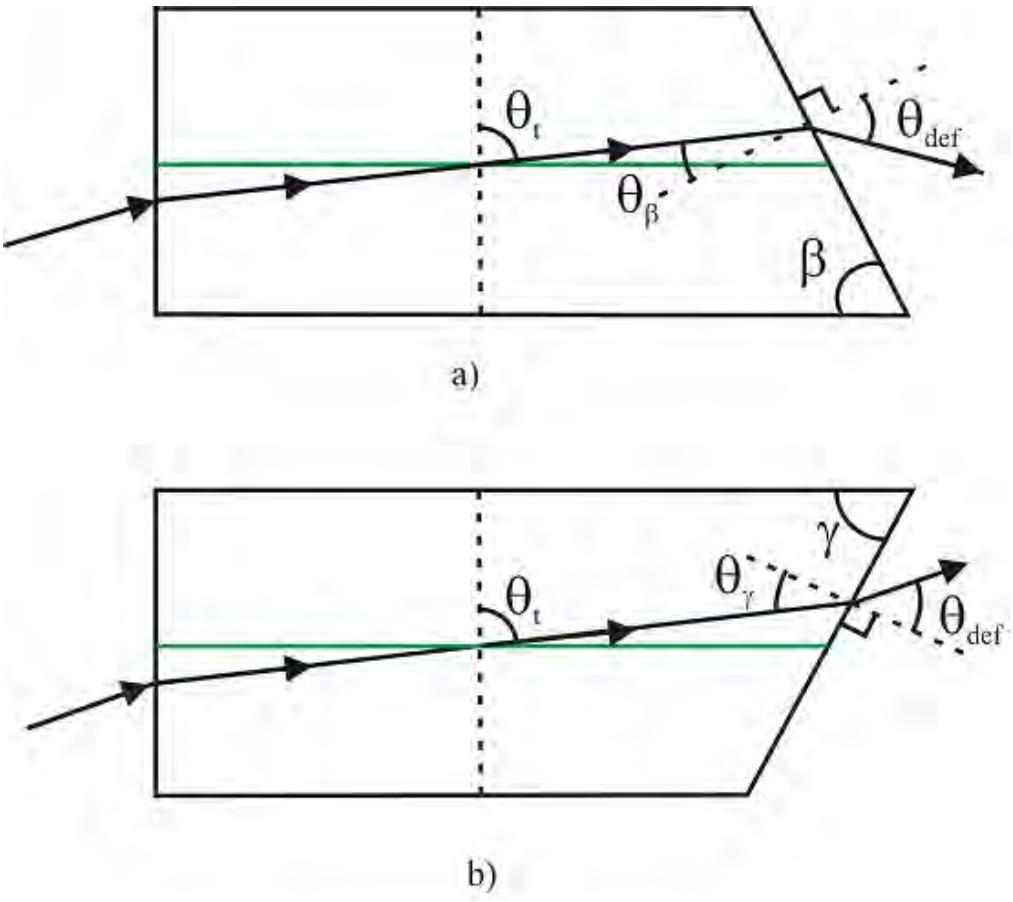

Fig. 6.6. Schematic of scanners with polished exit facets. The beam exits the rear face with angles of incidence θ_β (a) and θ_γ (b) respectively.

Fig. 6.7 illustrates this behaviour for a value of θ_{inc} = 87.75^{o} for a facet angled as shown in fig. 6.6(a), as is represented by the solid lines. In this geometry however, although the external angle of deflection is substantially increased when compared to that through an end face polished normally to the ray direction, the linearity is poor. Nevertheless, for β = 62.5^{o} a deflection of ~8^{o} is achievable for the voltage range between 0 and 1000V. In the normalised value of 1kVmm^{-1} an angular deflection of 1.6^{o} is achieved compared to 0.5^{o} without the exit facet.

When the facet is angled the opposite way, as shown in fig. 6.6(b), then the opportunity exists to simultaneously have a large angular deflection range, and good linearity of deflection and transmission as a function of applied voltage. Linearity is a desirable attribute for the device if implementation is to be easy, although it is not an intrinsic necessity as nonlinear effects can be taken into account when calibrating. The calculations for this oppositely angled facet are represented by the dashed lines in fig. 6.7 and show plots for facet angles spanning the range 66-69^{o}.

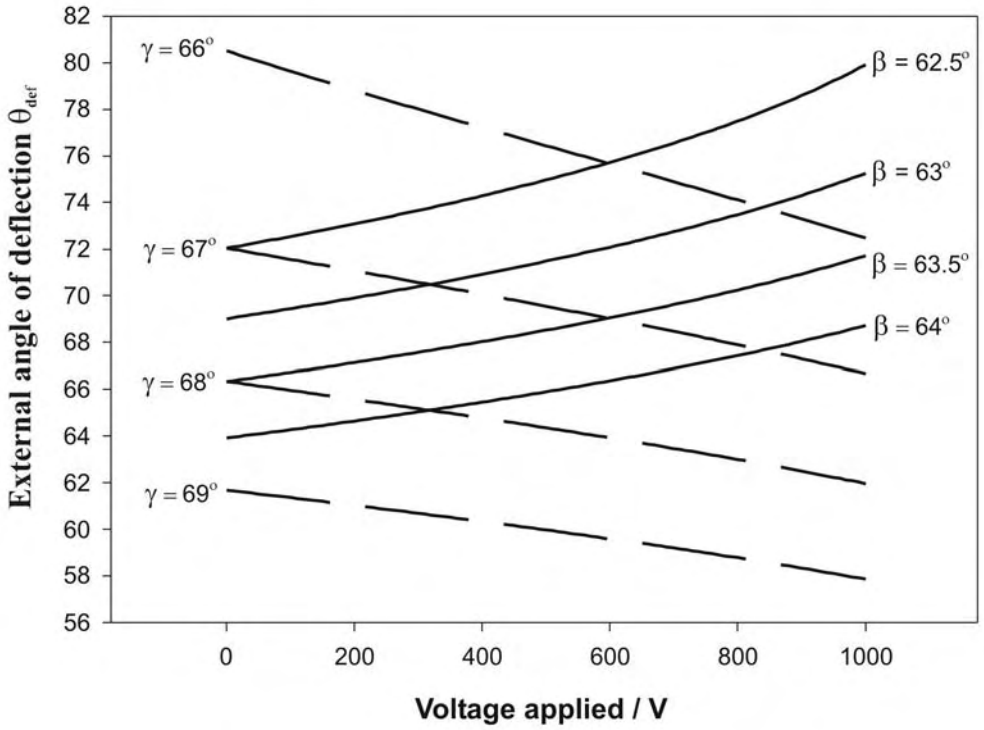

Fig. 6.7. External angle of deflection θ_{def} as a function of applied voltage, for the arrangement of fig.6.5(a), for facet angles β between 62.5° and 64.0° (represented by the solid lines). The dashed lines represent the external angle of deflection θ_{def}, for the arrangement of fig. 6.5(b), for facet angles γ between 66.0° and 69.0°. The common value of θ_{inc} for both cases is 87.75°.

As θ_t increases, the value of θ_γ decreases, thereby reducing the Fresnel reflectivity from this angled facet and acting to compensate for the decreasing value of transmission across the interface. Fig. 6.8 shows a comparison between a facet angled at 69° and a facet polished at effectively normal incidence. Although greater Fresnel reflectivity invariably occurs for this *s*-polarised state at these angles, it is immediately apparent that the transmission reduction has been at least partially compensated. For this geometry (θ_{inc} = 87.75°), this compensation is at the expense of an overall reduction of ~27% of the transmitted intensity.

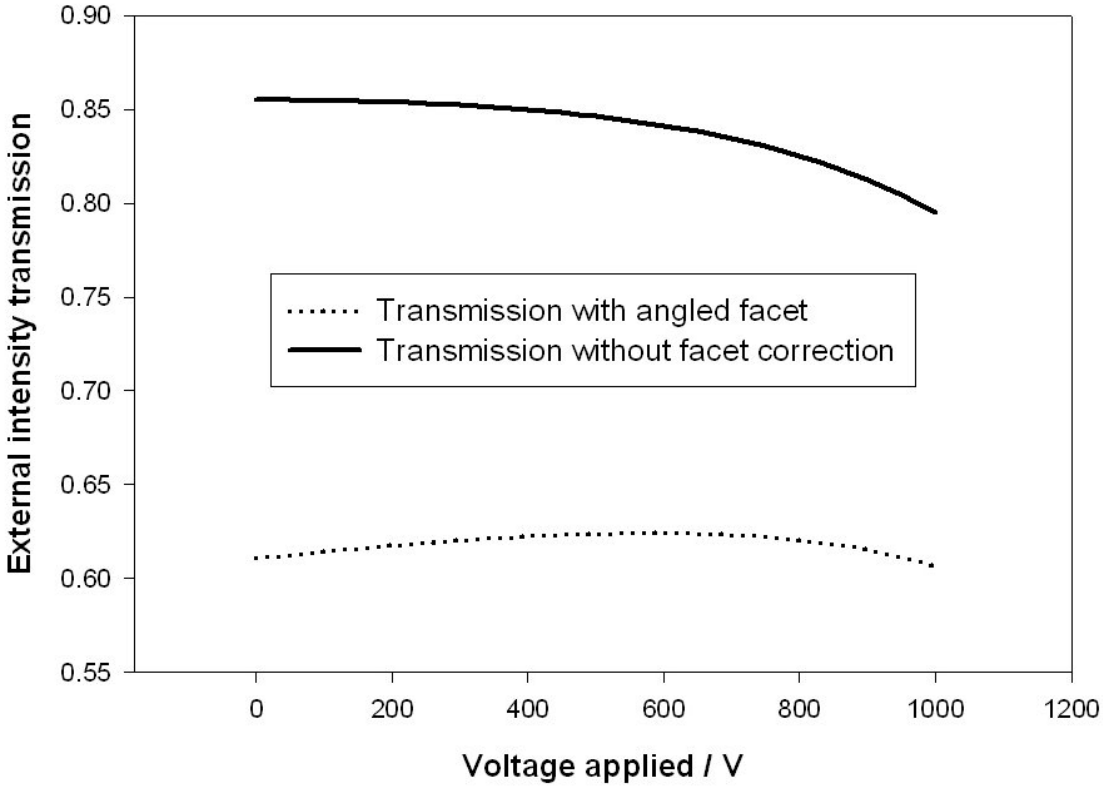

Fig. 6.8. Comparison between external intensity transmission with the facet as in fig. 6.6(b) and without exit face faceting, as a function of applied voltage.

A dramatic yet simple improvement can be made to the deflection angles achievable by any of the devices discussed in this chapter. This is achieved by using both polarities of applied field. So far only one polarity has been used, but by also reversing the polarity the total deflection angle achievable will be increased (effectively ~doubled), as the light can also be arranged to bend towards the normal, rather than just towards the interface.

Fig 6.9 shows results of angular deflection, θ_{def}, against applied voltage, and compares experimental results with those predicted by theory. The plot shows data obtained for *s*-polarised light from a He-Ne laser at a wavelength of 632.8nm incident on the interface between the two domains at an angle of 88.14° for a device facetted

with angle $\alpha \approx 66^{o}$ and shows an angular deflection of greater than 18° that also shows good linearity for an applied voltage range of ±1000V. It is seen that these experimental results are in very good agreement with those predicted by theory. These experiments have also been repeated using other wavelengths i.e. 1.52μm, which also show large deflection and are similarly in good agreement with the theoretically predicted results.

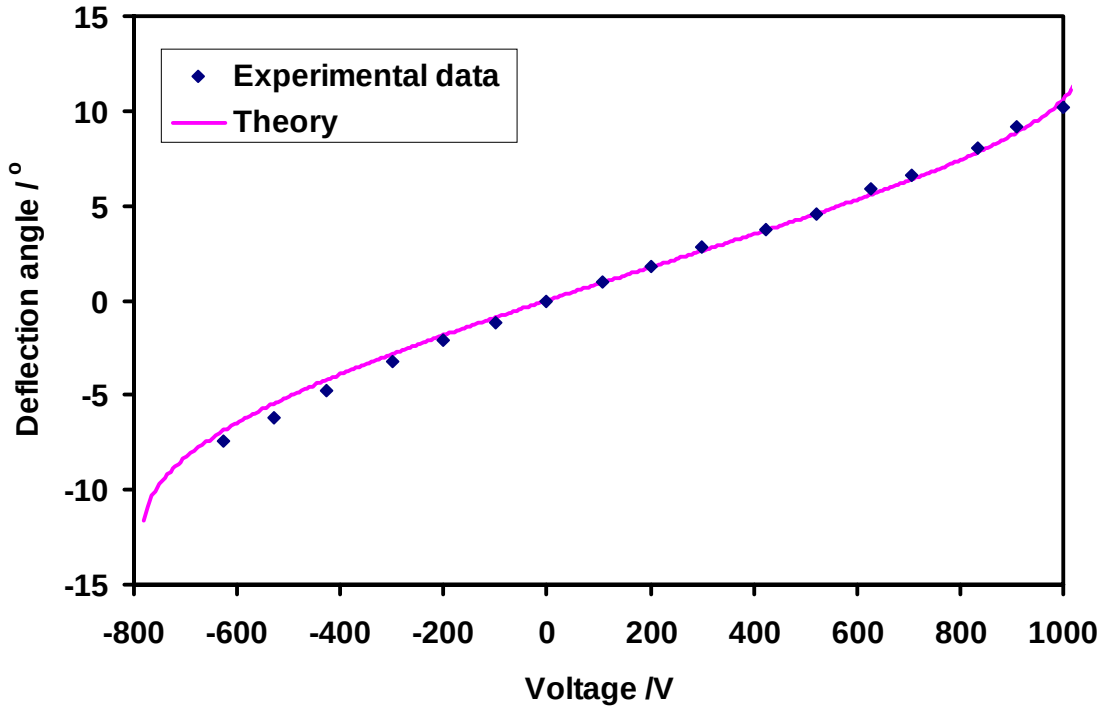

Fig.6.9. Angular deflection as a function of applied voltage

Fig 6.10 shows the beam profile of the output from a facetted deflector device. Although the beam is elliptical in shape due to the faceting of the device, if required this could be accounted for with the use of suitable cylindrical lenses. It can be seen that the beam size in the *y*-direction remains constant throughout the deflection and the beam size in the *x*-direction also remains constant over the deflection range -2^{o} to 6^{o} before diverging, as can be seen plotted in fig. 6.10.

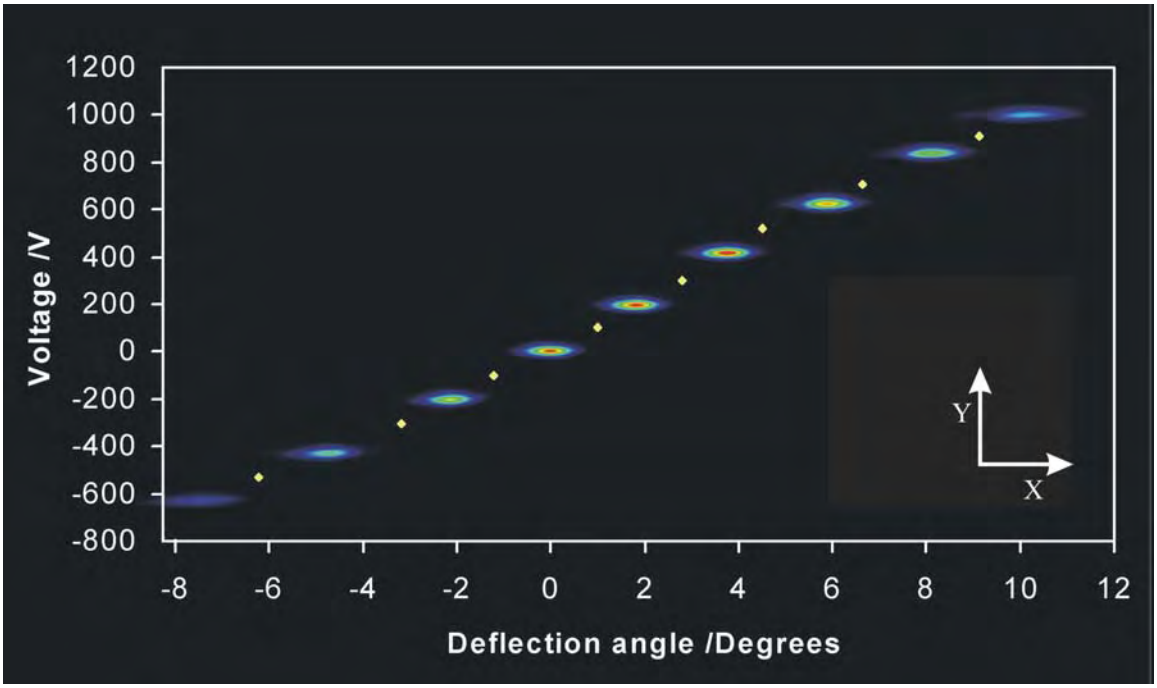

Fig. 6.10. Beam profile images as a function of applied voltage and angular deflection

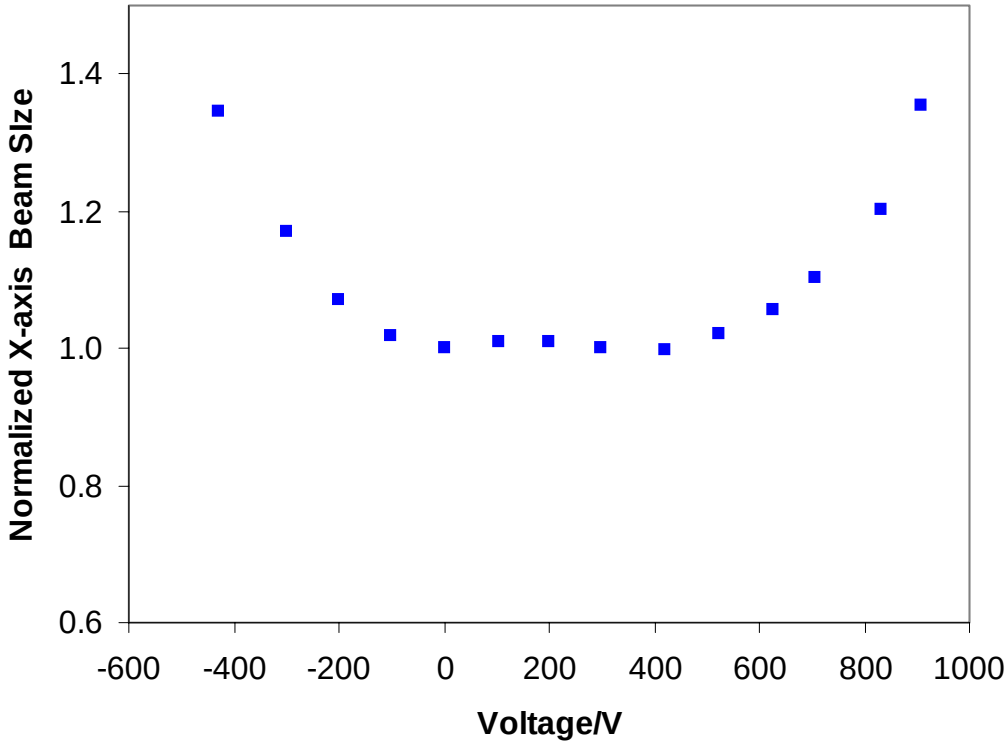

Fig. 6.11. Normalised measured beam size as a function of applied voltage

It can also be seen that as the beam is deflected it loses power, as in fig 6.12, due to increased Fresnel reflections as the beam nears the angles required for total internal reflection. It can again be seen that the experimental results are in good agreement with theory.

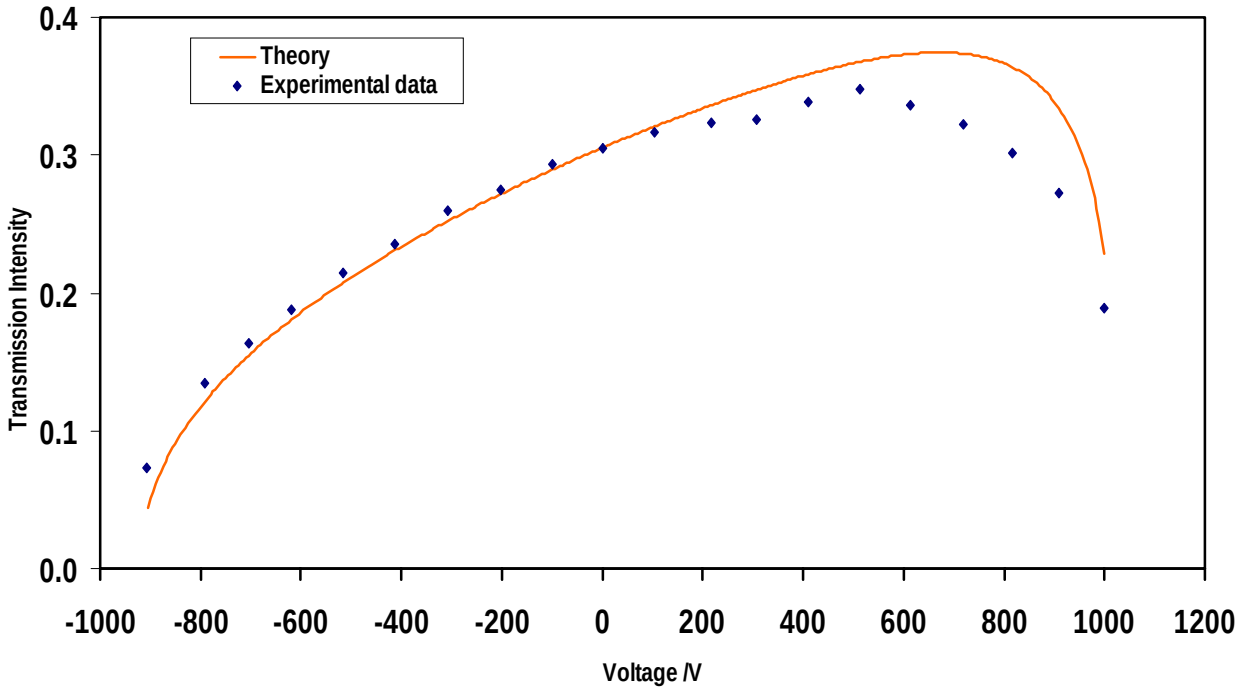

Fig. 6.12. Transmitted intensity as a function of applied voltage

6.6 Summary

A novel electro-optic beam deflector device has been described. The device permits a wide angular deflection range, of up to ~18^{o}, with simultaneous capability for good linearity of both deflection angle and transmission uniformity as a function of applied field. When compared to existing schemes for electro-optic scanning based on prisms, it is seen that this new geometry has a sensitivity that is between one and two orders of magnitude larger. It has also been shown that the device characteristics are a very good match to those predicted by theory.

6.7 References

[Abedin95] Abedin, K. S., Tsuritani, T., Sato, M., Ito, H., Shimamura, K. and Fukuda, T. (1995) *Optics Letters,* **20,** 1985-1987.

[Boyland01a] Boyland, A. J., Ross, G. W., Mailis, S., Smith, P. G. R. and Eason, R. W. (2001b) *Electronics Letters,* **37**, 585-587.

[Boyland01b] Boyland, A. J., Mailis, S., Hendricks, J. M., Smith, P. G. R. and Eason, R. W. (2001a) *Optics Communications,* **197**, 193-200.

[Barrington03] Barrington, S.J., Boyland, A.J., and Eason, R.W. *Submitted Applied Optics 2003*

[Chen94] Chen, Q. B., Chiu, Y., Lambeth, D. N., Schlesinger, T. E. and Stancil, D. D. (1994) *Journal of Lightwave Technology,* **12,** 1401-1404.

[Chiu99a] Chiu, Y., Gopalan, V., Kawas, M. J., Schlesinger, T. E. and Stancil, D. D. (1999) *Journal of Lightwave Technology*, **17,** 462-465.

[Chiu99b] Chiu, Y., Zou, J., Stancil, D. D. and Schlesinger, T. E. (1999) *Journal of Lightwave Technology,* **17,** 108-114.

[Eason01] Eason, R. W., Boyland, A. J., Mailis, S. and Smith, P. G. R. (2001) *Optics Communications,* **197,** 201-207.

[Gahagan99] Gahagan, K. T., Gopalan, V., Robinson, J. M., Jia, Q. Z. X., Mitchell, T. E., Kawas, M. J., Schlesinger, T. E. and Stancil, D. D. (1999) *Applied Optics*, **38,** 1186-1190.

[Hecht98] Hecht, E. (1998) *Optics,* Addison-Wesley, Reading, MA.

[Li96] Li, J., Cheng, H. C., Kawas, M. J., Lambeth, D. N., Schlesinger, T. E. and Stancil, D. D. (1996) *IEEE Photonics Technology Letters,* **8**, 1486-1488.

[Weis85] Weis, R. S. and Gaylord, T. K. (1985) *Applied Physics A-Materials Science & Processing,* **37,** 191-203.

[Yamada96] Yamada, M., Saitoh, M. and Ooki, H. (1996) *Applied Physics Letters,* **69,** 3659-3661.

Chapter 7

Futures and applications

7.1 Overview

There are many directions that the work discussed in this thesis could follow and this chapter will introduce some of these possibilities. The study of the LIFE of chapter 4 is still in the early stages and requires further research to lead to a better understanding of the processes involved as well as attempts to create structures in a more controllable way. The work of chapters 5 and 6 however is further developed and attempts could be made to implement this into useful devices. Investigation of the use of alternative materials for this application as a route to finding improved device performance could also be carried out.

7.2 LIFE

The next logical step in the structuring process using LIFE would be to create controlled (regular periodic for example) structures. The simplest of such structures would be periodic with straight or possibly curved lines, and a method for defining these lines would be to photolithographically pattern the +z face of a sample, thereby creating a phase-mask like structure and then illuminate through this face to produce a corresponding pattern on the –z face. This could be done using the setup and procedure described in 4.3.3. The results of the studies reported in ch.4 have shown that structures formed in areas subjected to a certain level of irradiance form long parallel lines that self align along 3 preferential axes, it would therefore be reasonable

to try and align the pattern with one of these preferred axes. These axes are parallel or perpendicular to the y-axis.

Following successful control of the structuring process more ambitious 2D and 3D features could be attempted.

7.3 Electro-optic switch and deflector

7.3.1 2D deflector

Using the device described previously in ch.6 and [Eason01] a 2D scanner could easily be developed. The device would be relatively cheap and simple to construct. It would also contain no moving parts and therefore could be smaller, faster and more durable than current alternatives.

A possible schematic for a 2D deflector is shown in fig.7.1. In this schematic the first deflector is a poled structure as described previously which is used to bring about beam deflections in the vertical plane. The beam then enters the second deflector which is used to bring about deflection in the horizontal plane. In the suggested schematic this second deflector is made using the bonding technique discussed in 3.4.8, where the like faces (e.g. 2 –*z* faces) of two single domain z-cut crystals are joined to form the interface. This has the advantage of providing a larger aperture for the beam entering the second deflector. This is a key feature to this 2D deflector. In other electro-optic deflectors displacement of the beam by the first deflector would move the beam out of alignment with the second deflector.

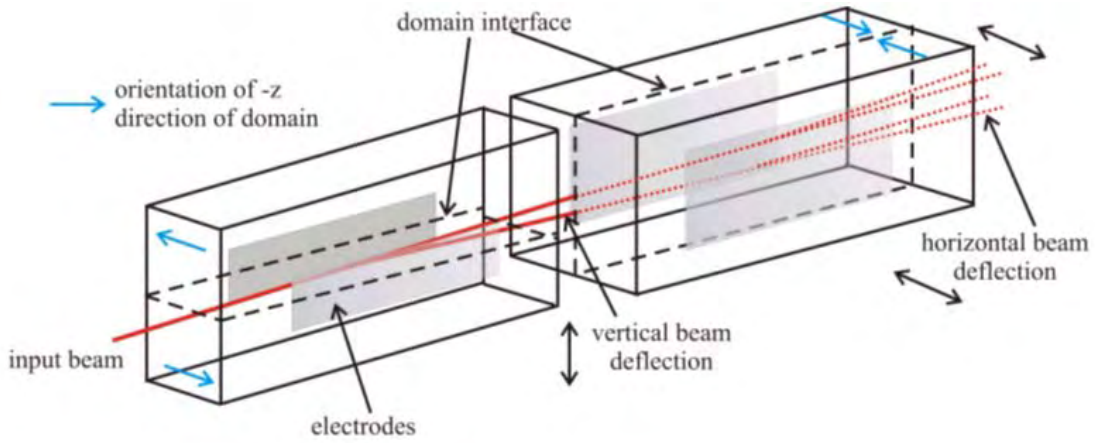

Fig.7.1. Schematic for 2D beam deflector

7.3.2 Multiple output cascaded device

Combining a number of the devices described in chapter 5 and [Boyland01a, Boyland01b] to produce a multiple output cascaded device on a single LN sample is possible. Fig.7.2. shows two simple examples of possible cascaded switch architectures.

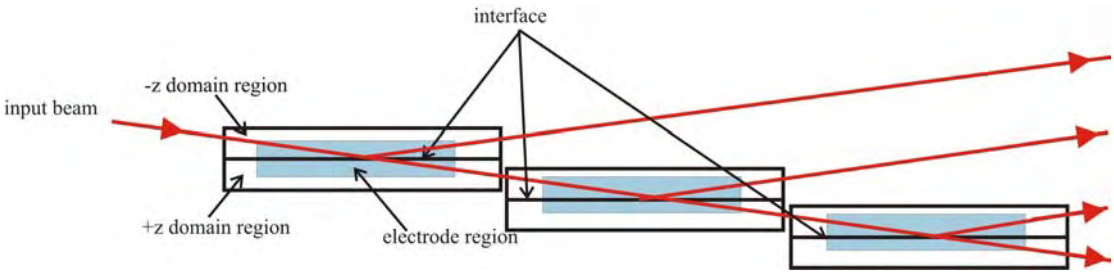

a)

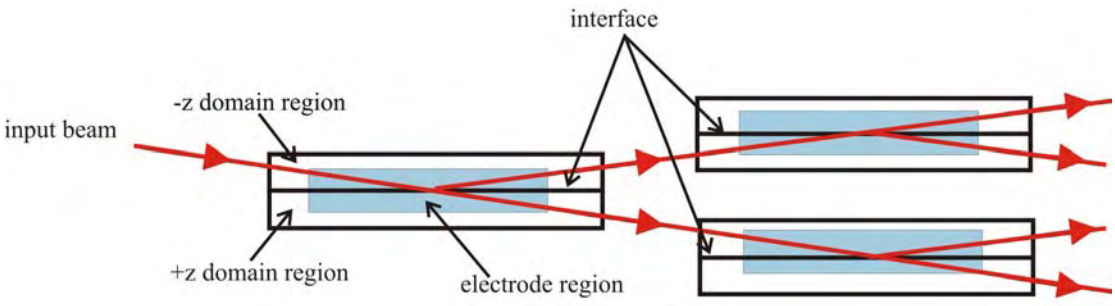

b)

Fig. 7.2. Possible cascaded device architectures

Both the architectures shown above require only relatively simple fabrication procedures. The advantage of the design shown in b) is that it provides the same number of outputs but is shorter in length and therefore the beam entering the device needs to be collimated over a shorter distance. If the constraints on device thickness meant that the beam required refocusing within the device then electro-optical cylindrical lenses as reported by Yamada *et al* [Yamada96] could be included within the device architecture.

7.3.3 Switching speed

The switching and deflection speeds achievable for the device will be an important factor in deciding upon its suitability for many applications. The performance speed is limited by:

- speed of the driving electronics
- capacitance of the device

Although this device requires high voltages, the voltage driver requirements will be intrinsically simple as no current is required. The capacitance of the device can be kept to a minimum by limiting the size of the electrodes to cover only the areas directly above and below the domain boundary. The capacitance (C) of the device described in ch's 5 and 6 can be calculated using the expression:

$$C = \frac{\varepsilon_0 \varepsilon_r A}{d} \qquad \textbf{(7.1)}$$

where ε_0 is the permittivity of free space, ε_r is the relative permittivity (or dielectric constant) which has a value of 28 [Yariv] for LN, A is the electrode area which has dimensions of length 10mm and width 2 mm, and *d* is the device thickness.

This results in a capacitance value of 17pF, which would result in a time constant *t* of 0.85ns when the device is terminated using a 50Ω resistor. The electrode size can be significantly reduced which will result in faster switching times, e.g. if the electrode width was reduced to 300μm the resulting time constant would be just 0.13ns.

7.3.4 Alternative materials

The manufacture of the TIR switch and deflector devices is not limited to LN alone. Alternative materials of interest are those with larger electro-optic coefficients, or as in the case of stoichiometric LN, similar electro-optic coefficients but lower coercive field [Oxide]. This leads to lower voltage requirements for poling which may aversely effect the device performance by limiting the electric field that can be applied across an interface before re-poling occurs. The advantages of using materials with larger electro-optic coefficients are that beam deflection or switching will occur at lower voltages for devices of the same dimensions as the equivalent device in LN. Alternatively thicker devices could be fabricated as the requirements for the applied electric field to cause deflection or switching would be lower. Some of the possible materials and their electro-optic coefficients can be seen in table 8.1. Included in this table is a polymeric material which shows a large electro-optic coefficient. Developments in polymeric electro-optic materials means that some of these materials now have electro-optic coefficients that rival those of the best inorganic materials [de Ridder99]. Although large scale application of electro-optic polymers for high performance, complex, reliable and low cost devices is still some way in the future, these materials should be considered.

Material	**Electro-optic coefficients ($10^{-12}mV^{-1}$)**	**Reference**
Stoichiometric LN	r_{13} = 10.4	[Oxide]
	r_{33} = 38.3	[Oxide]
SBN	r_{13} = 67	[Yariv]
	r_{33} = 1340	[Yariv]
$BaTiO_3$	r_{51} = 1640	[Yariv]
Polymer - DAST	r_{11} = 530	[Thakur02]

Table 7.1. Electro-optic coefficients of alternative materials

7.4 Applications

There are numerous applications for the structuring process reported in ch.4 and devices reported in ch's 5 and 6. The process reported in ch.4 will hopefully lead to a controllable structuring technique that allows the realisation of the potential of LN as a MEMS / MOEMS material. The current well established MEMS material is silicon. However in contrast to silicon, LN possesses a range of linear and nonlinear properties that yield numerous potential benefits in the context of MEMS actuation and device application. The devices described in ch's 5 and 6 have many potential applications including use in laser projection systems, colour separation, 1D and 2D barcode scanning, Q-switching and even streak cameras. Discussion of some of these applications follows.

7.4.1 Streak cameras

A streak camera is a device used to measure ultra-fast light phenomena and can deliver intensity vs. time vs. position (or wavelength) information. Figure 7.3a shows a schematic of the operating principle for the current generation of streak camera.

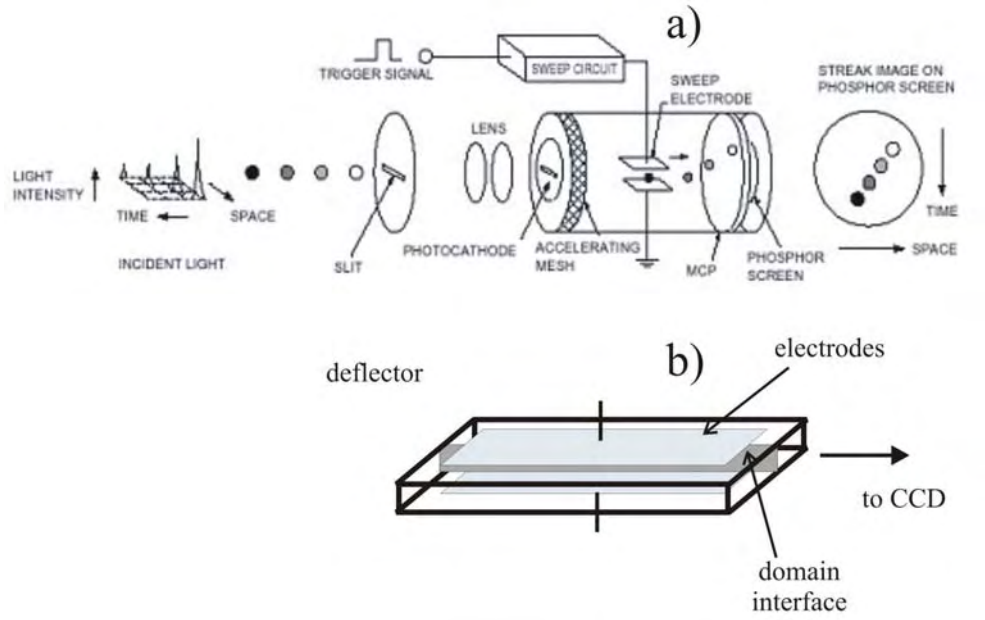

Fig. 7.3. a) Schematic of operating principle for current streak camera design [Hamamatsu], b) an alternative design using the electro-optically controllable deflector

The light being measured passes through a slit and is formed by the optics into a slit image on the photocathode of the streak tube. Light that is incident on the photocathode is converted into photo-electrons whose number density is proportional to the intensity of the incident light. These electrons then pass through a pair of accelerating electrodes, where they are accelerated and are incident on a phosphor screen. As the electrons produced from the optical pulses pass between a pair of sweep electrodes, a high voltage ramp is applied at a time synchronised to the incident light. This initiates a high-speed sweep (the electrodes are swept from top to bottom). During the high-speed sweep, the electrons, which arrive at slightly different times, are deflected at slightly different angles in the vertical direction, and enter the micro-channel plate (MCP). As the electrons travel through the MCP, they are multiplied several thousands of times, after which they are incident on a second phosphor screen, where they are converted again to light.

On the phosphor screen, the phosphor image corresponding to the optical pulse which was the earliest to arrive occurs in the uppermost position, with the other images being arranged in sequential order from top to bottom. Therefore the vertical direction on the phosphor screen serves as the time axis. The brightness of the phosphor images is proportional to the intensity of the corresponding incident optical pulse. The horizontal direction of the phosphor image corresponds to the horizontal location of the incident light [Hamamatsu].

However this design could be significantly simplified by replacing the photocathode, accelerating mesh, sweep electrodes, MCP and the phosphor screen with a deflector device, as described in ch.6, coupled into a CCD camera, as shown in fig. 7.3b.

7.4.2 Q-switch

The technique of Q-switching allows the generation of laser pulses of short duration (from a few nanoseconds to a few tens of nanoseconds) and high peak power (from a few megawatts to a few tens of megawatts). The principles of this technique are well known and have been used since being reported by Hellwarth in 1961 [Hellwarth61].

One of the most widely used methods for Q-switching is the use of an electro-optical shutter called a Pockels cell. As discussed previously in ch.5 the TIR switch has the advantages of having low operating voltages as well as being much less wavelength dependent that the Pockels cell. The voltage requirement could be reduced further as only a small deflection of beam would achieve the desired effect without the requirement for TIR to occur. Another comparison that should be made is that the

Pockels cell is a polarisation controlled switch whereas this device is a deflector switch which is intrinsically a lot more sensitive.

7.4.3 Barcode scanner

Barcodes are widely used as machine readable identification labels for an enormous number of products. The original 1D barcode contains a unique serial number coded in black and white bars, which acts as a key to a database containing more detailed information and an example of this can be seen in fig. 7.4a. The desire by end-users to have more information in the barcode led to the development of the 2D barcode. This could be used as a portable database rather than just a database key. The 2D barcodes are classified into two classes, *stacked* symbology, which refers to symbology made up of a series of 1D barcodes, as can be seen in fig. 7.4b. The other class is referred to as *matrix code*, which is based upon the position of black spots within a matrix. Each black element is the same dimension and it is the positions of the elements that code the data, as can be seen in fig. 7.4c.

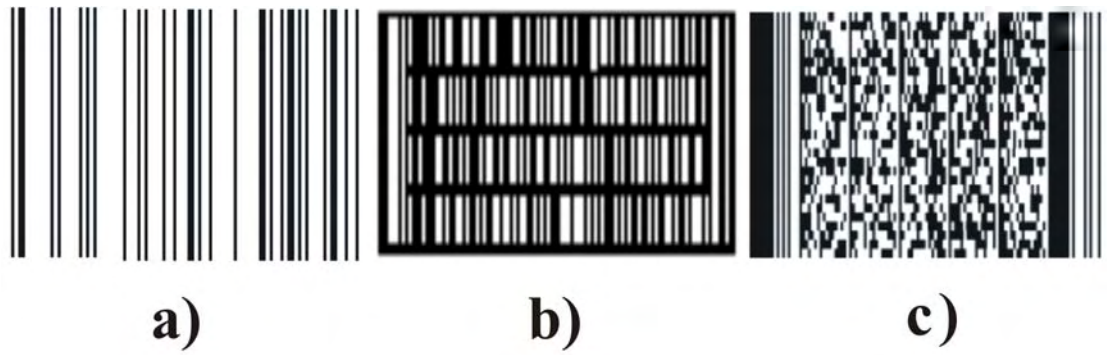

Fig. 7.4. Types of barcode, a) 1D, b) 2D stacked, and c) 2D matrix code.

Barcode scanners operate by using photodetectors to sense changes in the reflected intensity from the focused beam of light that is being used to read the barcode. The introduction of helium-neon lasers as a light source for non-contact barcode reading in

the 1970's led to a revolution in the field, with further significant developments in 1987 with the introduction of visible light laser diodes. Laser diode barcode scanners quickly captured the market. Non-contact laser scanners can be fixed or handheld units with stationary or moving beams. The units with moving beams are referred to as self scanners, which have scan speed requirements of usually around 40Hz for stationary items, with speed requirements increasing slightly for moving items i.e. on a conveyer belt. Handheld scanner models currently on the market contain moving parts to induce the beam deflection and this makes the devices sensitive to rough use. The use of a deflector as described in ch.6 for scanning 1D barcodes would have the advantages of being very simple to design and fabricate as well as having no moving parts, so it could be cheaper as well as being more robust. The use of the 2D deflector described earlier in this chapter could be used for raster scanning of 2D barcodes.

7.5 Summary

Many feasible potential applications of the structuring techniques and devices reported in this thesis have been suggested. The devices implementations could provide routes to simplified, cheaper and more robust architectures.

7.6 References

[Barcode 1] http://www.adams1.com/pub/russadam/barcode1.cgi

[Boyland01a] Boyland, A. J., Ross, G. W., Mailis, S., Smith, P. G. R. and Eason, R. W. (2001) *Electronics Letters,* **37,** 585-587.

[Boyland01b] Boyland, A. J., Mailis, S., Hendricks, J. M., Smith, P. G. R. and Eason, R. W. (2001) *Optics Communications,* **197,** 193-200.

[de Ridder99] de Ridder, R. M., Driessen, A., Rikkers, E., Lanbeck, P.V., and Diemeer, M.B.J. (1999) *Optical Materials,* **12,** 205-214.

[Eason01] Eason, R. W., Boyland, A. J., Mailis, S. and Smith, P. G. R. (2001) *Optics Communications,* **197,** 201-207.

[Hamamatsu] http://www.hamamatsu.co.uk/

[Hellwarth61] Hellwarth, R. W. (1961) In *Advances in Quantum Electronics*(Ed, Singer, J. R.) Columbia University Press, New York, pp. 334-341.

[Oxide] www.opt-oxide.com

[Svelto] Svelto, O. (1993) *Principles of lasers,* Plenum Press, London.

[Yamada96] Yamada, M., Saitoh, M. and Ooki, H. (1996) *Applied Physics Letters,* **69,** 3659-3661.

[Yariv] Yariv, A. (1997) *Optical Electronics in Modern Communications,* Oxford University Press, Oxford.

Chapter 8

Conclusions

8.1 Conclusions

Through the study of LIFE reported in chapter 4 a greater knowledge of how the parameters of illumination and etching time, Fe dopant level, and irradiance levels effect the development of the structures has been developed. Through analysis of the structures formed it has been learnt that the structures propagate along 3 preferential directions each 120^{o} apart, and are

- resistant to etching
- are positively charged in comparison to the background substrate.
- have the < μm width that is associated with domains

These observations lead to the conclusion that the structures are similar to, and maybe inverted domains.

By studying and comparing SEM images of the LIFE samples it was possible to establish a number of rules that governed the patterns that occurred during the growth of these structures. These rules are:

1. Lines grow from dots

2. Lines can propagate only along one of three directions, at 120^{o} to each other

3. Lines cannot touch or cross over each other

4. Lines may change direction to avoid another line.

5. Line growth stops when a crossing would inevitably occur

This lead to the development of a model (*see appendix 2*) that showed similar patterning to that occurring during the LIFE process.

The novel electro-optically controlled domain engineered switching device reported in chapter 5 has been demonstrated to show good contrast ratios (in excess of 20dB) which could increase with the optimisation of manufacturing technique to fulfil the potential of TIR (which is a 100% efficient process). It was shown that the behaviour of the device was in good agreement with a theoretical model relating to the devices behaviour for both visible and IR wavelengths.

The device was also shown to operate as an electro-optically controlled beam deflector and this mode of operation was reported in chapter 6. The device demonstrated a wide angular deflection range, of up to ~18^{o}, with simultaneous capability for good linearity of both deflection angle and transmission uniformity as a function of applied field. When compared to existing schemes for electro-optic scanning based on prisms, it is seen that this new geometry has a sensitivity that is between one and two orders of magnitude larger. It has also been shown that the device characteristics are a very good match to those predicted by theory.

In chapter 7 areas of futures work and applications were reported showing just some of the possibilities for continuing the work reported in this thesis.....

Appendix 1

Cleaning procedure

The first step in preparing these samples is thoroughly cleaning them, this is necessary to remove any particulate contamination on the sample surface as this may prevent the photoresist being applied uniformly and may cause breakdown during the poling process. The process is carried out in a cleanroom environment using an ultrasonic bath preheated to a temperature of 55°C. Cleaning is a multi-step process using a series of solvents as detailed below in table 1. All solvents are preheated to 55^{o}C before use.

Step	Cleaning solution	Time	Reasons for use
1	Ecoclear	20	Removes organic contaminants i.e. fingerprints
2	Acetone	20	Removes ecoclear and organic residue
3	Isopropyl Alcohol(IPA)	20	Removes acetone and organic residue
4	Distilled water	20	Removes IPA and rinses any remaining residues

The samples were then blown dry using a filtered nitrogen gun.

Appendix 2

Modelling of LIFE

N Spots	*Model Image*	*Fourier Transform*
100	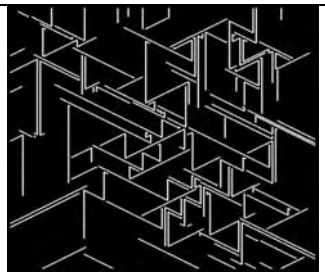	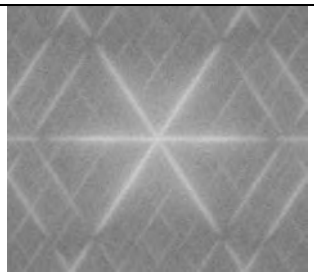
500	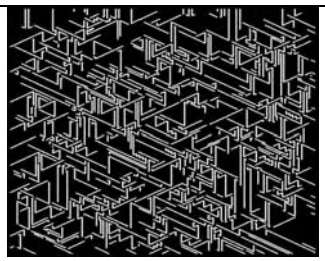	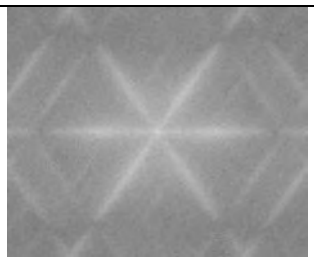
1000	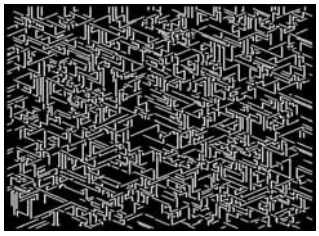	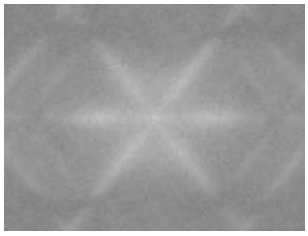
2500	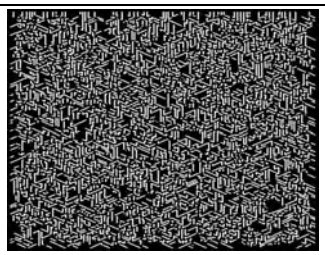	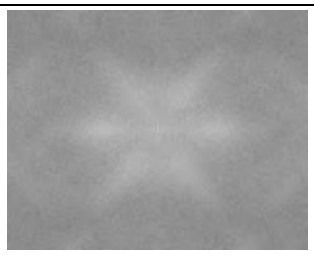
5000	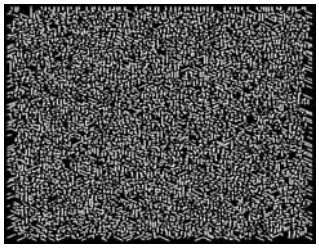	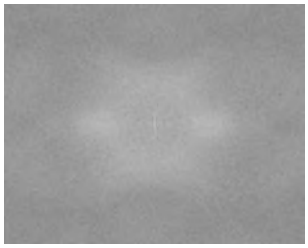

The modelling results show images from the model and their respective Fourier transforms. The figure shows results for increasing numbers of spots, N. The spots are representative of the initial growth sites observed from experimental data. The increasing spot density is representative of increases in Fe dopant level and / or irradiance level. This model shows a good representation of experimental results.

Appendix 3

Publications

Journal papers

J.G.Scott, **A.J.Boyland**, R.W.Eason

The meaning of LIFE!

to be submitted Nature Materials April/May 2003

S.J.Barrington, **A.J.Boyland**, R.W.Eason

Resolution considerations in electro-optic single interface deflectors

Submitted Applied Optics March 2003

S.J.Barrington, **A.J.Boyland**, R.W.Eason

Domain engineered lithium niobate as a medium for an integrated solid-state 2D scanning system

Submitted Applied Optics March 2003

A.J.Boyland, S.Mailis, J.M.Hendricks, P.G.R.Smith, R.W.Eason

Electro-optically controlled beam switching via total internal reflection at a domain-engineered interface in $LiNbO_3$

Optics Communications 2001 Vol. 197 pp193-200

R.W.Eason, **A.J.Boyland**, S.Mailis, P.G.R.Smith

Electro-optically controlled beam deflection for grazing incidence geometry on a domain-engineered interface in $LiNbO_3$

Optics Communications 2001 Vol. 197 pp201-207

A.J.Boyland, G.W.Ross, S.Mailis, P.G.R.Smith, R.W.Eason

Total internal reflection switching in electro-optically addressable domain-engineered $LiNb0_3$

Electronics Letters 2001 Vol.37(9) pp.585-7

A.J.Boyland, S.Mailis, I.E.Barry, R.W.Eason, M.Kaczmarek

Latency effects and periodic structures in light induced frustrated etching of Fe:doped $LiNbO_3$

Applied Physics Letters 2000 Vol.77(18) pp.2792-2794

Conference oral presentations

S.J.Barrington, **A.J.Boyland**, C.L.Sones, R.W.Eason

Electro-optic solid state beam deflection: Resolution considerations and 2-D implementation

CLEO/Europe EQEC Munich Jun 22-27 2003

J.G.Scott, **A.J.Boyland**, R.W.Eason

Sub-micron filamentary structures formed during light induced frustrated etching of lithium niobate: Results and modelling

CLEO/Europe EQEC Munich Jun 22-27 2003

A.J.Boyland, S.Mailis, J.M.Hendricks, P.G.R.Smith, R.W. Eason

Beam deflection and T.I.R switching in domain-engineered $LiNbO_3$

IOP- Optics and Nonlinear Optics of Micro-structured and Nanostructured materials

London 14th Nov 2001

A.J.Boyland, S.Mailis, J.M.Hendricks, P.G.R.Smith, R.W.Eason

Electro-optically controlled beam deflection and switching via total internal reflection at a domain-engineered interface in $LiNbO_3$

International Workshop on Periodic Microstructured Nonlinear Optical Materials 2001 Proceedings for conference

R.W.Eason, **A.J.Boyland**, S.Mailis, J.M.Hendricks, P.G.R.Smith

Electro-optically controlled beam deflection and switching in domain-engineered $LiNbO_3$

IOP-MOEMS London 31 Oct 2001

A.J.Boyland, S.Mailis, P.G.R.Smith, R.W.Eason

Electro-optically controlled TIR switching in domain-engineered $LiNbO_3$

International Workshop on Periodic Microstructured Nonlinear Optical Materials Madrid 10-13 Jun 2001

A.J.Boyland, S.Mailis, R.W.Eason

Switching applications in domain-engineered $LiNbO_3$

COSTP2 Meeting Hungary May 2001

A.J.Boyland, G.W.Ross, S.Mailis, P.G.R.Smith, R.W.Eason

Electro-optically addressable total internal reflection switch in domain-engineered $LiNbO_3$

CLEO 2001 Baltimore 6-11 May 2001 CMD2

R.W.Eason, I.E.Barry, **A.J.Boyland**, P.T.Brown, S.Mailis, P.G.R.Smith

Microstructuring of ferroelectric crystal media using light poling and etching techniques

Eleventh Int School on Quantum Electronics : Laser Physics and Applications Varna Bulgaria 18-22 Sep 2000 (Invited)

Conference poster presentations

A.J.Boyland, R.W. Eason

Micron-scale features in LiNbO3 produced by interferometric patterned light induced frustrated etching

IOM Materials Congress 2000 Cirencester, UK 12-14 April 2000

Patents

UK Patent Application No 0108307.0

Electro-optically addressed grazing incidence beam scanner & deflector